WING-TIP VORTEX STRUCTURE AND WANDERING

by

Steffen Pentelow

A thesis submitted to
the Faculty of Graduate and Postdoctoral Studies
in partial fulfillment of
the requirements for the degree of

MASTER OF APPLIED SCIENCE

in Mechanical Engineering

Ottawa-Carleton Institute for Mechanical and Aerospace Engineering
University of Ottawa
Ottawa, Canada

May 2014

Abstract

An isolated wing-tip vortex from a square-tipped NACA 0012 wing at an angle of attack of 5° was studied in a water tunnel at a chord based Reynolds number of approximately 2.4×10^4. Measurements were taken using stereo particle image velocimetry at three measurement planes downstream of the wing under each of three freestream turbulence conditions. The amplitude of wandering of the vortex axis increased with increasing distance downstream of the wing and with increasing freestream turbulence intensity. The magnitude of the peak azimuthal velocity decreased with increasing distance from the wing as well as with increases in the freestream turbulence intensity. The streamwise velocity in the vortex core was less than the freestream velocity in all cases. Time resolved histories of the instantaneous waveform shape and location of the vortex axis were determined from sequences of images of fluorescent dye released from the wing.

Acknowledgements

I am greatly indebted to the many friends and family who have supported me as I have worked on this thesis. In particular, to my parents, my sister and my brother-in-law whose love and encouragement has been unfailing.

My sincere thanks go to Dr. Stavros Tavoularis for his patience in guiding and teaching me, which has allowed me to be successful in my work.

I am grateful to my fellow students who have been with me daily in my work; especially to Christina Vanderwel, George Choueiri and Laura Haya whose knowledge and experience I have frequently relied on. The staff of the machine shop also have my gratitude for their help and expertise.

Thank you to the Natural Sciences and Engineering Research Council of Canada for financially supporting me with a scholarship and the project with research grants.

Table of Contents

List of Tables

List of Figures

Nomenclature

A	aspect ratio of a wing
a	power law fit constant (Equation 4.2, 4.4)
a_1	linear least squares fit constant (Equation 4.8)
a_2	linear least squares fit constant (Equation 4.8)
a_{ij}	anisotropy tensor (Equation 4.5)
b	wing span
C	a closed curve bounding the surface S
c	chord length of the wing
d_P	seed particle diameter
g	acceleration due to gravity
k	turbulent kinetic energy (Equation 4.3)
k_w	axial wave number
$L_{\alpha\alpha,k}$	integral length scale (Equation 4.7)
L_r	reference length on the camera's recording surface
l	closed loop path defining the edge of the surface C
l_r	reference length in the measurement plane
M	turbulence grid mesh spacing
m	azimuthal wave number
N	number of measurements used in calculating a mean

n	power law fit constant (Equation 4.2, 4.4)
p	pressure
p_1	polynomial describing the path of the vortex axis in the XY plane (Equation 5.1)
p_2	polynomial describing the path of the vortex axis in the XZ plane (Equation 5.2)
Q	Q parameter (Equation 3.10)
Q_{COM}	centre of mass of the Q parameter
Q_{max}	maximum value of the Q parameter
q_s	swirl parameter (Equation 2.6)
$R_{\alpha\alpha,k}$	two-point velocity autocorrelations (Equation 4.6)
Re_c	chord based Reynolds number
r	radial distance from the vortex core
r_{AD}	radius of the circular area considered in calculations of the $\Delta U_{x,COM}$
r_{def}	radius of the circular area considered in calculations of the $\mathbf{U_{def}}$
r_{inv}	radial location at which the azimuthal velocity profile becomes $\propto {}^{1}\!/_{r}$
r_k	separation between the two velocity vectors in the direction k for two-point velocity autocorrelations
r_{max}	radial location of the peak azimuthal velocity
r_o	vortex core radius
r_Q	radius of the circular area considered in calculations of the Q_{COM}

r_{SS}	radius of the circular area considered in calculations of the SS_{COM}
S	surface over which Γ is calculated
$\mathbf{S}$	rate of strain tensor (*i.e.*, the symmetric component of the velocity gradient tensor)
SS	swirling strength (Equation 3.9)
SS_{COM}	centre of mass of the swirling strength
SS_{max}	maximum value of the swirling strength
t_i	time at which frame i is taken
$tr(*)$	trace of any square matrix $*$
$\mathbf{U}$	velocity vector
$\mathbf{U_{2C}}$	two component velocities derived from a single camera's double framed particle images (Equation 3.1)
$U_{2C,z}$	transverse (Z) component of velocity derived from a single camera's double framed particle image (Equation 4.1)
$\mathbf{U_{3C}}$	three component velocities derived from images from two cameras' double framed particle images
$\mathbf{U_{def}}$	deformation velocity of the vortex axis
$\mathbf{U_{seed}}$	velocity of the seed particles relative to the fluid velocity
U_r	radial velocity from the vortex axis in a YZ plane
U_T	terminal rise or sink velocity of a seed particle in the water tunnel (Equation 3.4)
$\mathbf{U_{VPM}}$	vortex planar movement velocity (Equation 5.5)

U_x	axial velocity (positive in the downstream direction)
U_y	spanwise velocity (positive toward the root of the wing from the tip)
$U_{y,def}$	deformation velocity of the vortex axis in the Y direction
U_{yz}	magnitude of the velocity parallel to the YZ plane
U_z	transverse velocity (positive toward the suction side of the wing)
$U_{z,def}$	deformation velocity of the vortex axis in the Z direction
U_θ	azimuthal velocity about the vortex axis in a YZ plane (positive in the counter-clockwise direction)
U_∞	mean freestream velocity for a given measurement plane and freestream turbulence condition
u_x	fluctuating component of the axial velocity (positive in the downstream direction)
u_y	fluctuating component of the spanwise velocity (positive toward the root of the wing from the tip)
u_z	fluctuating component of the transverse velocity (positive toward the suction side of the wing)
u_i	velocity fluctuation in the direction i, which represents the axis X, Y, or Z
X	streamwise distance from the quarter chord position on the wing (positive downstream)
X_{VS}	spacing between velocity vectors in a PIV vector map
X_o	streamwise location of the effective origin for turbulent stress decay

x	streamwise distance from the measurement plane
Y	spanwise distance from the quarter chord position on the wing (positive toward the root of the wing from the tip)
Y_{ax}	Y coordinate of the vortex axis location
y	spanwise distance from the vortex axis in a YZ plane (positive toward the root of the wing from the tip)
Z	transverse distance from quarter chord position on the wing (positive on the suction side of the wing)
Z_{ax}	Z coordinate of the vortex axis location
z	transverse distance from the vortex axis in a YZ plane (positive on the suction side of the wing)

Greek symbols

α	angle of attack
α_1	angle between primary axis of camera 1 and the streamwise axis X
α_2	angle between primary axis of camera 2 and the streamwise axis X
α_m	magnification coefficient of the camera system (Equation 3.3)
Γ	circulation (Equation 2.1, 2.3)
Γ_o	total vortex circulation
Γ^*	mean circulation at the radius of the peak azimuthal velocity for the no-grid case
Δr_Q	change in radius over which $\lvert\Delta YZ_Q\rvert$ occurs
Δt	time between frames

ΔU_x	axial velocity deficit (Equation 5.4)
$\Delta U_{x,COM}$	centre of mass of the axial velocity deficit
$\Delta U_{x,max}$	maximum value of the axial velocity deficit
ΔX_{CCD}	perceived displacement of a particle on the image recording surface
ΔYZ_Q	change in location of the Q_{COM}
δ_{ij}	Kronecker delta
$\delta U_{\theta,x}$	Uncertainty in U_θ and U_x due to the inclination of the vortex axis with respect to X
$\delta *$	uncertainty associated with any parameter $*$
ϵ_u	precision uncertainty of a velocity vector
Θ	angle between the vortex axis and the streamwise axis X (Equation 5.3)
θ	angular component in the cylindrical coordinate system with its origin coincident with the vortex axis in a YZ plane (positive counter-clockwise starting from the positive z direction)
μ_W	dynamic viscosity of water
ρ_P	density of the seed particles
ρ_W	density of water
σ_{ax}	mean of the standard deviations of vortex axis coordinates in the Y and Z directions
σ_Y	standard deviation of vortex axis in the Y direction
σ_Z	standard deviation of vortex axis in the Z direction

$\sigma_{\lvert\mathbf{U_{VPM}}\rvert}$	standard deviation of the magnitude of the vortex planar movement velocity
$\sigma_{\lvert\mathbf{U_{def}}\rvert}$	standard deviation of the magnitude of the vortex axis deformation velocity
τ_P	time constant of the seed particles with respect to the fluid motion (Equation 3.5)
$\boldsymbol{\omega}$	vorticity vector (Equation 2.2)
ω_n	angular frequency
ω_x	vorticity in the X direction
$\mathbf{\Omega}$	rate of rotation tensor (*i.e.*, the antisymmetric component of the velocity gradient tensor)

Other Notation

$'$	RMS fluctuations
$\langle\quad\rangle$	ensemble averaged
$\lvert\quad\rvert$	magnitude
$\lVert\quad\rVert$	Euclidean norm

Acronyms

CCD	charge-coupled device
DNS	direct numerical simulation
ILS	integral length scale
ITTC	international towing tank conference

LIF	laser induced fluorescence
PIV	particle image velocimetry
PDF	probability density function
PLSF	planar least squares fit
RMS	root mean squared
SPIV	stereo particle image velocimetry

Chapter 1

Introduction

Wing-tip vortices are rotating fluid structures found behind the wing-tips of all conventional fixed wing aircraft while their wings are producing lift. They result in a reduction of the aerodynamic efficiency of the aircraft generating them and can be powerful enough to pose a significant hazard to other aircraft nearby. Over the past century, considerable scholarship has been devoted to understanding the structure and behaviour of wing-tip vortices as well as to developing strategies for their alleviation. Given that a significant motivation for studying wing-tip vortices is to better understand their properties in real world situations it is prudent to consider the effects of the conditions they are likely to encounter. Wing-tip vortices encounter turbulence of a wide variety of length scales and intensities in the atmosphere. Consequently, an important research goal in the study of wing-tip vortices is the influence of turbulence of different length scales and intensities on wing-tip vortices.

Analytic, computational and experimental studies of wing-tip vortices have provided insights into wing-tip vortex structure and behaviour. Experimental studies have consistently found that the path of a wing-tip vortex axis does not remain straight behind the wing-tip but bends as a result of what is termed vortex wandering. There is no consensus on the exact cause or combination of causes of vortex wandering in the literature. There is a dearth of high-quality experimental studies investigating vortex wandering, and, in particular, the influence of freestream turbulence on vortex wandering. Many of the studies that have been conducted have been limited to point measurements of velocity.

The primary objective of this thesis was to study a wing-tip vortex under various freestream turbulence conditions. The streamwise evolution of the vortex was also of interest. Wandering of the vortex and the velocity profiles across the vortex were the focus of the analysis. To accomplish this, an isolated wing-tip vortex was investigated in a water tunnel under three freestream conditions. Grid turbulence generators were used to vary the turbulence intensities and the length scales of the most energetic turbulent eddies. Because of the limitations of the apparatus used, it was not possible to match the ratio of length scale of atmospheric turbulence to wing chord length, which may be on the order of magnitude of 10 (Spalart, 1998), whereas in the laboratory study this ratio was of the order of 0.1. Velocity measurements were collected in an area encompassing the wing-tip vortex using stereo particle image velocimetry (SPIV).

In order to study the velocities in a wing-tip vortex, it is important to identify the vortex axis location at the time each measurement is taken. An additional thrust of the current research was to compare several different means of identifying the vortex axis location and to determine which was most suitable to the experimental conditions of this study. Using the vortex axis locations, the movement of the vortex axis under the different freestream turbulence conditions was quantified. Characteristic velocity and circulation profiles across the vortex were examined at various distances downstream of the wing and for the different freestream turbulence conditions.

In addition to SPIV measurements, images of laser induced fluorescence (LIF) from dye that was injected into the flow at the wing-tip were also used to examine vortex characteristics. Using two simultaneous LIF images taken from different positions, it was possible to reconstruct the three dimensional shape of the vortex axis. The angle of inclination of the vortex axis to the streamwise axis and the vortex axis location itself were quantified using these reconstructions. High-speed LIF images were taken in a plane perpendicular to the streamwise axis and the dye patterns created by the vortex analysed in order to identify the movement of the vortex axis location with high frequency resolution.

Chapter 2

Background and literature review

2.1 Fundamentals of wing-tip vortices

To properly discuss wing-tip vortices, we must first be clear on what we mean by the term *vortex*. There is not one universally accepted definition of a vortex but many that emphasize different features that can be associated with vortices. For the purpose of this thesis, the following simple and elegant definition will be used:

> A vortex exists when instantaneous streamlines mapped onto a plane normal to the vortex core exhibit a roughly circular or spiral pattern, when viewed from a reference frame moving with the centre of the vortex core (Robinson, 1990, p. 23).

A *wing-tip vortex* is a vortex resulting from the fluid flow around the free tip of a finite wing while generating lift. Wing-tip vortices are generated both by natural structures (*e.g.*, the wings of birds and the pectoral fins of some whales) and by man-made structures (*e.g.*, aircraft wings and windmill blades). The focus of this thesis is on the wing-tip vortices found behind conventional aircraft while their wings are producing lift.

2.1.1 Wing-tip vortex formation

Wing-tip vortices are generated by pressure differences on the two surfaces of a finite wing generating lift. An approximation of the change in pressure from the pressure surface to the suction surface on a simple finite wing is shown in Figure 2.1. Moving from the wing-tip inboard there is both a decrease in pressure on the suction surface and an increase in pressure on the pressure surface resulting in an increasing magnitude of the pressure difference across the wing. As a consequence of the spanwise pressure gradient, a spanwise component of velocity is induced in the fluid passing

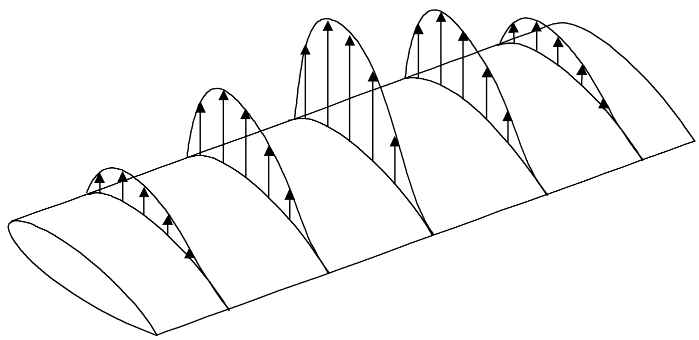

Figure 2.1: Change in pressure across a simple finite wing (reproduced from Bailey, 2006).

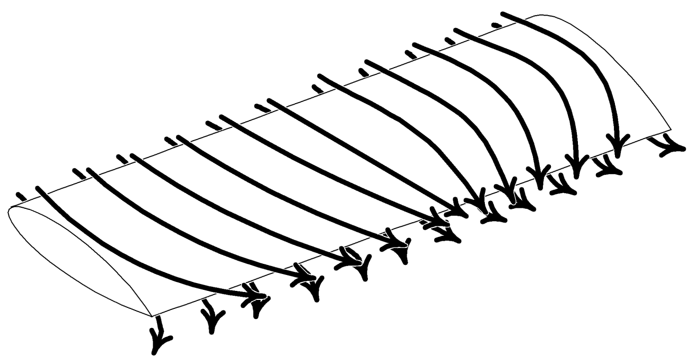

Figure 2.2: Spanwise flow due to the pressure variation across a simple finite wing (reproduced from Bailey, 2006).

over both surfaces of the wing; outboard on the pressure surface and inboard on the suction surface (Figure 2.2). At the wing-tip, fluid rolls from the pressure surface around the tip toward the suction surface setting up a rotating flow behind the wing termed a wing-tip vortex. Behind the trailing edge of the wing a shear layer is produced where fluid from above the wing with an inboard velocity component meets fluid from below the wing with an outboard velocity component. Downstream of the wing this high vorticity layer of fluid wraps around the wing-tip vortex in a process referred to as the roll-up of the vortex (Figure 2.3).

2.1.2 Adverse effects of wing-tip vortices

The rotation of wing-tip vortices is such that the fluid velocity which is induced by the vortex inboard of the wing-tip is in the opposite direction of lift. This induced flow

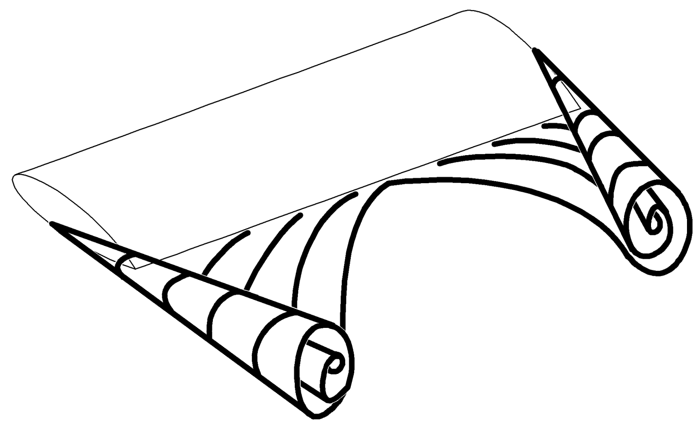

Figure 2.3: Roll-up of the shear layer behind a simple finite wing (reproduced from Bailey, 2006).

behind the trailing edge of the wing is known as downwash. Downwash effectively reduces the angle at which the wing encounters the freestream (*i.e.*, reduces the wing's angle of attack α). Consequently, the total lift is lower and the drag is higher than would be without wing-tip vortices. Additional drag due to wing-tip vortices is known as induced drag or vortex drag. Induced drag on a transport aircraft travelling under typical flight conditions makes up approximately 40 % of the total drag (Kroo, 2001). Under high-lift conditions at take off and landing this percentage may be significantly higher. With the airline industry spending an estimated \$ 214 billion on fuel in 2013 (International Air Transport Association, 2013), even slight improvements in aircraft efficiency through the reduction of drag would be highly valuable both from an economic standpoint and an environmental one.

Wing-tip vortices also pose a hazard to other aircraft travelling in the vicinity of the generating aircraft. Velocities in the vortex core of large transport aircraft can be up to 360 km/h and can remain coherent for up to 30 km behind the aircraft (Breitsamter, 2011). The primary concern in an aircraft encountering a strong wing-tip vortex is the rolling moment that is induced as it may exceed the capacity of the aircraft's control mechanisms to counteract (Widnall, 1975). In order to mitigate this risk, minimum separation requirements have been developed for different leading and trailing aircraft configurations and are used as guidelines for aircraft spacing. This limits the capacity of busy airports and increases the cost of their operation.

2.1.3 Wing-tip vortex break down

The state of wing-tip vortices behind aircraft is of high practical importance given the hazard that they pose to other aircraft. The strength of a vortex is defined as the circulation along a closed curve C that surrounds the vortex

$$\Gamma = \oint_C \mathbf{U} \cdot \mathbf{dl}, \tag{2.1}$$

where $\mathbf{U}$ is the velocity vector and $\mathbf{dl}$ is an infinitesimal length along C. By virtue of the Stokes theorem, Γ can also be expressed in terms of the vorticity vector

$$\boldsymbol{\omega} = \nabla \times \mathbf{U}, \tag{2.2}$$

as

$$\Gamma = \iint_S \boldsymbol{\omega} \cdot \mathbf{dA}, \tag{2.3}$$

where S is any surface bounded by the closed curve C and $\mathbf{dA}$ is an infinitesimal area on the surface S. According to the first Helmoltz theorem (Helmholtz, 1858/1867), in the absence of viscous forces, the vortex strength would remain constant along its length.

For the purposes of this discussion, $\Gamma(r)$ will refer to the circulation along the perimeter of a circle with radius r and centred on the vortex axis. In inviscid flows, Helmholtz second theorem states that vortices cannot end in the fluid but must either form connected circuits, extend to infinity or terminate on an immersed solid wall. With this in mind, in the case of a wing-tip vortex, the wing, around which Γ is non-zero, can be viewed as a continuation of the vortices emanating from each tip. When a wing accelerates from standstill, it begins generating lift and a ‘start-up vortex’ is formed behind it that connects the wing-tip vortices so that a closed vortex loop is formed. The model of a single continuous vortex is a simplified view, however, as it does not take into account the continuous shedding of vorticity over the span of the trailing edge of the wing nor the viscous effects that are important to understanding wing-tip vortices and their evolution in the real world flows.

In flight, the vortex system is complex and the strengths of the vortices behind the wing are affected by the growth of instabilities as well as the action of viscous forces. Spalart (1998) gives two hypotheses which describe the process by which the strength of wing-tip vortices is reduced to a level at which they do not pose a hazard for other aircraft: "stochastic collapse" (p. 120) and "predictable decay" (p. 119). Under the stochastic collapse hypothesis, vortex degradation is primarily accomplished during a single event when atmospheric turbulence excites a catastrophic instability in the vortex. The instability deforms the vortex and, once sufficient deformation has occurred, the energy contained in it cascades to smaller scale structures. The predictable decay model holds that the constant action of viscous forces and other mechanisms whose effects on the decay of the vortex are consistent for a given set of conditions (*e.g.*, some cooperative instabilities) gradually drain energy from the vortex until it is no longer strong enough to pose a threat to other aircraft.

2.2 Roll-up of the wing-tip vortex

Many characteristics of wing-tip vortices are determined during the vortex formation process. Wing-tip geometry, surface roughness, angle of attack α, aspect ratio A, chord based Reynolds number Re_c, airfoil shape, and wing sweep are all important factors that influence the characteristics of the vortex. If sharp corners or edges exist along the wing, additional vortical structures may be shed from these locations. Modern commercial aircraft have many discontinuous features over the span of a wing (most significantly, flaps, and nacelles) producing a wake vortex system behind the wing containing multiple discrete vortical structures to roughly 10 chord lengths c downstream of the wing (Breitsamter, 2011). If we, instead, consider a simpler system where there are no vortex-shedding discontinuities over the span of the wing, multiple vortices may still be present as the vortex generated by the wing-tip, itself, may initially be composed of multiple vortices (*e.g.*, Anderson & Lawton, 2003; Bailey, Tavoularis, & Lee, 2006). Birch, Lee, Mokhtarian, and Kafyeke (2003) found that the multiple vortices generated at the wing-tip merged quickly and the merging was almost complete by the time they reached the trailing edge. In addition to discrete vortical structures, the shear layer that develops at the trailing edge of the wing accounts for much of the vorticity that is contained in the primary vortex further downstream. By $2c$ downstream of the wing, the shear layer would likely complete its roll-up and merge with the wing-tip vortex to the extent that the vortex would be

Table 2.1: Classification of stages of wing-tip vortex evolution (following Breitsamter, 2011).

Streamwise location	Stage of wing-tip vortex evolution
$X/c = \mathcal{O}(1)$	Near field
$X/c \leq 20$	Extended near field
$20 < X/c \leq 200$	Mid/far field
$200 < X/c$	Decay region

essentially axisymmetric (Green & Acosta, 1991).

In this thesis, periods of vortex development were classified according to Breitsamter (2011). Accordingly, the period which occurs immediately downstream of the wing's trailing edge ($X/c < 1$) will be referred to as the near-field. Other classifications are summarized in Table 2.1.

2.3 Azimuthal velocity variation

After the wake-vortex system and the shear layer behind the wing have rolled up into a single vortex, the velocity field becomes roughly axisymmetric (this occurs in the extended near field). At this stage, wing-tip vortices are commonly approximated as consisting of an inner core region which rotates as a rigid body with azimuthal velocity U_θ proportional to the radius ($U_\theta \propto r$) and an outer region which rotates like a potential vortex with azimuthal velocity proportional to the inverse of the radius ($U_\theta \propto {}^1\!/r$). The Rankine vortex model is a simple model which behaves exactly in this manner with the two profiles meeting at a sharp corner (see Figure 2.4).

In reality, an intermediate zone exists between the core and the outer region of the vortex. Spalart (1998) specifies two radii which are important in characterizing the azimuthal velocity in a wing-tip vortex. The first, denoted as r_{max}, is the radius at which the azimuthal velocity reaches its peak. The second, denoted as r_{inv}, is the radius at which the profile begins to decrease proportionally to the inverse of the radial position.

The importance of these radii is further illuminated by examining the profile of $\Gamma(r)$ across the vortex. From Lord Rayleigh's work in 1917, we know that, in the inviscid case, a vortex would be stable to axisymmetric disturbances wherever the

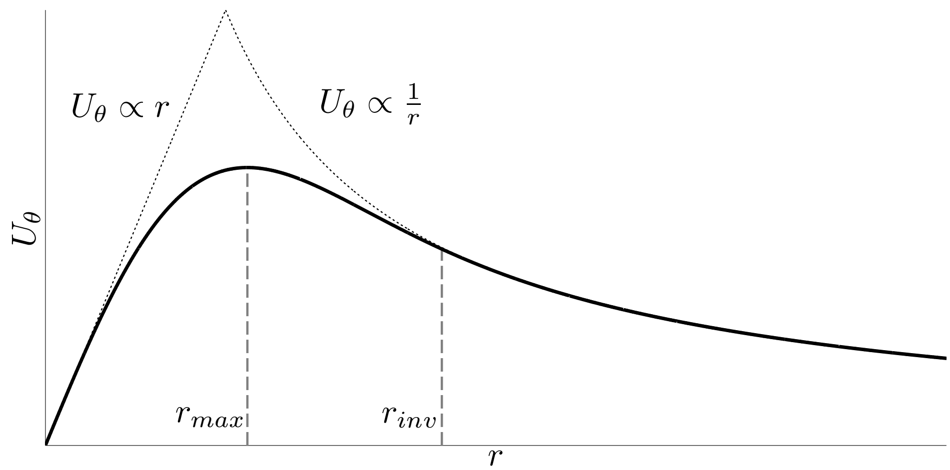

Figure 2.4: Typical radial profile of azimuthal velocity compared with $U_\theta \propto r$ and $U_\theta \propto {}^1\!/r$.

magnitude of the circulation profile increases with radial position. In the inner region of the vortex, where U_θ increases proportionally to r, the increase of $\Gamma(r)$ is also proportional to r and the vortex is stable to axisymmetric disturbances. Beyond the inner region of the vortex, it was traditionally held that the profile of U_θ asymptotically approaches that of a potential vortex from below with its slope never becoming steeper than ${}^1\!/r$ and, consequently, circulation continues to increase with radial distance from the vortex axis eventually approaching a constant value. An example of such a model is the Lamb-Oseen vortex model which is often used to approximate a wing-tip vortex. Its azimuthal velocity profile has the form:

$$U_\theta(r) = \frac{\Gamma_o}{2\pi r}\left(1 - e^{-r^2/r_o^2}\right), \tag{2.4}$$

where r_o is the core radius and Γ_o is the total circulation of the vortex (*i.e.*, $\Gamma_o = \lim_{r\to\infty} \Gamma(r)$, assuming an isolated vortex). Since the circulation is strictly increasing (*i.e.*, U_θ always decreases more slowly than the potential vortex model) a Lamb-Oseen vortex is stable to axisymmetric disturbances at all radial locations. The Lamb-Oseen model, however, makes the significant simplification that there is no variation in axial flow across the vortex. Batchelor (1964) gives a more complete model, known as the Batchelor vortex, which takes into account an axial velocity surplus or deficit using a similarity solution. Batchelor (1964) was studying a wing-tip vortex far downstream of the wing where its decay is due entirely to the effects of viscosity. Moore and Saffman (1973) point out that the similarity solutions he used were only valid at downstream distances of at least $\mathcal{O}(10^3 c)$. A simplified version of the Batchelor vortex, called the q-vortex has commonly been used in analytic studies of wing-tip vortices. The q-vortex model, removes the dependence of the Batchelor vortex on the distance downstream of the wing making it similar to a Lamb-Oseen model with a Gaussian axial velocity field imposed across the vortex (Jacquin, 2005). Moore and Saffman (1973) suggest another model which, like Batchelor's, is valid at locations far downstream of the wing, however, better approximates the true behaviour of wing-tip vortices near the wing. Recent experimental work using a rounded tip NACA 0012 wing in a water tunnel has confirmed that the velocity profiles predicted by Moore and Saffman's model match measured velocity profiles much more closely than Batchelor's model in the extended near field (del Pino, Parras, Felli, & Fernandez-Feria, 2011).

The linear dynamics of wing-tip vortices have been studied extensively. The standard approach has been to introduce perturbations in the form of Kelvin waves which can be characterized by the velocity and pressure fluctuations that initiate them

$$({U_x}', {U_r}', {U_\theta}', p') = \left(\hat{U_x}, \hat{U_r}, \hat{U_\theta}, \hat{p}\right) e^{i(k_w X + m\theta - \omega_n t)}, \tag{2.5}$$

where U_x is axial velocity, U_r is radial velocity, p is pressure, k_w is the axial wave number, m is the azimuthal wave number, and ω_n is the angular frequency. The azimuthal wave-number of the disturbance m characterizes the modal shape (Breitsamter, 2011). The aforementioned axisymmetric disturbances correspond to the $m = 0$ mode, however, positive-m modes may also excite instabilities in some cases (Jacquin, 2005). In general, the stability of an isolated wing-tip vortex is closely related to the deficit or surplus ΔU_x (positive for a deficit and negative for a surplus) of axial velocity in the core with respect to the freestream. Stability of a vortex is often examined in terms of the swirl parameter

$$q_s = \frac{\Gamma_o/2\pi r_o}{\Delta U_x}. \tag{2.6}$$

Analysis of a q-vortex shows that, for a value of $q_s = 1.5$, the vortex core would be fully stable, whereas it would become less stable with increasing axial velocity, until, for $q_s = 0.7$, it would be unstable over the entire core (Jacquin, 2005). Several numerical studies have also found evidence that, in the presence of axial flow, the circulation does not increase monotonically with increasing radial distance from the vortex axis (*e.g.*, Pantano & Jacquin, 2001; Ragab & Sreedhar, 1995). These studies show that the circulation of the vortex reaches a maximum higher than Γ_o at a certain radial distance from the vortex axis. The existence of a circulation overshoot region in wing-tip vortices has been debated in the literature, as some authors cite numerical evidence of its presence (*e.g.*, Jacquin & Pantano, 2002; Pradeep & Hussain, 2010), while others find insufficient experimental evidence to infer its existence in physical flows (Spalart, 1998).

2.4 Axial velocity

Batchelor (1964) showed that, in the inviscid case, the pressure in the core of a wing-tip vortex would be less than that in the freestream upstream of the wing so that fluid particles from upstream of the wing would accelerate in the downstream direction as they enter the vortex core causing a surplus in axial velocity with respect to the free stream. Moore and Saffman (1973) proposed that, in viscous flows, the boundary layer of the wing produces a fluid flux deficit into the vortex core which tends to slow the axial velocity in opposition to the trend described by Batchelor for the inviscid case. Neglecting other factors, an axial velocity deficit would tend to be smoothed out by viscous interaction with the freestream. The effect of the viscous dissipation on the axial flow defect in the vortex core becomes significant only far downstream of the wing, beyond a distance from the wing estimated by Moore and Saffman (1973) to be roughly $0.01cRe_cA^2$.

In addition to these general mechanisms, various other factors influence axial flow in the vortex core, however, the precise mechanisms by which the axial defect is controlled are not well understood. Axial velocities both higher than the freestream velocity U_∞ (jet-like flow) and lower than U_∞ (wake-like flow) have been observed in experimental studies (Anderson & Lawton, 2003). Lee and Pereira (2010) identified the wing-tip shape, α, Re_c, the roughness of the wing's surface, A, and airfoil shape as important factors and were able to generate both jet-like and wake-like flows behind a square-tipped NACA 0012 wing by adjusting only α.

2.5 Vortex wandering

Wing-tip vortex wandering or meandering refers to the movement of the vortex axis in a transverse-spanwise plane. This phenomenon has been observed in experimental studies for decades (*e.g.*, Baker, Barker, Bofah, & Saffman, 1974). Devenport, Rife, Liapis, and Follin (1996) found that the amplitude of wandering motions increases with the distance downstream of the wing. There has yet to be a consensus on the specific cause or combination of causes of these motions, however, several explanations are commonly encountered in the literature. In cases where a pair of wing-tip vortices are present, cooperative instabilities are known to deform the vortex axis (*e.g.*, Crow, 1970). In the case of an isolated vortex, some early studies (*e.g.* Baker et al., 1974) suggest that wandering is primarily due to the interaction of the vortex with freestream turbulence. More specifically, Jacquin, Fabre, Geffroy, and Coustols (2001) suggest that asymmetric inertial waves in the vortex may be excited by freestream turbulent structures. Alternatively, in wind and water tunnel experiments, it is also possible that some wandering may be produced as the vortex interacts with the image vortices produced by the walls (Beninati & Marshall, 2005). It has also been proposed that vibrations in the vortex generator itself could be to blame for the wandering of the wing-tip vortex in wind and water tunnel studies (Jacquin et al., 2001). Biot-Savart induction, by which a vortex induces velocity at other points in the flow field, may play a role in vortex wandering. In cases where Kelvin-Helmholtz instabilities in the shear layer behind the trailing edge of the wing generate secondary vortical structures, these structures may induce movement of the primary wing-tip vortex (Gursul & Xie, 2000). Self-induced deformation by the Biot-Savart mechanism, as described by Hama (1962), has been suggested by Rokhsaz, Foster, and Miller (2000) to be responsible for vortex wandering. This mechanism, however, has been criticized by some authors (*e.g.*, Iungo, Skinner, & Buresti, 2009) on the grounds that such a mechanism would imply that wandering amplitude would increase with increasing vortex strength, as for example would be the case if α were increased. Though consistent with the findings of the study by Rokhsaz et al. (2000), this is in opposition to the trend found in other prominent studies (*e.g.*, Devenport et al., 1996). Heyes, Jones, and Smith (2004) suggests that the increased wandering at higher angles of attack seen by Rokhsaz et al. (2000) may have been due to flow separation on the wing at higher α. An alternate cause of wandering, given by Green (1995), is that it is a consequence of packets of high vorticity fluid intermittently being ejected from the vortex core, a notion proposed by Bandyopadhyay, Ash, and Stead (1991). Green (1995) suggests that the vortex core responds to these ejections by moving in the opposite direction of the ejection.

For practical purposes, wandering has commonly been considered to be stochastic (Baker et al., 1974). Devenport et al. (1996) developed a method to correct single-point measurements of velocity for vortex wandering by assuming the distribution of vortex axis locations to be a non-isotropic Gaussian function. The assumption that the probability density function (PDF) of the vortex axis locations is Gaussian is questioned by Spalart (1998) who points out that if the wandering caused the vortex axis to form sinusoidal shape the PDF would be non-Gaussian. A subsequent study of a single vortex by Heyes et al. (2004), however, found the PDF of vortex axis locations to be approximately Gaussian. More recently Bailey, Estejab, Robert, and Tavoularis (2011) found evidence that, in addition to the seemingly random wandering of the vortex axis, there may be a helical component to the motion with a long pitch. Interestingly, the pitch of the helical motion appeared to be insensitive to freestream flow conditions.

2.6 Turbulence and wing-tip vortices

In practice, wing-tip vortices encounter a variety of atmospheric conditions. Atmospheric turbulence can include structures with wide ranges of length scales and intensities. Laboratory tests have confirmed the lived experience of those in the aircraft industry that, as a general trend, atmospheric turbulence enhances the decay of vortex pairs (Sarpkaya & Daly, 1987).

Studies of isolated wing-tip vortices have shown that they both interact with the turbulence found in the freestream and may themselves be turbulent in nature at times. Spalart (1998) summarized the sources of turbulence in and around wing-tip vortices along with the likely length scales of their most energetic eddies L (given in Table 2.2, where $\Delta U/U_\infty$ is the turbulent fluctuation velocity normalized by the

Table 2.2: Types of turbulence affecting wing-tip vortices (reproduced from Spalart, 1998, with permission from Annual Reviews through RightsLink, license number 3283220010688)

Source	$\Delta U/U_\infty$	L/b	Extent
Boundary layers (no-slip condition)	1	0.001	To trailing edge
Viscous wakes (streamwise shear)	0.1	0.01	A span
Vortex sheet (lateral shear)	0.1	0.01	A few spans
Rolled-up vortex (circulation)	1	0.1	Possibly many spans
Atmosphere (thermal, shear)	0.01	10	Everywhere

freestream velocity and b is the wingspan). Experimental work by Bandyopadhyay et al. (1991) on split-wing vortices, indicated that the vortex core has periods of both turbulent and laminar behaviour and found that the vortex periodically both ejected and ingested turbulent fluid (see Figure 2.5 for an example of a split-wing configuration). Bandyopadhyay et al. (1991) proposed that rotation of the vortex acts to damp turbulent fluctuations in the fluid it ingests. Results by Devenport et al. (1996), however, indicated that the vortex core was consistently laminar, which implies that there are significant differences in the behaviour and organization of turbulence in split-wing vortices and those generated by a single wing.

A direct numerical simulation (DNS) study by Melander and Hussain (1993) showed that a columnar vortex placed in a field of homogeneous turbulence tends to organize the fine scale turbulence of the turbulent field into thread-like structures of high vorticity which enwrap the primary vortex. As the intensity of the velocity fluctuations in the freestream was increased, the secondary structures went from dissipating downstream at low fluctuation intensity, to remaining intact and causing

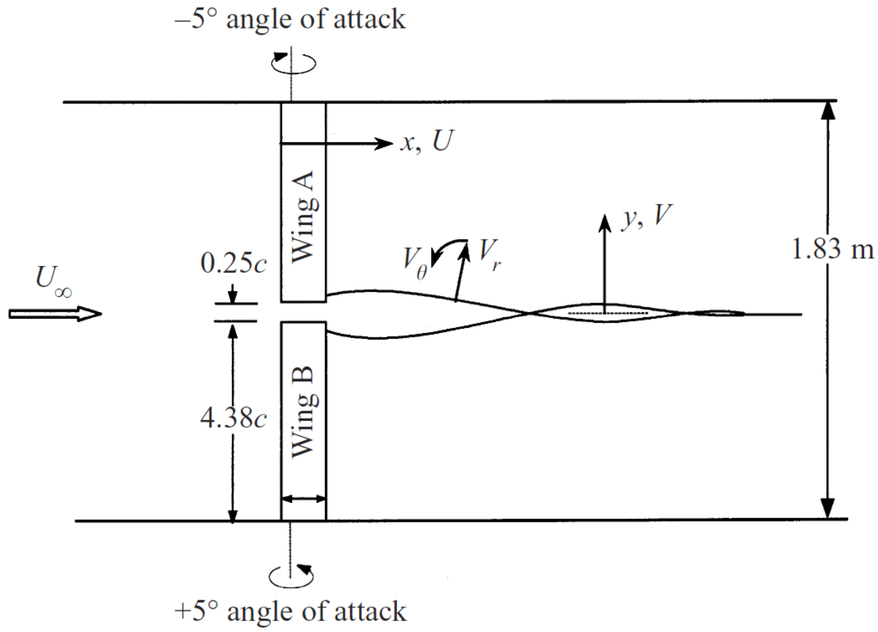

Figure 2.5: Split-wing configuration used by Devenport et al. (1999) (reproduced with permission from Annual Reviews through RightsLink, license number 3287081316735)

the shape of the primary vortex to deform at moderate fluctuation intensity, to causing the primary vortex to be destroyed at high fluctuation intensities. A 2005 DNS study by Takahashi et al. in which a Lamb-Oseen vortex was placed into a homogeneous and isotropic turbulence field that was, itself, generated by a DNS study of decaying turbulence in order to simulate more realistic conditions, also found that the turbulence field organized itself into secondary structures which wrapped around the primary vortex. Holzäpfel et al. (2003) performed a numerical investigation of a vortex in turbulent freestream regimes that would be more commonly encountered by wing-tip vortices (*i.e.*, a stably stratified flow, a jet, and a shear layer), as well as in isotropic turbulence. In all cases secondary structures were found to emerge and wrap around the primary vortex affecting it to different extents based on the characteristics of the freestream regime. Stephan, Holzäpfel, and Misaka (2013) performed a numerical investigation on a pair of counter rotating vortices near a solid boundary and investigated the effect of placing different obstacles on the boundary. They found that secondary structures, specifically horseshoe vortices, generated by the boundary and obstructions wrap around the vortices and significantly accelerate their decay.

An experimental study by Sun and Marshall (2000) investigated the interaction of a vortex with the wake of a spherical object and found, similarly, that the wake of the sphere wound thin vortical structures around the primary vortex. In cases where the strength of the secondary structures was significant with respect to the primary vortex, the vortex core size was observed to vary in response to their perturbations and, if they were sufficiently strong, the primary vortex was observed to eject fluid from its core or break down completely. The observation of core fluid being ejected from the primary vortex due to its interaction with secondary structures is in agreement with the findings of the previously mentioned experimental study by Bandyopadhyay et al. (1991). Marshall (1997) numerically investigated the interaction of a series of secondary structures in the form of vortex rings placed around a columnar vortex and also observed packets of high vorticity fluid being ejected from the core. In another numerical study, however, Marshall and Beninati (2005) tracked the exchange of core fluid with the freestream by introducing a passive scalar into the core and found that no core fluid ejection events occurred.

2.7 Axis identification from planar velocity fields

Planar velocity data obtained from particle image velocimetry (PIV) or numerical simulations are commonly used to study wing-tip vortices. In order to study the velocity characteristics of a vortex, coordinates must be specified relative to the vortex axis. If the vortex axis moves in the measurement window, ensemble averaging of the velocity fields in the reference frame of the measurement window would differ significantly from the ensemble averaged velocity field taken in a reference frame in which the vortex axis coordinates are fixed. By moving the frame of reference with the vortex axis, the actual velocity field in the vortex can be obtained (Figure 2.6).

Many methods for identifying the location of the axis of a vortex from PIV data have been suggested and numerous studies comparing the effectiveness of various methods have been conducted (*e.g.*, Carmer, Konrath, Schröder, & Monnier, 2008; Jiang, Machiraju, & Thompson, 2005; van der Wall & Richard, 2006) but no one practice has become an accepted standard. Based on the definition of a vortex given by Robinson (1990) (see Section 2.1), identifying the vortex axis by locating the centre

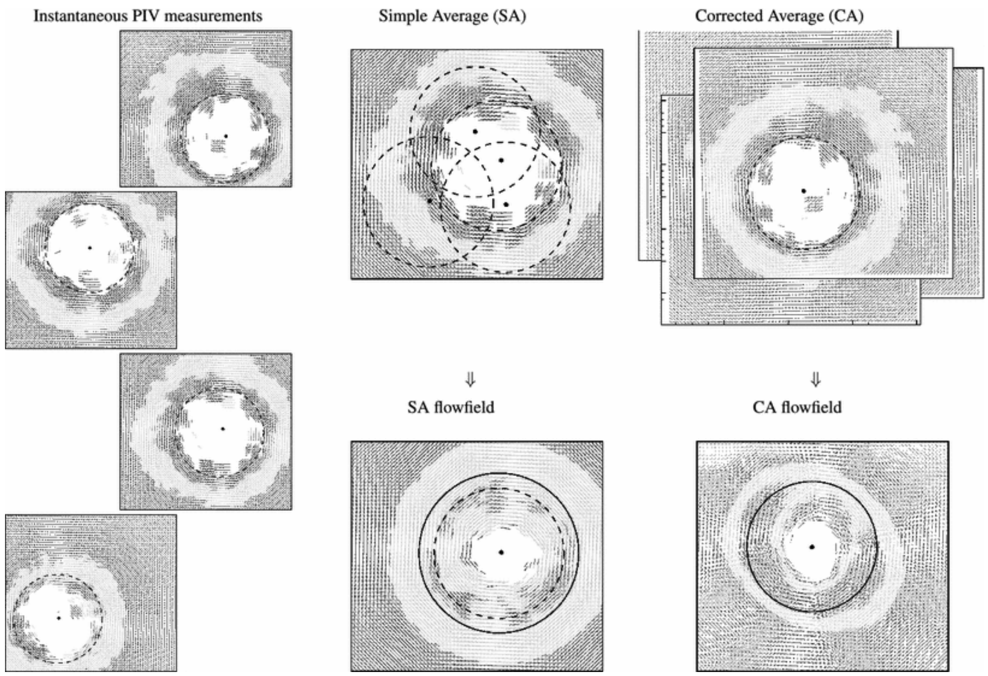

Figure 2.6: Comparison of planar velocity fields averaged with and without correcting for the vortex axis location (from Bhagwat & Ramasamy, 2012, with permission from Springer through RightsLink, license number 3281511503623).

about which the streamlines are circling or spiralling out from seems a very simple and direct method. Robinson (1990), however, requires that the frame of reference that the streamlines are viewed in be moving with the vortex. As Jiang et al. (2005) point out if a vortex keeps moving with respect to the observer's frame of reference, the streamlines would be deformed and their centre may no longer indicate the location of the vortex axis. Consequently, to implement an accurate vortex identification scheme we either need a priori knowledge of the movement of the vortex or a Galilean invariant technique.

A common class of methods rely on Galilean invariant scalar parameters extracted from the velocity field to indicate the location of the vortex axis. Older studies commonly used the magnitude of the component of $\boldsymbol{\omega}$ (Equation 2.2) that is normal to the measurement plane ω_x to indicate the location of the vortex axis (Hussain & Hayakawa, 1987). By using ω_x, however, it is difficult to distinguish between rotation in a vortex and shear (Jeong & Hussain, 1995). For this reason, this approach is no longer in common use. Several popular indicator parameters are derived from the velocity gradient tensor $\nabla\mathbf{U}$. Hunt, Wray, and Moin (1988) use the second invariant of $\nabla\mathbf{U}$ (commonly referred to as Q) to indicate the location of a vortex. They define a vortex as a connected region with positive values of Q. Decomposing $\nabla\mathbf{U}$ into its symmetric component $\mathbf{S}$ (*i.e.*, the rate of strain tensor) and antisymmetric component $\mathbf{\Omega}$ (*i.e.*, the rate of rotation tensor), Q can be calculated as

$$Q = \frac{1}{2}\left(\|\mathbf{\Omega}\|^2 - \|\mathbf{S}\|^2\right) = \frac{1}{2}\left(tr\left(\mathbf{\Omega}\mathbf{\Omega}^t\right) - tr\left(\mathbf{S}\mathbf{S}^t\right)\right). \tag{2.7}$$

Jeong and Hussain (1995) proposed instead that a vortex core region could be defined as a region in which the tensor $\left[\mathbf{S}^2 + \mathbf{\Omega}^2\right]$ has two negative eigenvalues. This method implies that λ_2 (the second largest eigenvalue of $\left[\mathbf{S}^2 + \mathbf{\Omega}^2\right]$) is negative and is commonly referred to as the λ_2 method. A study by Zhou, Adrian, Balachandar, and Kendall (1999) introduced the swirling strength SS parameter which is defined as the imaginary part of the complex eigenvalue of $\nabla\mathbf{U}$ where a complex eigenvalue exists. Carmer et al. (2008) point out that, in two dimensional flows, the magnitudes of Q, λ_2, and SS would be proportional to each other.

It is sometimes possible to identify the location of the vortex axis by finding the maximum or minimum value of one of these indicator parameters (van Jaarsveld, Holten, Elsenaar, Trieling, & van Heijst, 2011). In many cases, however, an indicator parameter field may contain multiple peaks or many cells in the core region with comparable values of a parameter instead of a single peak (van der Wall & Richard, 2006). As an alternative to locating a single peak value, a centre of mass calculation may be done to obtain an estimate of the vortex axis location by using one of the indicator parameters as the mass (van der Wall & Richard, 2006). If the expected distribution of an indicator parameter across the vortex is known, the vortex axis may be identified by comparing the expected profile to the measured data. Schram, Rambaud, and Riethmuller (2004) opt for a wavelet based approach by assuming that the vorticity across the vortex can be described by a Gaussian function and using the Ricker wavelet (a.k.a. the Mexican hat wavelet) to analyse the velocity field. In another study, Bhagwat and Ramasamy (2012) developed a technique that identified the vortex axis location by comparing the measured azimuthal velocity field to a known theoretical profile (they used the Lamb-Oseen profile) and performing a least-squares fit by adjusting the vortex axis location coordinates to minimize the discrepancy between the measured and theoretical velocities.

Chapter 3

Apparatus and methods

All measurements in this study were taken in a recirculating water tunnel facility at the University of Ottawa. A square-tipped wing with a NACA 0012 airfoil shape was mounted in the water tunnel to generate a wing-tip vortex. The turbulent characteristics of the flow were adjusted by inserting square turbulence generating grids upstream of the test section. Two measurement techniques were used to investigate the flow in and around the wing-tip vortex: stereo particle image velocimetry (SPIV) and laser induced fluorescence (LIF). Data analysis was performed using MATLAB along with software provided by the manufacturer of the SPIV system (Davis software, LaVision Inc.).

3.1 Wing

A square-tipped NACA 0012 wing with a chord length $c = 0.178$ m and a semi-span $b/2 = 0.298$ m was used to generate a wing-tip vortex in the water tunnel (Figure 3.1). The wing was mounted with its root at the surface of the water and the spanwise dimension of the wing proceeding vertically downward. The wing was mounted so that the quarter-chord position (from the leading edge) was in the centre of the tunnel and the tip of the wing was 397 mm ($2.23c$) above the tunnel floor. The wing's angle of attack was adjustable and, when changed, rotated about the quarter-chord position. All measurements were collected with an angle of attack of 5°.

Free-surface effects at the root of the wing were kept low by mounting the root of the wing on a thin circular aluminium plate with a diameter of 280 mm ($1.6c$). The suction surface of the wing was equipped with a boundary layer trip wire, 1 mm ($0.006c$) in diameter, in an effort to trigger transition of the boundary layer from a laminar to a turbulent regime.

The wing was constructed with an internal fluid reservoir near its tip, which was

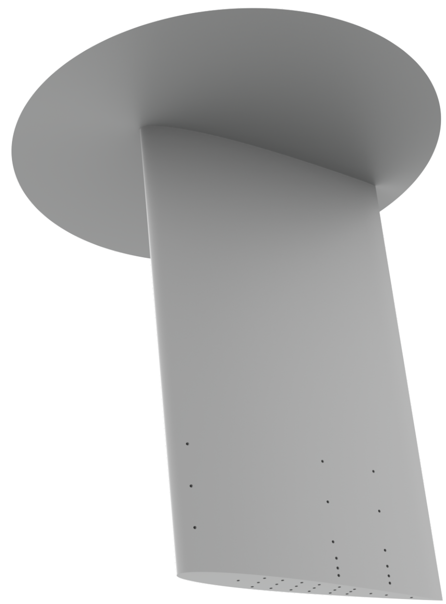

Figure 3.1: NACA 0012 square-tipped wing, showing the injection holes.

fed through a hose connected to the root of the wing. The reservoir fed 0.4 mm diameter holes near and on the wing-tip which could be used to inject water carrying dye or particles into the flow. Some or all of the holes were blocked (covered with tape) during some tests. Dye- and particle-seeded fluid was supplied from tanks below the tunnel which were pressurized using a compressed air line.

3.2 Water tunnel

The water tunnel consisted of a large settling chamber at the upstream end of the test section, a 4 m long test section, a recovery tank downstream of the test section, and a recirculation system where water from the recovery tank was pumped back to the settling chamber by an axial pump (Figure 3.2). The total volume of the tunnel was approximately 15 m^3. Water was circulated through the system using an axial pump powered by a 5.6 kW variable speed electric motor.

The outlet from the water recirculation piping was located at the farthest upstream

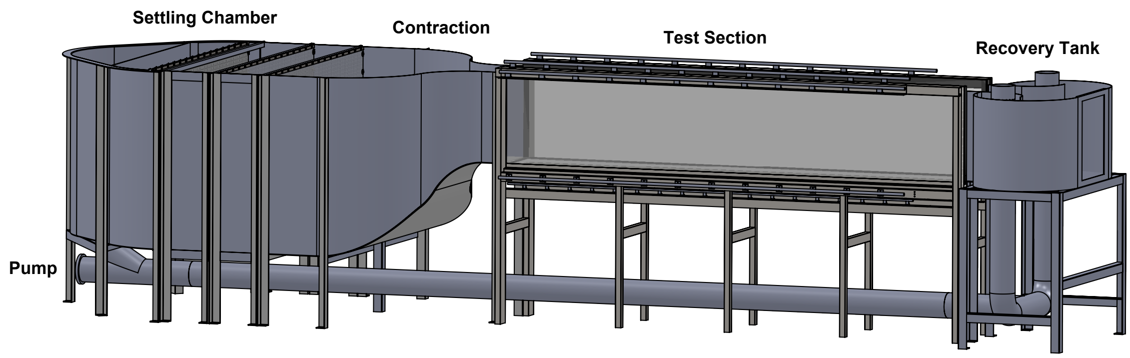

Figure 3.2: Water tunnel facility.

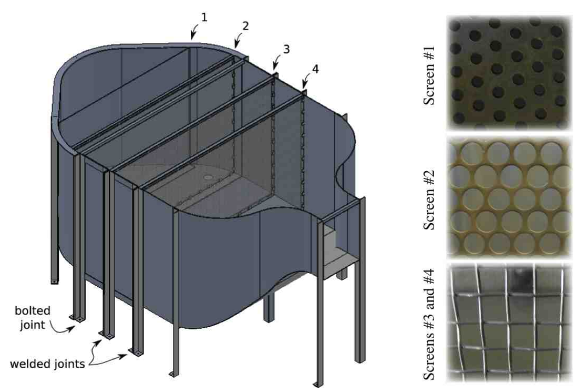

Figure 3.3: Screens in the upstream settling tank (reproduced from Vanderwel, 2011).

end of the settling chamber, which consisted of a perforated vertical pipe. The flow from the outlet generated strong large scale vortices, which were broken down by several layers of 5 cm thick coarse pond filter sheets, followed by four screens with decreasing solidities (ratio of closed to open area) located inside the settling chamber. The water entered the test section through a 10:1 contraction (Figure 3.3, filter medium not shown in the figure). The use of the filters, screens, and contraction resulted in a sufficiently uniform, low turbulence flow for this study.

The test section side walls and bottom were made of glass, which allowed uninterrupted viewing along the full test section length. The water surface was free of cover. The test section was 550 mm (3.1c) wide and the depth of the water in the test section was kept constant for all measurements at 700 mm (3.9c). Work by Vanderwel (2011) showed that the tunnel floor's boundary layer was laminar and extended to a thickness of approximately 100 mm (0.6c) at the furthest downstream measurement location used in this study, which was 300 mm below (1.7c) below wing tip.

Downstream of the test section was a recovery tank where the water leaving the test section was collected and directed to the recirculation piping. The recirculation piping passed under the main test section and took water to the upstream settling tank through an axial pump, which was located underneath the upstream settling tank. The recovery tank contained an additional outlet which was connected to a filtration system that consisted of a puck chlorination system and filters which removed particles down to 5 μm in diameter. Chlorination and filtering were activated by a timer while the tunnel is not in use.

3.2.1 Turbulence grids

Turbulence generating grids were used to generate freestreams with different turbulence conditions (Figure 3.4). Two grids were used, fabricated from aluminium sheets 3.175 mm thick, with square holes punched out, both having a solidity of 0.44. The mesh sizes of the two grids were $M = 25$ mm (0.14c) and $M = 51$ mm (0.29c), respectively. The grids were inserted into the tunnel at the upstream end of the test section. Measurements were taken using the $M = 0.14c$ grid (the 'small-grid' cases) and the $M = 0.28c$ grid (the 'large-grid' cases), in addition to measurements done with no obstruction placed at the upstream end of the test section (the 'no-grid' cases).

3.3 Dye and seed particles

The fluorescent dye used in this study was an aqueous solution of 2 mg/L rhodamine 6G. Rhodamine 6G was chosen for its low molecular diffusivity, which allowed the vortex structure to be discerned from images of fluorescence. Rhodamine 6G's peak emission occurs at 560 nm, while its peak absorption is at 530 nm (Arcoumanis, McGuirk, & Palma, 1990). The flow was illuminated by a laser light source at a wavelength of 532 nm and images were recorded through a 540 nm long pass filter when it was necessary to separate the dye emission from laser light reflections for image clarity.

Hollow glass spheres (Potters Industries, Sphericel®110P8) were used to seed the

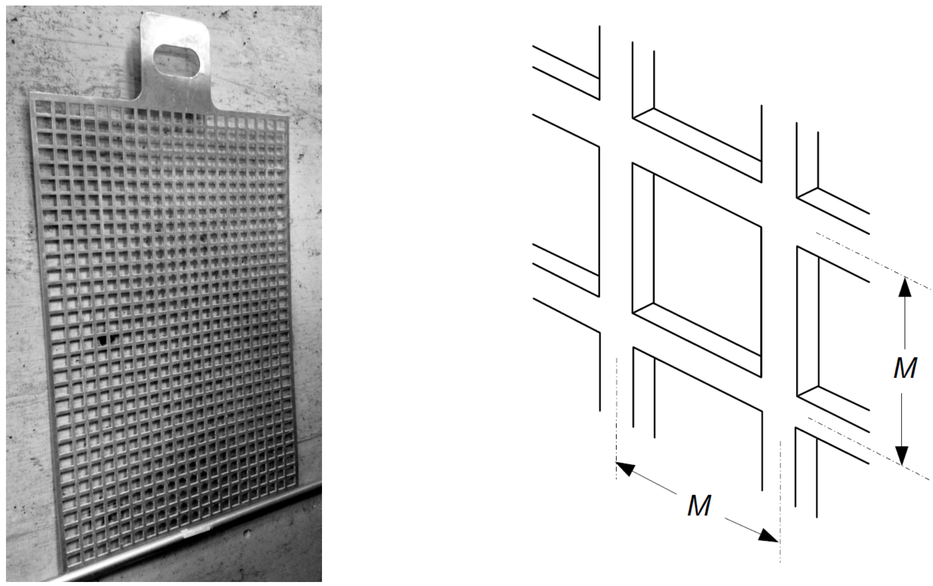

(a) (b)

Figure 3.4: The small grid (a) and definition of the mesh size M (b) (reproduced from Bailey, 2006).

flow for SPIV measurements. The spheres had a specific gravity of 1.10 g/cm^3 and a mean diameter of 11.7 μm. The dynamic properties of the spheres in the water tunnel flow are discussed in Section 3.7.2.

For the injection of both the hollow glass spheres and the Rhodamine 6G, the flow rate of the water carrier was set to a level at which the injected stream appeared to slowly ooze into the boundary layer of the wing and from the wing-tip surface. Higher flow rates, which would have been beneficial for dye visibility and measurement purposes, were avoided because the injected liquid formed jets that extended beyond the wing boundary layer causing it to travel downstream at the periphery of the vortex instead of remaining in its core, as well as causing concern that the injection was significantly affecting the flow.

3.4 Coordinate systems

Positions in the water tunnel are specified in one of two coordinate systems (Figure 3.5). The first is a fixed coordinate system, which has its origin on the wing-tip at the quarter-chord position. Positions in this system are given in Cartesian components X,

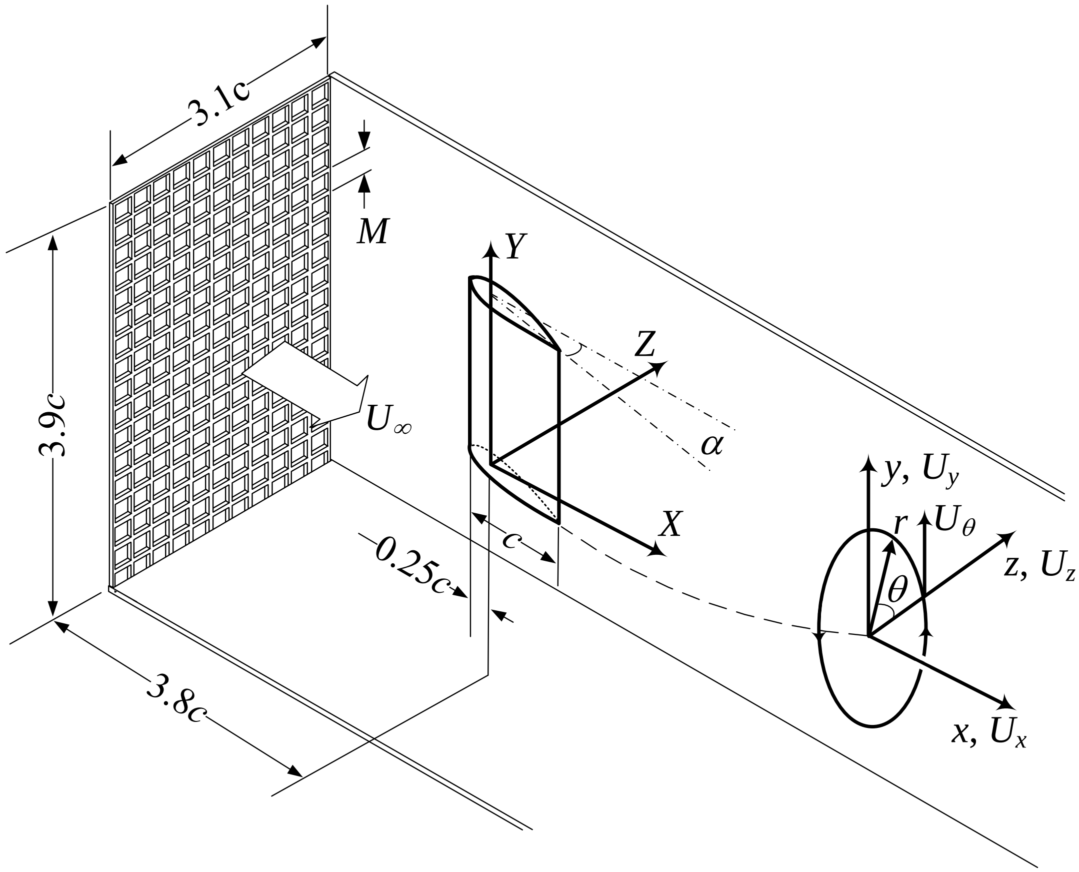

Figure 3.5: Coordinate systems used in this report (adapted from Bailey, 2006).

Y, and Z which, with reference to the wing, correspond to the streamwise, spanwise, and transverse directions, respectively. The origin of the second system is attached to the axis of the wing-tip vortex at the streamwise position where measurements are taken. Coordinates here are specified either as the Cartesian components x, y, and z or as the cylindrical components r, θ, and x (where x is aligned with the streamwise axis of the water tunnel). Velocity components are either given in Cartesian form U_x, U_y, and U_z or in cylindrical form U_r, U_θ, and U_z.

Turbulence grids were inserted at the upstream end of the test section immediately following the contraction at X = -0.68 m (-3.8c). The quarter-chord location of the wing-tip (the origin of the fixed coordinate system) remained at a fixed location with respect to the water tunnel for all measurements.

3.5 Stereo particle image velocimetry

Quantitative data were acquired primarily using SPIV. The system consisted of a New Wave Research Nd:YAG laser light source (model: Solo 120XT), two Imager pro X 4M cameras and FlowMaster software by LaVision Inc.. Double-framed images were recorded at a rate of 4 Hz. The planes of measurement were parallel to the YZ plane and measurements were taken at three planes downstream of the wing, namely, at $X = 0.63$ m, 1.18 m, and 2.28 m ($X = 3.6c$, $6.6c$, and $12.8c$).

3.5.1 SPIV system components

The Nd:YAG laser produced two pulses 3500 μs apart at a rate of 4 Hz. In order to generate a laser sheet in the desired plane, the laser was mounted below the water tunnel and its beam passed through a divergent sheet generator then reflected off a mirror and straight up through the water tunnel so that the laser sheet was parallel to the YZ plane.

To obtain particle images from two independent views of the measurement planes, one camera was mounted on each side of the water tunnel parallel to the bottom of the water tunnel and at an angle of 45° to the corresponding water tunnel wall. A Scheimpflug adapter was used to tilt each camera's focal plane so that it would be coincident with the measurement plane. Significant image distortion would have occurred if the cameras had viewed the air-glass-water interface at the tunnel wall at 45° because of the difference in refractive indices. To avoid this problem, water-filled triangular prisms were attached to the outside of the tunnel walls so that each camera's axis was normal to the air-glass-water interface (Figure 3.6). The cameras then viewed the tunnel wall itself as a water-glass-water interface introducing only a small image distortion. To compensate for this distortion and to calibrate the images from each camera to the true dimensions of the measurement planes, a two-level calibration plate was used (LaVision Inc., 3D Calibration Plate, type 22). It is noted that the movement of particles in the flow were tracked in three dimensions, so what has been so far described as a measurement plane in actuality a thin volume. The thickness of the volume over which the laser light was bright enough to illuminate

Figure 3.6: Arrangement of the cameras and water-filled triangular prisms.

particles to a level that they were discernible by the image processing software was approximately 2 mm.

The Imager pro X 4M cameras have a resolution of 2048 x 2048 pixels and were used in conjunction with Nikon Nikkor 50 mm f/1.8D lenses, set at f/2.8, which allowed an adequate depth of field while also allowing enough light into the camera to generate usable particle images. The lenses were manually focussed on the calibration plate and then subsequently the focus was refined by making minor adjustments so that the particles illuminated by the laser sheet were as distinct as possible. In order to isolate laser light being reflected off the particles from ambient light and other reflections, 532.5 nm bandpass filters (with a transmission below 50 % beyond ± 5 nm from 532.5 nm) were attached to the camera lenses.

3.5.2 Particle image processing

Initial processing of the particle images was done using LaVision Inc.'s FlowMaster software. The software performed the following sequence of operations on the acquired image sets.

1. *Image calibration.* This created a de-warping and scaling function that was applied to all images based on comparing an image of the calibration plate to its known dimensions.

2. *Compensation for image intensity non-uniformity.* A sliding intensity average was subtracted across the image in order to create particle image with more even intensity.

3. *Division of images into interrogation cells and cross correlation of the double framed images.* A three-pass cross correlation was used. The frames were divided into interrogation cells of 64 x 64 pixels for the first pass and 32 x 32 pixels for the second and third passes with a 50 % overlap in each case. If the difference between a given vector and its neighbours was too great it was removed and, in subsequent iterations, replaced only if a vector which was consistent with the surrounding vectors was found. A 3 x 3 cell smoothing filter was also applied here.

4. *Post-processing vector fields.* At positions where the cross correlation was too low for there to be confidence in the results or, as in the previous step, where the velocity vectors were inconsistent with their neighbours, these vectors were removed. Where vectors had been removed, the resulting gaps in the data set were filled in by interpolation of the values from the surrounding cells.

The resulting vector fields had a spatial extent of approximately 100 mm ($0.56c$) and a resolution of roughly 0.8 mm ($0.005c$) in both the Y and Z directions. Near the edges of the processed vector fields, where the laser illumination and particle seeding were insufficient, the data were discarded. The edge of usable data was determined by examining the RMS deviation from the mean vector in each interrogation cell for a dataset (2000 images) at each measurement plane. Near the edges of the data where the results became questionable, the RMS deviation about the mean vectors increased significantly allowing these areas to be easily identified and discarded.

3.6 Laser induced fluorescence

LIF images were taken in three orthogonal planes, namely XY, XZ, and YZ. Rhodamine 6G dye was injected through the wing-tip and was used to demarcate the wing-tip vortex since the dye remained in and near the wing-tip vortex core for the length of the test section. Images of the XY and XZ planes were recorded simultaneously at a rate of 4 Hz. These images were taken using Imager pro X 4M cameras with Nikon Nikkor 50 mm f/1.8D lenses at two locations, one centred on $X = 1.18$ m ($X = 6.6c$) and the other on $X = 2.28$ m ($X = 12.8c$). Images in the YZ plane were taken using the same arrangement as was used for the SPIV measurements, except that a high-speed camera was used. The camera used in this case was a pco.edge with a resolution of 2560 x 2160 pixels at a frame rate of 100 Hz along with a Nikon Nikkor 50 mm f/1.8D lens and a long pass 540 nm filter. The filter improved the clarity of the images by selectively allowing light at the peak emission wavelength of Rhodamine 6G dye to enter the camera. Images in the YZ plane were captured at $X = 1.73$ m ($X = 9.7c$). Illumination for all dye images was provided by a 1 W continuous beam diode laser (Wicked Lasers, model KPN5323S), which emitted radiation at a peak wavelength of 532 nm. For images in the XY and XZ plane, the beam was passed through a lens to create a cone of light which illuminated the entire vortex over the streamwise length that was in the field of view of cameras. For images in the YZ plane, the beam was passed through a sheet generating lens which illuminated the YZ plane; the thickness of illumination was roughly 2 mm.

3.7 Uncertainty estimates

3.7.1 Equipment positioning

The wing model and the calibration plate were mounted on a cart, which could traverse the length of the test section. The streamwise position of the cart was measured to ± 2 mm and was determined by observing the cart's position relative to a scale affixed to the top of the water tunnel. The location of the turbulence generating grids was also determined to ± 2 mm relative to the water tunnel scale. The laser sheet was aligned at each measurement plane to be at the centre of the desired measurement volume as determined by the location of the calibration plate. In the Z direction, the quarter-chord point of the wing and the centre of the calibration plate were aligned to $\pm$ 1 mm of the centre of the tunnel. The wing-tip and the origin of the calibration plate were located at 397 $\pm$ 1 mm above the tunnel floor.

3.7.2 Stereo particle image velocimetry

The SPIV system used in this study produced a three-component velocity map by calculating a two-component velocity map from each camera and then combining them to derive the third velocity component. Following established guidelines for estimating uncertainty in PIV studies (Specialist Committee on Uncertainty Analysis of 25th ITTC, 2008), the uncertainty in two-component PIV studies can be examined as the uncertainty associated with each of four fundamental parameters:

- the uncertainty of the magnification coefficient $\delta\alpha_m$;
- the uncertainty in the displacement of a particle on the CCD chip $\delta\Delta X_{CCD}$;
- the uncertainty in the time between frames $\delta\Delta t$;
- and the uncertainty associated with the ability of the particles to follow the fluid flow $\delta\mathbf{U_{seed}}$.

In terms of these fundamental parameters, the velocities in the two component vector maps $\mathbf{U_{2C}}$ can be described as:

$$\mathbf{U_{2C}} = \alpha_m \frac{\Delta X_{CCD}}{\Delta t}. \tag{3.1}$$

The uncertainty in the velocities can be calculated as:

$$\frac{\delta\mathbf{U_{2C}}}{\mathbf{U_{2C}}} = \sqrt{\left(\frac{\delta\alpha_m}{\alpha_m}\right)^2 + \left(\frac{\delta\Delta X_{CCD}}{X_{CCD}}\right)^2 + \left(\frac{\delta\Delta t}{\Delta t}\right)^2 + \left(\frac{\delta\mathbf{U_{seed}}}{\mathbf{U_{seed}}}\right)^2}. \tag{3.2}$$

Magnification coefficient

The magnification coefficient α_m was defined as the ratio of the image size in pixels L_r to the physical size on the measurement plane l_r.

$$\alpha_m = \frac{l_r}{L_r} \tag{3.3}$$

The calibration plate and the camera's CCD chip are both built to extremely small tolerances so the uncertainties of l_r and L_r are negligible. Small misalignments between the calibration plate and the plane of the light sheet where particles are actually measured could be up to 3° resulting in an uncertainty in α_m of $(1 - \cos(3°))$ or 0.1 %. Uncertainty due to lens aberration contributes an uncertainty of roughly 0.5 % of the total image length L_r. When added in quadrature, the two contribute a possible bias of 0.5 % in the magnification coefficient.

Particle displacement

Uncertainty in the measurement of particle displacement on the CCD was primarily due to the possibility of particle pair mis-matches. This occurs when an erroneous peak instead of the true peak in the correlation map is used to compute a flow vector. Based on statistical analysis of the error introduced by mis-matches in artificial images this uncertainty was estimated to be roughly 0.2 pixels (Specialist Committee on Uncertainty Analysis of 25th ITTC, 2008). An additional error in the particle displacement is due to a phenomenon known as 'peak locking' which is the result of the process of discretization of particle reflections into pixels and results in an uncertainty of roughly 0.1 pixels. For an average particle displacement between frames of roughly 8 pixels, the precision uncertainty in the particle displacement was approximately 4 %.

Time between frames

The time between frames was controlled by a programmable timing unit (PTU) which synchronized the cameras and the laser pulses. The significant uncertainties in Δt were the uncertainty in the synchronizing pulse of the PTU and in the separation between the laser pulses. Based on the manufacturers' manuals the uncertainty in the signal from the PTU was 5 ns and in the laser pulse itself was 10 ns. Given that Δt was 3500 μs for all measurements, the resulting precision uncertainty in Δt was 3×10^{-4} %.

Particle velocity

Since SPIV measurements detect the velocity of seed particles in the fluid and not the velocity of the fluid itself, it is important to estimate the difference between these two velocities. The hollow glass spheres which were introduced as seed particles as well as the foreign particles present in the tunnel which were not removed by the 5 μm filter are considered here. The foreign particles are assumed to be primarily composed of rust (ferric oxide) from the axial pump.

The terminal rise or sink velocity U_T of the particle is an upper bound of the difference between the seed particle velocity and the flow velocity in the Y (vertical) direction. Approximating all the particles as spherical and assuming Stokes flow for a conservative estimate of the drag force on the particles, Tavoularis (2005) suggests calculating U_T as:

$$U_T = (\rho_P - \rho_W)\,\frac{g d_P^2}{18\mu_W} \tag{3.4}$$

where g is gravitational acceleration, d_P is the particle diameter, μ_W is the dynamic viscosity of the fluid, and ρ_P and ρ_W are the particle and fluid densities, respectively. For the hollow glass spheres, which had a density of 1.10 g/cm^3 and 90 % of which were less than 16 μm in diameter (according to the manufacturer's specifications), U_T was 1.4×10^{-5} m/s. Considering that the density of ferric oxide is 5.24 g/cm^3 and using the 5 μm pore size of the water tunnel filter as the particle diameter, one may estimate that U_T for the foreign particles was 5.8×10^{-5} m/s. The terminal sink velocity was used to approximate the uncertainty in the particle velocity relative to the fluid velocity $\mathbf{U_{seed}}$. The average velocity in the YZ plane was 6×10^{-3} m/s (a conservative value based on the large grid tests where the in plane velocities were slowest). The precision uncertainty due to the particle's relative velocity was estimated to be, at most, 1 %.

It was also of interest to estimate the upper bound of the frequency of changes in fluid motion which could be resolved well by the particle motion. If one considers that the velocity of a particle will eventually match the velocity of the surrounding fluid due to viscous forces, the time lag between a change in the fluid velocity and the change in particle velocity can be characterized by a time constant, τ_P. Tavoularis (2005) gives an expression for this time constant as

$$\tau_P = \frac{\rho_P d_P^2}{18\mu_W}\left(1 + \frac{\rho_W}{2\rho_P}\right). \tag{3.5}$$

The inverse of the time constant is an estimate of the minimum frequency of fluid motion which would be suppressed (as by a 3 dB 1st order low-pass filter) by the particle motion. This frequency was 45 kHz for the hollow glass spheres and 125 kHz for the foreign particles.

Total SPIV uncertainty

Based on these estimates, the overall uncertainty in the velocities of each two-component velocity map was 4 %. This can be separated into a precision limit of 4 % and a bias limit of 0.5 %.

LaVision Inc. (2012) outlined a method for estimating the uncertainty in velocities in a three-component velocity map $\delta\mathbf{U_{3C}}$. The method used the geometry of the optical system along with the uncertainties in the velocities from the two-component maps to estimate $\delta\mathbf{U_{3C}}$. The uncertainty in the in-plane and out-of-plane components are given by

$$\delta U_x = \delta U_{2C}\frac{\sqrt{sin^2\alpha_1 + sin^2\alpha_2}}{|sin^2\left(\alpha_2 - \alpha_1\right)|} \quad , \tag{3.6}$$

$$\delta U_z = \delta U_{2C}\frac{\sqrt{cos^2\alpha_1 + cos^2\alpha_2}}{|sin^2\left(\alpha_2 - \alpha_1\right)|} \quad , \text{ and} \tag{3.7}$$

$$\delta U_y = \frac{\delta U_{2C}}{\sqrt{2}}, \tag{3.8}$$

where α_1 and α_2 are the angles at which the two cameras view the measurement plane; in this case these angles were $+45°$ and $-45°$, respectively. The total precision

Table 3.1: Precision and bias limits in individual measurements of velocity components.

	Precision Limit of U_{2C} [%]	Bias Limit of U_{2C} [%]
δU_x	4	0.5
δU_y	3	0.4
δU_z	4	0.5

and bias limits of individual measurements of the U_x, U_y, and U_z velocity components are presented in Table 3.1 as percentages of the magnitude U_{2C} of the two-component velocity vectors $\mathbf{U_{2C}}$. When a result is the average of more than 10 repeated measurements in a stationary field, the precision limit of the mean is equal to the precision limit of each value divided by $\sqrt{N}$, where N is the number of measurements. The resolution of the vector fields and, therefore, the smallest discernible scale of motion, was $0.005c$.

3.7.3 Derived quantities

Swirling strength SS and Q were calculated for each velocity map as

$$SS = max\left[0, -\left(\frac{\partial U_y}{\partial Z}\frac{\partial U_z}{\partial Y} - \frac{1}{2}\left(\frac{\partial U_y}{\partial Y}\frac{\partial U_z}{\partial Z}\right) + \frac{1}{4}\left(\frac{\partial U_y}{\partial Y}^2 + \frac{\partial U_z}{\partial Z}^2\right)\right)\right] \quad \text{, and} \tag{3.9}$$

$$Q = \frac{1}{2}\left(\|\mathbf{\Omega}\|^2 - \|\mathbf{S}\|^2\right) = \frac{1}{2}\left(\frac{\partial U_z}{\partial Z}^2 + \frac{\partial U_y}{\partial Y}^2\right) - \left(\frac{\partial U_y}{\partial Z}\frac{\partial U_z}{\partial Y}\right), \tag{3.10}$$

where $\mathbf{S}$ and $\mathbf{\Omega}$ are the symmetric and antisymmetric components of the rate of strain tensor, respectively. Both of these parameters depend on velocity derivatives. The LaVision Inc. software calculates velocity derivatives using a central difference scheme. The error associated with a velocity derivative calculated using a central difference scheme in a PIV system can be approximated as $0.7\epsilon_u/X_{VS}$ (Raffel, 2007), where X_{VS} is the spacing between velocity vectors (0.86 mm) and ϵ_u is the precision limit of the velocities. The average magnitude of the velocity derivatives (based on the calculated vector fields) was 1.5 s^{-1}. The uncertainties of the SS and the Q were determined from the propagation of the uncertainties in the velocity derivatives as

$$\begin{aligned}\delta SS = &\left\{ \left(\delta\frac{\partial U_z}{\partial Y}\cdot\frac{\partial U_y}{\partial Z}\right)^2 + \left(\delta\frac{\partial U_y}{\partial Z}\cdot\frac{\partial U_z}{\partial Y}\right)^2 \right.\\ &+\frac{1}{4}\left[\left(\delta\frac{\partial U_z}{\partial Z}\cdot\frac{\partial U_y}{\partial Y}\right)^2 + \left(\delta\frac{\partial U_y}{\partial Y}\cdot\frac{\partial U_z}{\partial Z}\right)^2\right.\\ &\left.\left.+\left(\delta\frac{\partial U_y}{\partial Y}\cdot\frac{\partial U_y}{\partial Y}\right)^2 + \left(\delta\frac{\partial U_z}{\partial Z}\cdot\frac{\partial U_z}{\partial Z}\right)^2\right]\right\}^{1/2}\\ =&0.7\mathrm{s}^{-2} \quad \text{, and}\end{aligned} \tag{3.11}$$

$$\begin{aligned}\delta Q =&2\left[\left(\delta\frac{\partial U_z}{\partial Z}\cdot\frac{\partial U_y}{\partial Y}\right)^2 + \left(\delta\frac{\partial U_y}{\partial Y}\cdot\frac{\partial U_z}{\partial Z}\right)^2\right.\\ &\left.+\left(\delta\frac{\partial U_y}{\partial Y}\cdot\frac{\partial U_y}{\partial Y}\right)^2 + \left(\delta\frac{\partial U_z}{\partial Z}\cdot\frac{\partial U_z}{\partial Z}\right)^2\right]^{1/2}\\ =&2\mathrm{s}^{-2}.\end{aligned} \tag{3.12}$$

3.7.4 Laser induced fluorescence

The de-warping and scaling of the LIF images was accomplished using the same software as that used in the analysis of the SPIV particle images. LIF images taken in the XY and XZ planes were used to statistically investigate the angles which the vortex axis makes with the YZ plane. The process by which this was accomplished is outlined in Section 5.1. The vortex axis location and slope were estimated from these images with an approximate precision uncertainty of ± 5 mm and ± 5°, respectively. LIF images taken in the YZ plane were used to estimate the vortex axis location in a series of high speed images (this procedure has been outlined in Section 5.2). The precision uncertainty associated with that estimation was approximately ± 3 mm for the no-grid cases and ± 5 mm for the small-grid cases.

Chapter 4

Results

4.1 Freestream flow characteristics

Sets of 500 particle images were taken without the wing in the water tunnel at each SPIV measurement plane as well as at the plane of the trailing edge of the wing. This was done for each turbulence condition (*i.e.*, the no-grid, small-grid, and large-grid cases) in order to characterize the freestream flow conditions.

4.1.1 Axial velocity

The uncertainties in the three Cartesian velocity components δU_x, δU_y, and δU_z defined in Equations 3.6 to 3.8 are calculated from the uncertainty $\delta \mathbf{U_{2C}}$ (Equation 3.2) in the velocities from the two component vector maps produced from the particle images from each camera along with the angles at which the cameras view the measurement plane α_1 and α_2. As described in Section 3.5.1, the two PIV cameras were positioned at angles of $\alpha_1 = 45°$ and $\alpha_2 = -45°$ with respect to the streamwise axis. As such, the particle motion perceived by a single camera in the Z direction was not a true representation of the movement of the particles in the Z direction but was a combination of the motion of the particles in the X and Z directions. Defining $U_{2C,z}$ to be the Z component of velocity derived from a single camera, Equation 4.1 and Figure 4.1 show the relationship between the true streamwise and transverse velocities U_x and U_z and $U_{2C,z}$ for the camera at an angle $\alpha_1 = 45°$.

$$U_{2C,z} = U_z cos(\alpha_1) + U_x sin(\alpha_1) \quad (4.1)$$

Measurements of $\langle U_x \rangle$ for cases without the wing are presented in Table 4.1. The RMS variation in $\langle U_x \rangle$ across each measurement frame was up to 0.75 %. The transverse and spanwise velocities in all cases were at least an order of magnitude smaller than the streamwise one, even in the measurements with the wing in place. Given

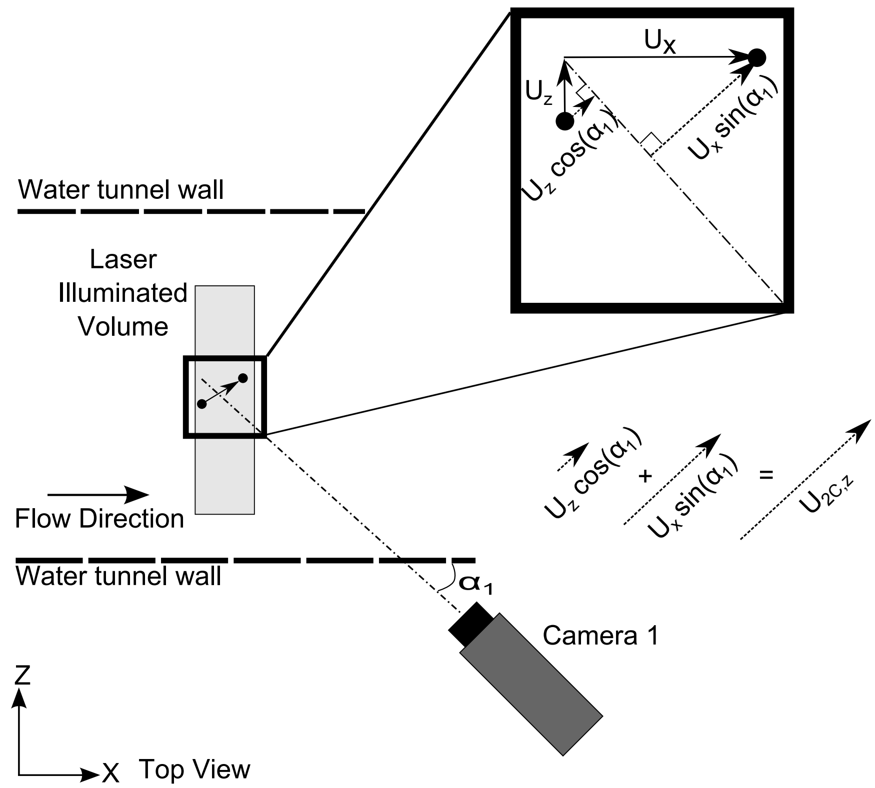

Figure 4.1: Sketch of the relationship between U_z, U_x, and $U_{2C,z}$ (not to scale).

Table 4.1: Mean axial velocities.

	$\langle U_x \rangle$ (m/s)		
	No-grid	Small-grid	Large-grid
$X/c = 0.7$	0.136	0.133	0.133
$X/c = 3.6$	0.135	0.133	0.134
$X/c = 6.6$	0.137	0.135	0.135
$X/c = 12.8$	0.139	0.138	0.138

$\delta\langle U_x \rangle = 0.001 m/s$

Equation 4.1, the velocities in the two-component vector maps $\mathbf{U_{2C}}$ were likewise dominated by the axial velocity. As with $\langle U_x \rangle$, $\mathbf{U_{2C}}$ did not show strong spatial variations. The ensemble averaged values of $\mathbf{U_{2C}}$ were always less than 0.12 m/s, and their averages across the measurement planes never exceeded 0.10 m/s. The upper limit 0.12 m/s was used in Equations 3.6 to 3.8 to obtain a conservative estimate of the uncertainty of individual velocity measurements (summarized in Table 4.2).

The Reynolds number based on these mean axial velocities and the chord length was $Re_c \approx 2.4 \times 10^4$ in all cases.

4.1.2 Uncertainty in measured velocities

The velocities presented in Table 4.1 are ensemble averages of 500 vector maps so the precision limit of these values was significantly reduced resulting in total uncertainties of 6×10^{-4} m/s in δU_x and δU_z and 5×10^{-4} m/s in δU_y (Table 4.2). The RMS variation in $\langle U_x \rangle$ across a given measurement frame (up to 0.75 % of $\langle U_x \rangle$ or 0.001 m/s) was significant relative to the total measurement uncertainty and was summed in quadrature with the precision uncertainty of the measured data to determine the precision limit of the values presented in Table 4.1. The resulting total uncertainty in the values of $\langle U_x \rangle$ was 0.001 m/s. The values of $\langle U_x \rangle$ for the no-wing cases are used as an estimate of the mean freestream velocity U_∞ for the measurements taken with the wing.

Table 4.2: Uncertainties in mean measurements of U_x, U_y, and U_z.

Uncertainties in U_x, U_y, and U_z ($\times 10^{-3}\ m/s$)						
	$\delta U_x,\ \delta U_z$			δU_y		
	Precision	Bias	Total	Precision	Bias	Total
Individual measurement	5	0.6	5	4	0.5	4
Mean over 500 frames	0.2	0.6	0.6	0.2	0.5	0.5
Mean over 2000 frames	0.04	0.6	0.6	0.04	0.5	0.5

Table 4.3: Magnitude of mean velocities in the YZ plane.

$\langle \lvert U_{yz} \rvert \rangle (m/s)$			
	No-grid	Small-grid	Large-grid
$X/c = 0.7$	0.003	0.003	0.003
$X/c = 3.6$	0.003	0.002	0.002
$X/c = 6.6$	0.003	0.002	0.002
$X/c = 12.8$	0.003	0.002	0.002

$\delta\langle \lvert U_{yz} \rvert \rangle = 0.001 m/s$

4.1.3 Transverse and spanwise velocities

The mean magnitudes of the velocity $|U_{yz}|$ parallel to the YZ measurement plane for the measurements taken without the wing are presented in Table 4.3 as average values over the measurement frame. The small observed values of the cross-stream velocities are attributed to residual large scale structures, which were not completely broken down in the settling tank (Vanderwel, 2011). The uncertainty in these values, determined in the same manner as for $\langle U_x \rangle$, was 0.001 m/s.

4.1.4 Freestream turbulence

The mean turbulence intensity is defined as the ratio of the standard deviation u_i' of the corresponding velocity fluctuations averaged over the measurement plane and the mean axial velocity $\langle U_x \rangle$. The mean turbulence intensities in the X, Y, and Z directions at the measurement plane located at the trailing edge of the wing are summarized in Table 4.4.

Table 4.4: Mean turbulence intensities at the $X/c = 0.7$.

$u_i'/\langle U_x \rangle$			
	No-grid	Small-grid	Large-grid
Streamwise intensity (X)	2.9 %	3.8 %	5.9 %
Transverse intensity (Z)	2.3 %	3.5 %	5.3 %
Spanwise intensity (Y)	2.4 %	3.5 %	5.3 %

$\delta u_i'/\langle U_x \rangle = 0.1$ %

Turbulent stresses

A conventional approach to describing turbulent stresses downstream of turbulence generating grids represents their evolution using power laws (Batchelor & Townsend, 1948)

$$\frac{\langle {u_i}^2 \rangle}{{U_x}^2} = a \left(\frac{X - X_o}{M} \right)^{-n}, \tag{4.2}$$

where a and n are constants and streamwise distance is not measured from the position of the turbulence generating grids ($X/c = -3.7$) but from an effective origin X_o. X_o is selected such that the measured data is linearised (on logarithmic axes) over the maximum possible streamwise distance. The turbulent kinetic energy per unit mass, defined as

$$k = \frac{1}{2} \left(\langle {u_x}^2 \rangle + \langle {u_y}^2 \rangle + \langle {u_z}^2 \rangle \right), \tag{4.3}$$

may be described using the same approach as is used for the turbulent stresses. The streamwise evolution of k can also be described by a power law

$$\frac{k}{{U_x}^2} = a \left(\frac{X - X_o}{M} \right)^{-n}. \tag{4.4}$$

The power law approach assumes that the flow is dominated by the turbulent structures generated by the grid and that the flow incident to the grids does not contain turbulent fluctuations which are significant with respect to the fluctuations generated by the grid.

In the experiments described in this thesis, the flow conditions upstream of the turbulence generating grid were not quiescent as evidenced by the presence of turbulence intensities in the no-grid case that were on the same order of magnitude as the cases with the small- and large-grid turbulence generators (Table 4.4). It was previously demonstrated that large-scale turbulent structures are present in the water tunnel that may be too large to be broken down by the turbulence generating grids (Vanderwel, 2011). These structures could contribute to the observed velocity fluctuations in the no-grid cases. Additionally low frequency surface waves, which are commonly encountered in water tunnel facilities containing a free surface, may be present and would appear as velocity fluctuations that do not degrade over the length of the tunnel (Tavoularis, 2005). A previous study on the water tunnel showed evidence of surface waves which propagated at a frequency of 0.1 Hz (Dunn, 2004). Waves of this kind represent a bulk movement of the fluid in the water tunnel and not local turbulent fluctuations. As such, they would not constitute turbulent fluctuations of the type that would interact with the wing-tip vortex but rather a low velocity periodic movement of the water in the water tunnel.

Given these additional sources of velocity fluctuations, the behaviour of turbulent stresses downstream of the grids is not conventional. Near the grids, however, where the flow is most strongly affected by the grid generated turbulence, the evolution of the turbulent stresses and kinetic energy is consistent with expectations for conventional grid generated turbulence. Data from the two measurement planes closest to the turbulence generating grid $X/c = 0.7$ and 3.6 were fit to Equations 4.2 and 4.4. Because of the limited number of data points near the turbulence generating grids, the value of X_o was not selected by attempting to linearise the measured data but a typical value from the literature $X_o = 3M$ was used (Bailey & Tavoularis, 2008). From measurements of $\langle u_x u_x \rangle$, $\langle u_y u_y \rangle$, and $\langle u_z u_z \rangle$ in both the small- and large-grid cases, a mean value of $n = -1.2$ was found which is consistent with the work of Comte-Bellot and Corrsin (1966). Using this value of n, straight lines were fit to the measured turbulent stresses in Figures 4.2 and 4.3. As expected, the streamwise stress was slightly higher than the other stress components for both turbulence cases.

Using the same value of n yielded a good fit for the measured turbulent kinetic energies in Figure 4.4. The turbulent stresses and kinetic energies at measurement locations far downstream of the turbulence generating grids $X/c = 6.6$ and 12.8 (*i.e.*, $X/M - 3 = 71$ and 116 for the small-grid case and 34 and 56 for the large-grid case) were much higher than the power law decay predicts. This is in agreement with the

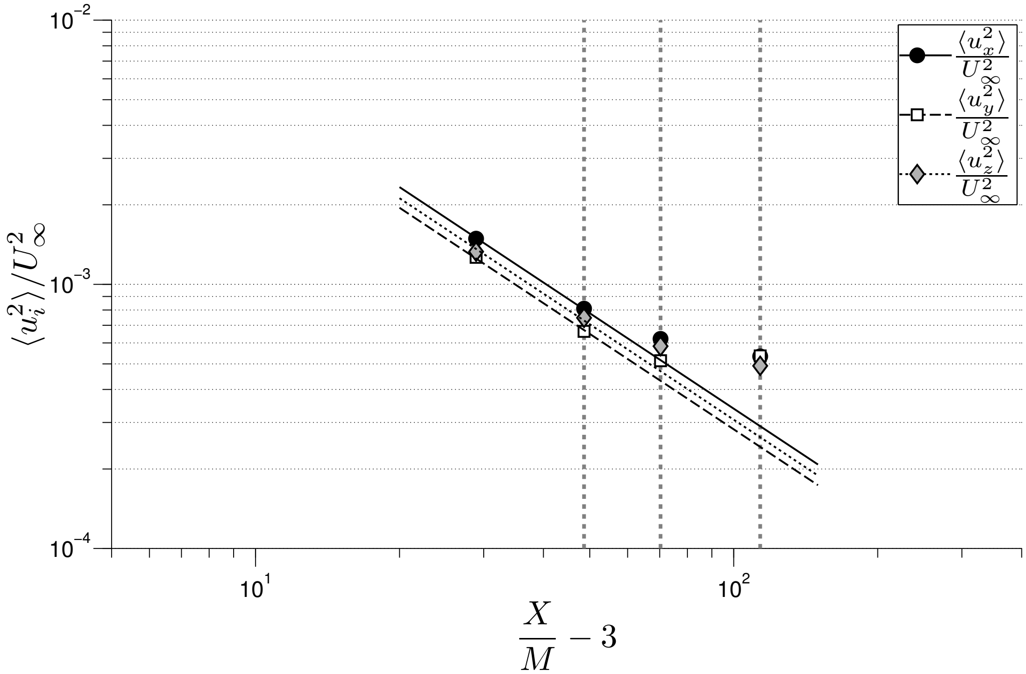

Figure 4.2: Evolution of turbulent stresses downstream of the turbulence generating grid for the small-grid case (vertical lines denote vortex measurement locations).

observation that the flow is relatively noisy even in the no-grid case. Background velocity fluctuations from upstream of the turbulence generating grids seems to sustain the turbulent kinetic energy at higher levels downstream of the grid than would be predicted based on the standard power law model.

Flow anisotropy

The anisotropy tensor is defined as

$$a_{ij} = \frac{\langle u_i u_j \rangle}{2k} - \frac{1}{3}\delta_{ij}, \tag{4.5}$$

where δ_{ij} is the Kronecker delta, which is equal to 1 if $i = j$ and 0 if $i \neq j$ (Pope, 2000). Figures 4.5 and 4.6 show a_{ij} plotted against streamwise location for all turbulence conditions. In isotropic turbulence all components of a_{ij} would be zero. In 4.5 the components of a_{ii} are fairly evenly distributed around $a_{ii} = 0$ as expected since $\sum a_{ii} = 0$. Individual values in Figure 4.6 show some deviation from 0 at all streamwise locations indicating some correlation between velocity components. This

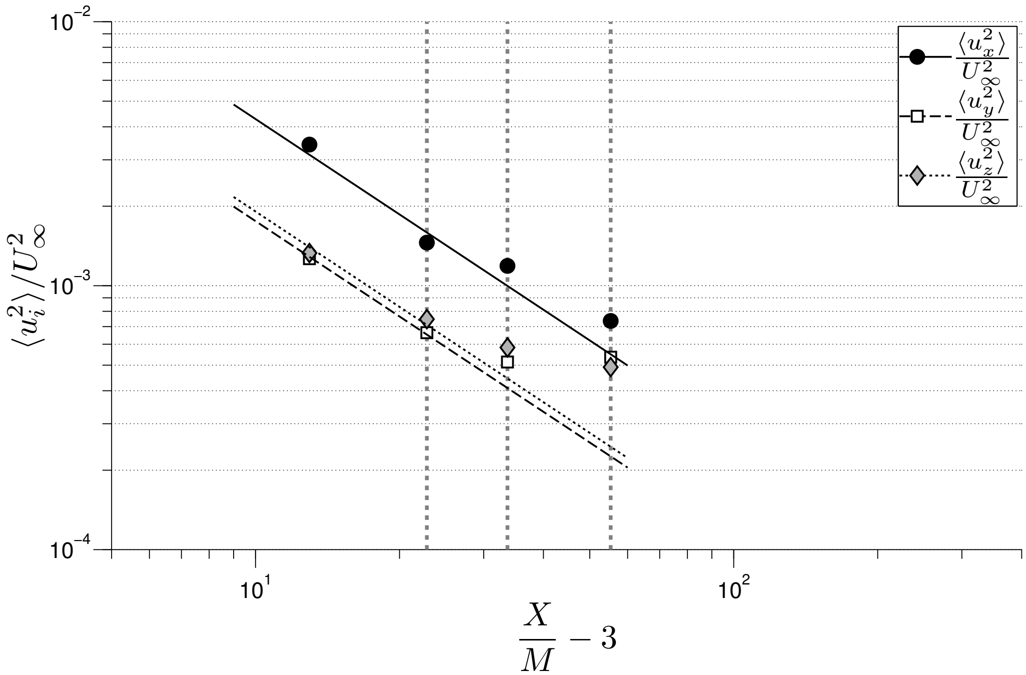

Figure 4.3: Evolution of turbulent stresses downstream of the turbulence generating grid for the large-grid case (vertical lines denote vortex measurement locations).

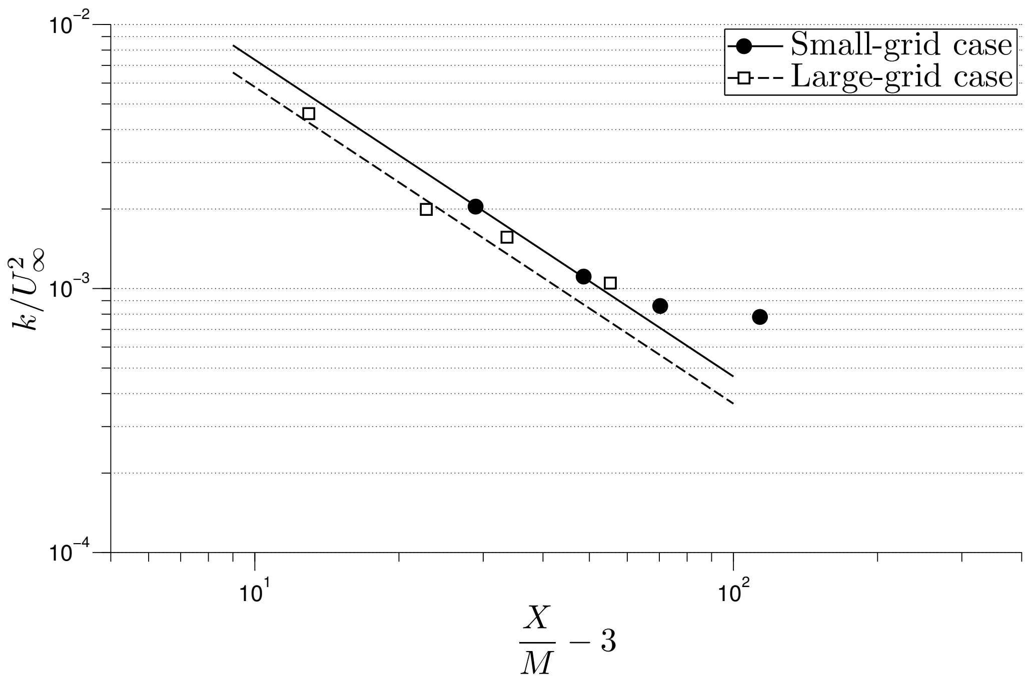

Figure 4.4: Evolution of turbulent kinetic energy downstream of the turbulence generating grid for the small- and large-grid cases.

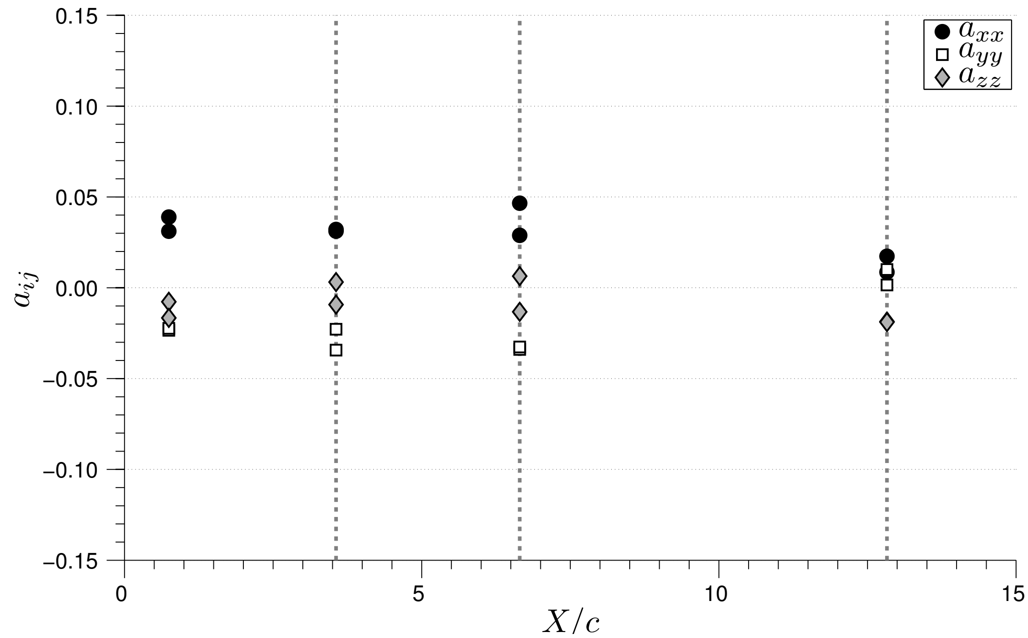

Figure 4.5: Anisotropy tensor components a_{ij} downstream of the wing for $i = j$.

could be due to the presence of residual large-scale structures from upstream of the test section.

Length scales

To identify the most energetic scales of turbulent motion, integral length scales $L_{\alpha\alpha,k}$ were calculated for each turbulence condition. Calculation of the $L_{\alpha\alpha,k}$ requires two-point velocity autocorrelations

$$R_{\alpha\alpha,k}\left(r_k\right) = \frac{\langle u_\alpha(0)u_\alpha(r_k)\rangle}{u_\alpha(0)u_\alpha(0)}, \tag{4.6}$$

where α is the direction of the velocity vector (X, Y, or Z) and r_k is the separation between velocity vectors in the direction k. The velocity autocorrelations were calculated at each measurement plane for each freestream turbulence condition. These values were integrated over r_k to determine $L_{\alpha\alpha,k}$

$$L_{\alpha\alpha,k} = \int_0^\infty R_{\alpha\alpha,k}\left(r_k\right) dr_k. \tag{4.7}$$

$L_{\alpha\alpha,k}$ is the longitudinal scale in the direction α if $\alpha = k$ and the transverse scale if $\alpha \neq k$. In this study, autocorrelations were integrated from $r_k = 0$ to their first

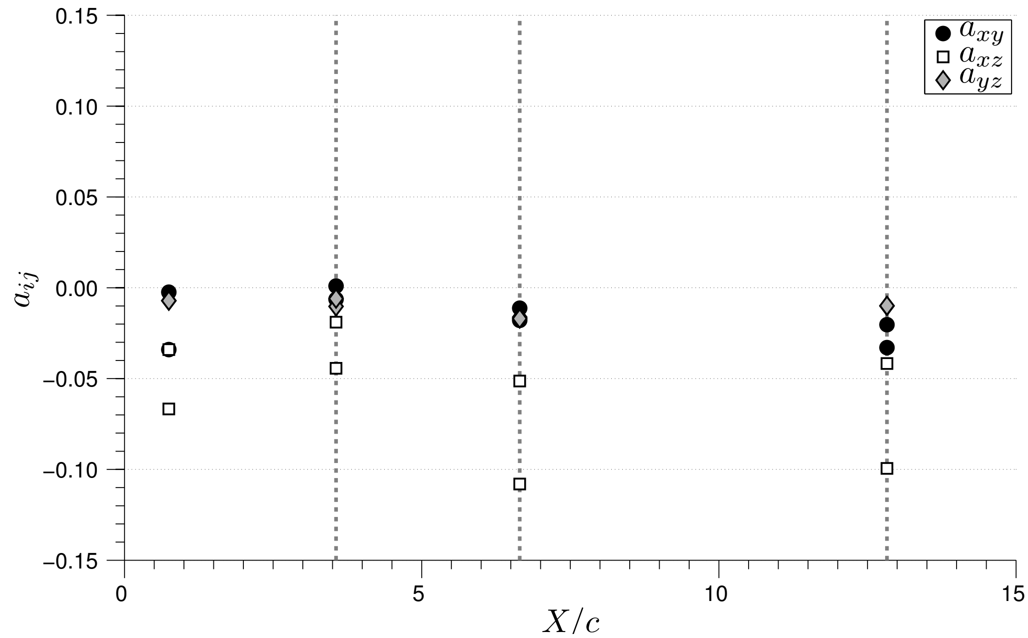

Figure 4.6: Anisotropy tensor components a_{ij} downstream of the wing for $i \neq j$.

zero crossing to obtain the integral length scales as suggested by O'Neill, Nicolaides, Honnery, and Soria (2004). Because all measurement planes were parallel to the YZ plane, the autocorrelations were calculated for r_k in the Y and Z directions but not in the streamwise direction X. Sample autocorrelations taken from the small-grid case at the $X/c = 0.7$ position are shown in Figure 4.7. A 5×5 cell smoothing filter was applied to the velocity data before the autocorrelations were calculated to avoid an artificially steep slope in the autocorrelation curves for values of r_k close to zero. The streamwise evolutions of the integral length scales are shown in Figure 4.8, where the transverse integral length scales for velocities in the Y direction $L_{yy,z}$ and in the Z direction $L_{zz,y}$ were averaged and presented as $L_{trans(y,z)}$ and the longitudinal integral length scales for velocities in the Y direction $L_{yy,y}$ and in the Z direction $L_{zz,z}$ were averaged and presented as $L_{long(y,z)}$. The transverse integral length scales for velocities in the X direction $L_{xx,y}$ and $L_{xx,z}$ were also averaged and are presented together as $L_{trans(x)}$. Straight lines in Figure 4.8 were fit to the data by least squares regression and are of the form

$$\frac{L_{\alpha\alpha,k}}{c} = a_1 \left(\frac{X}{c}\right) + a_2, \tag{4.8}$$

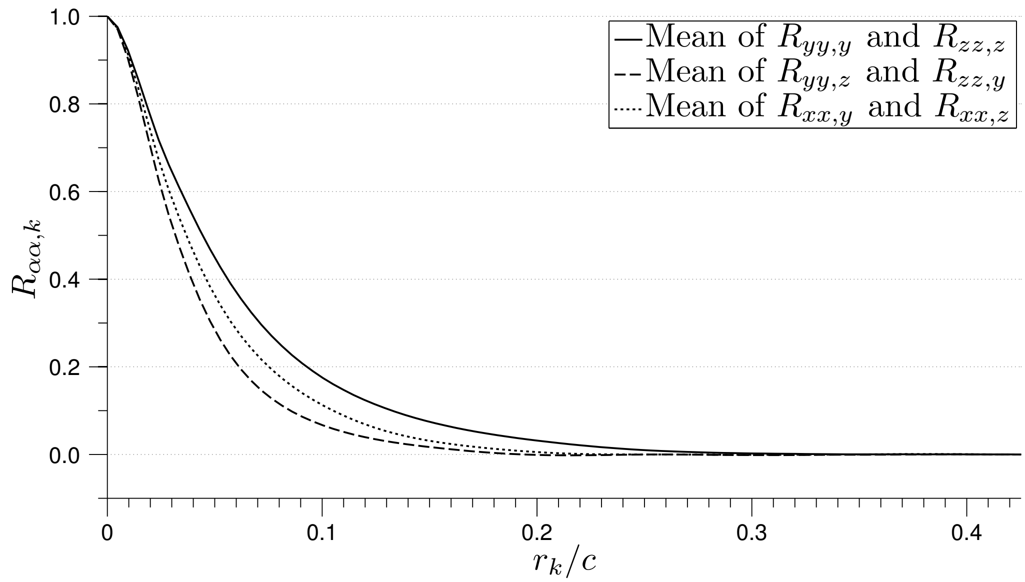

Figure 4.7: Two-point velocity autocorrelation for the small-grid case at $X/c = 0.7$.

where a_1 and a_2 are the regression coefficients. The coefficient a_1 represents the mean increase in $L_{\alpha\alpha,k}/c$ with respect to X/c and a value $a_1 = 2.5 \times 10^{-3}$ was found to fit the data well in all cases.

4.2 Velocity maps

For each measurement plane and each turbulence condition, 2000 sets of images were recorded. Ensemble averages of the corresponding velocities at each interrogation cell are shown in Figures 4.9, 4.10, and 4.11. It is noted that the extents of the data frame at each streamwise location were slightly different; consequently, the scales of the velocity vector arrows are also different in the velocity maps at different streamwise locations. The uncertainty in these values is given in Table 4.2. Data are presented using the fixed coordinate system defined by the Y and Z axes (Figure 3.5) and are not centred on the vortex axis location which varied from one image to the next. Velocity characteristics based on ensemble averages where the vortex axis has been aligned in each vector map are presented in Chapter 5.

At $X/c = 3.6$ (Figure 4.9) a deficit of axial velocity U_x in the wake of the wing is clearly seen in the top left of the data frames. This wake deficit rolls up into a

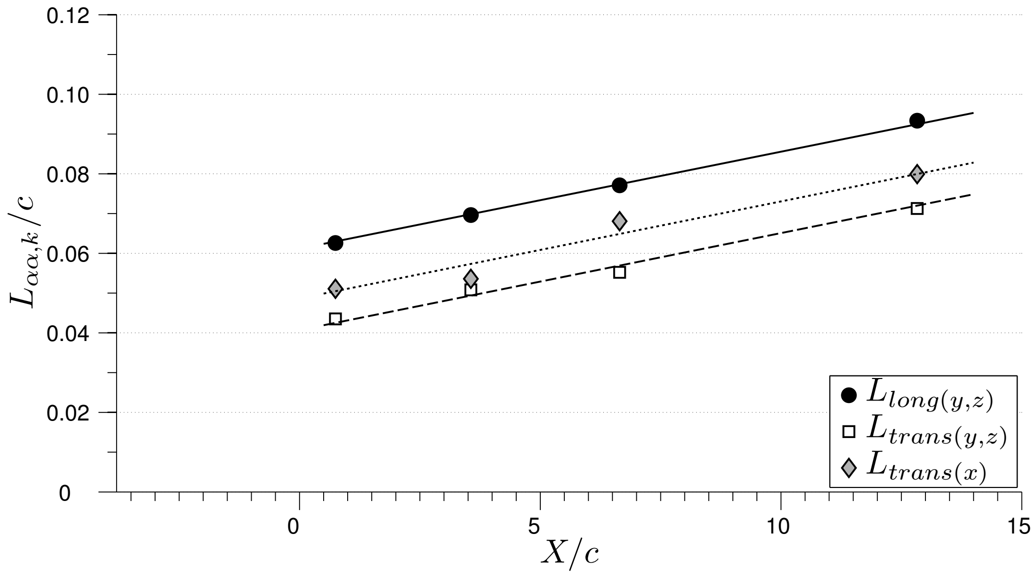

(a)

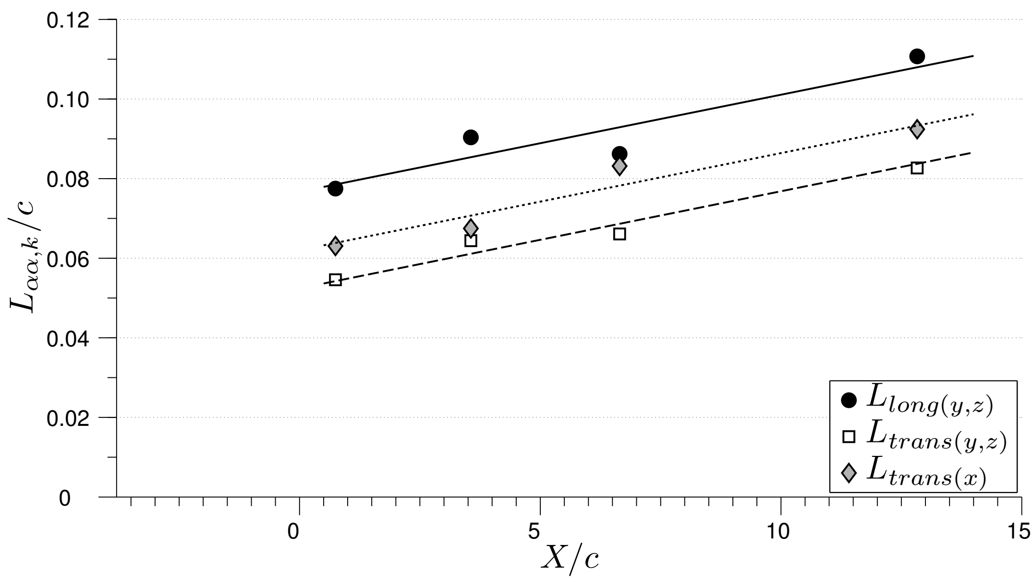

(b)

Figure 4.8: Integral length scales at all measurement planes for the small-grid cases (a) and the large-grid cases (b).

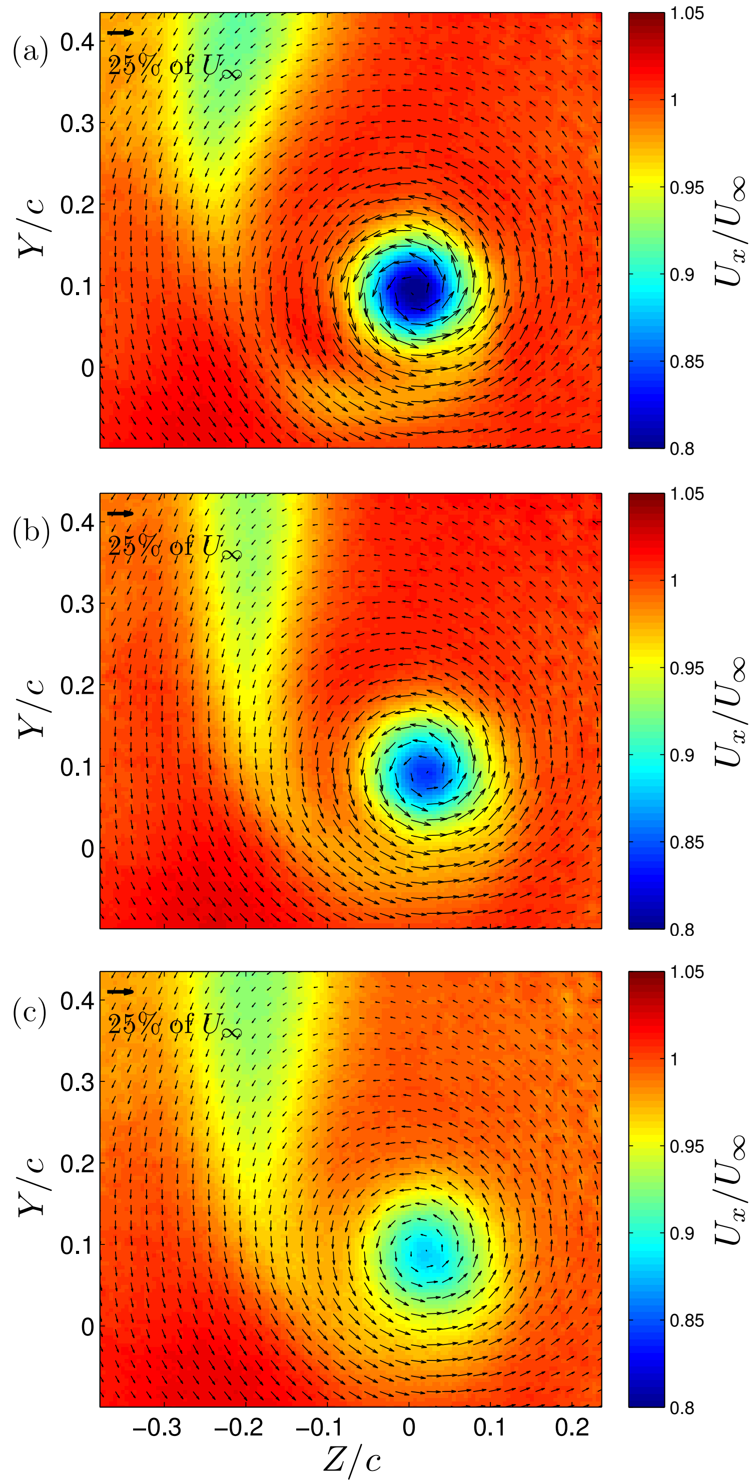

Figure 4.9: Ensemble averaged velocity fields taken from 2000 measurements at $X/c = 3.6$ for (a) the no-grid case, (b) the small-grid case, and (c) the large-grid case.

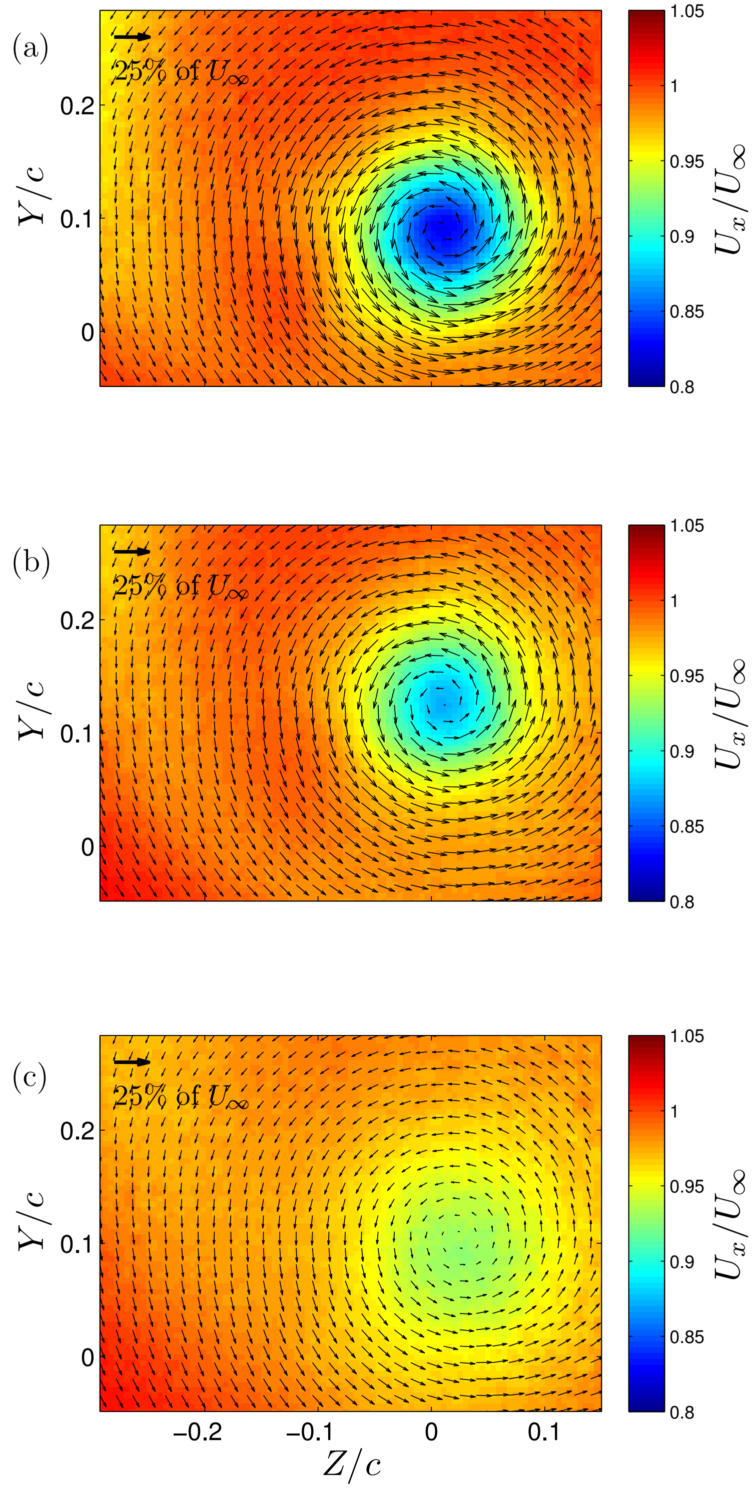

Figure 4.10: Ensemble averaged velocity fields taken from 2000 measurements at $X/c = 6.6$ for (a) the no-grid case, (b) the small-grid case, and (c) the large-grid case.

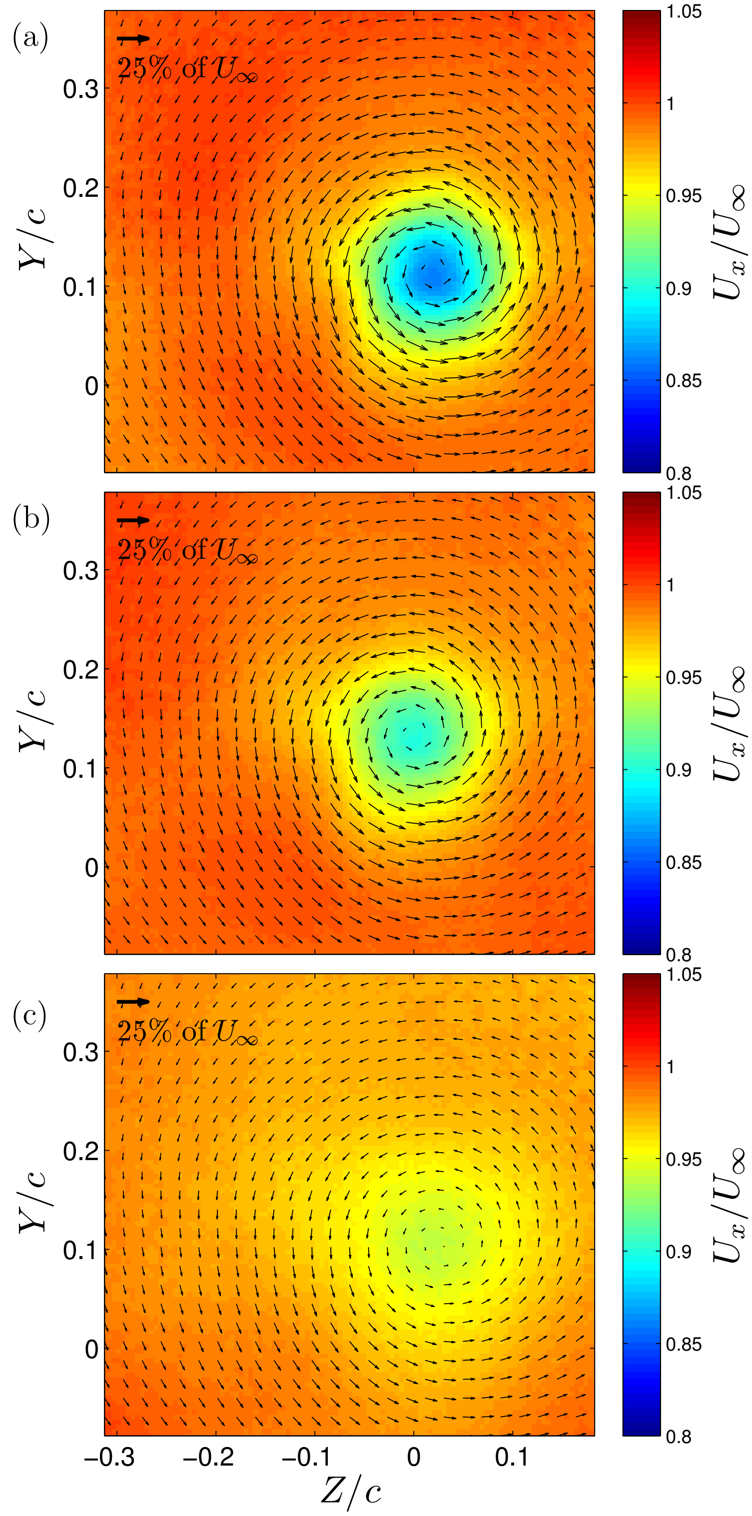

Figure 4.11: Ensemble averaged velocity fields taken from 2000 measurements at $X/c = 12.8$ for (a) the no-grid case, (b) the small-grid case, and (c) the large-grid case.

circular region near the middle of the data frame which shows a more intense axial velocity deficit. The cross-plane velocities U_y and U_z indicate that the flow is rotating around the location of this high axial velocity deficit indicating that it is the mean location of the vortex axis. Comparing the three turbulence cases, the magnitude of the velocity deficit near the vortex axis is most intense in the no-grid case and least intense in the large-grid case. The same trend is true for the magnitudes of the cross-plane velocities near the vortex axis.

Moving downstream to $X/c = 6.6$ (Figure 4.10), the magnitude of the velocity deficit both from the wake of the wing and near the vortex axis decreases and continues to decrease moving to $X/c = 12.8$ (Figure 4.11). The area affected by the velocity deficit near the vortex axis grows moving downstream from $X/c = 3.6$ to 6.6 and on to 12.8. The axial velocity across the entire measurement area decreases with increasing distance downstream of the wing. There is also a trend of decreasing cross-plane velocity magnitudes with increasing distance downstream of the wing. This trend is most pronounced in the large-grid cases. As observed in the three turbulence cases at $X/c = 3.6$, the magnitudes of both the velocity deficit and cross-plane velocities near the vortex axis are greatest in the no-grid cases and least in the large-grid cases in all measurement planes.

4.3 Dye images

Images of the fluorescence of dye that was injected in and around the vortex core were first taken simultaneously in the XY and XZ planes. These images were used to visualize the wandering of the vortex axis. 200 images were taken at two measurement locations ($X/c = 6.6$ and 12.8) for each of the three freestream conditions. Figures 4.12 and 4.13 show typical images in the XY and XZ planes. Processing of these images allowing 3D visualization of the vortex axis and quantitative study of the angles of inclination of the vortex axis with respect to the streamwise axis are presented in Chapter 5.

Dye images were also taken on the transverse (YZ) plane. These were recorded at a rate of 100 Hz, which was sufficiently fast for the motion of the vortex to be followed in time. 1000 images were recorded at a streamwise location of $X/c = 9.7$

for all turbulence conditions. Samples images are shown in Figures 4.14. Further analysis of these images is presented in Chapter 5.

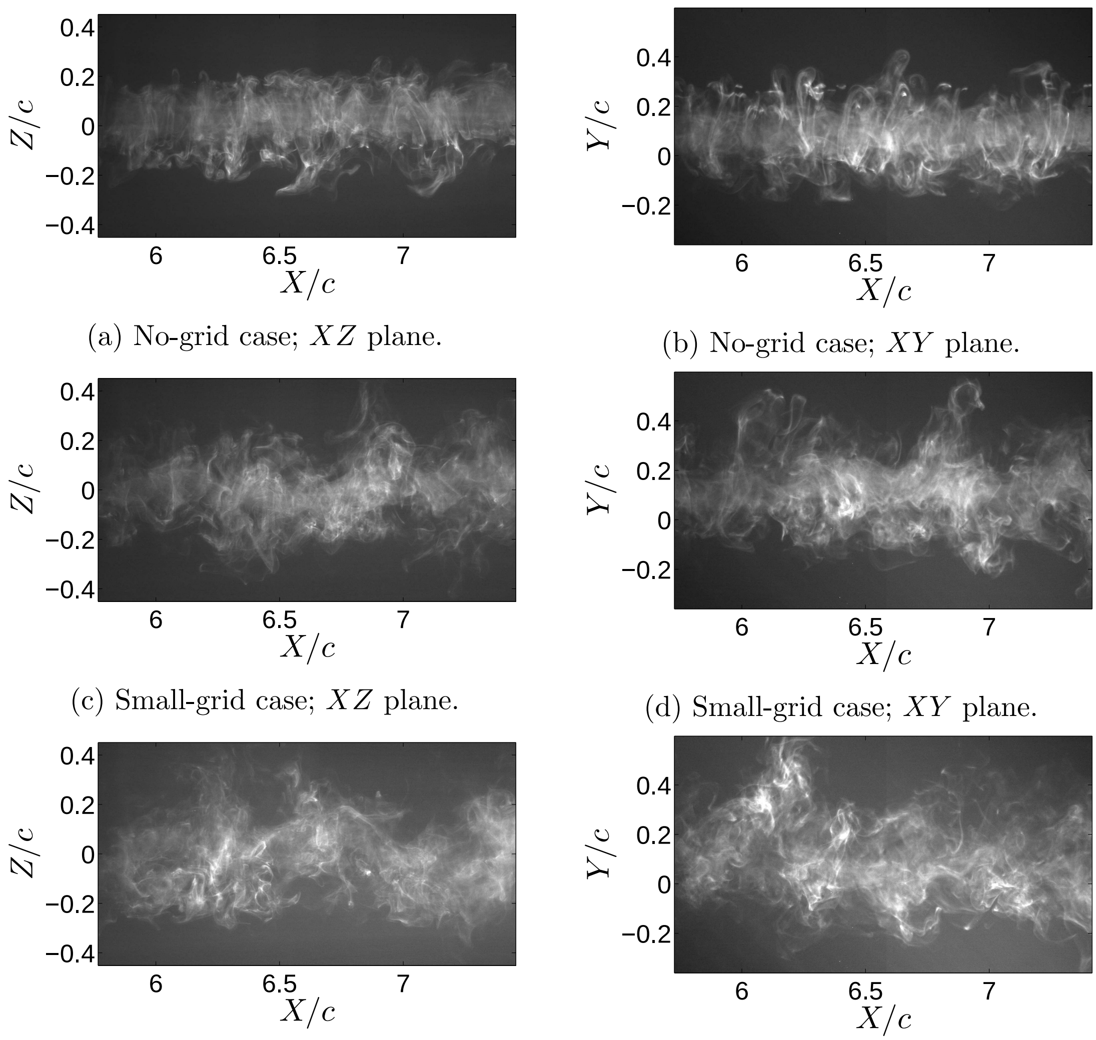

(a) No-grid case; XZ plane.

(b) No-grid case; XY plane.

(c) Small-grid case; XZ plane.

(d) Small-grid case; XY plane.

(e) Large-grid case; XZ plane.

(f) Large-grid case; XY plane.

Figure 4.12: Images of fluorescent dye in the XY and XZ plane near $X/c = 6.6$.

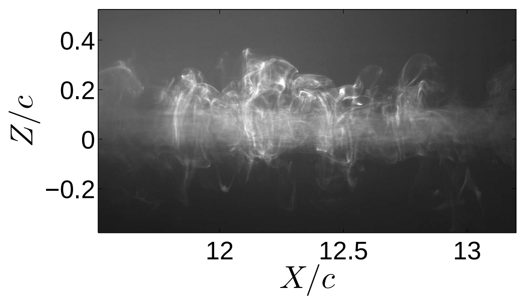

(a) No-grid case; XZ plane.

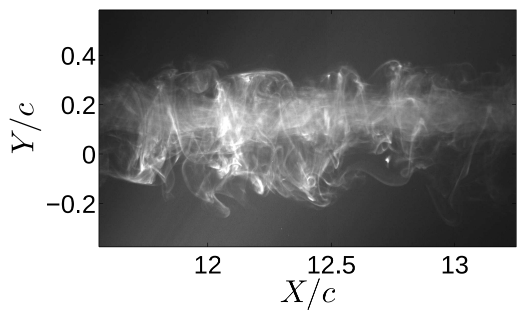

(b) No-grid case; XY plane.

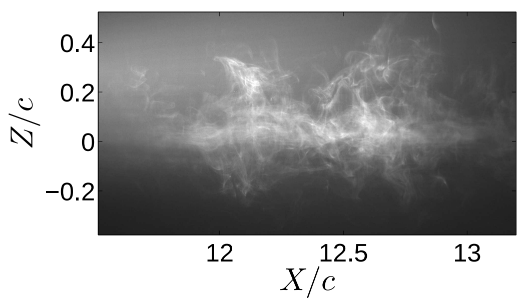

(c) Small-grid case; XZ plane.

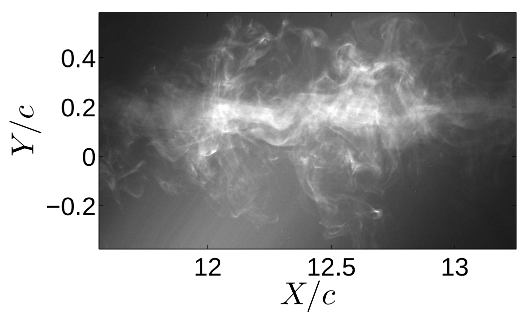

(d) Small-grid case; XY plane.

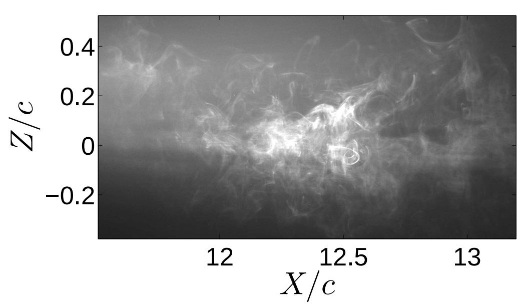

(e) Large-grid case; XZ plane.

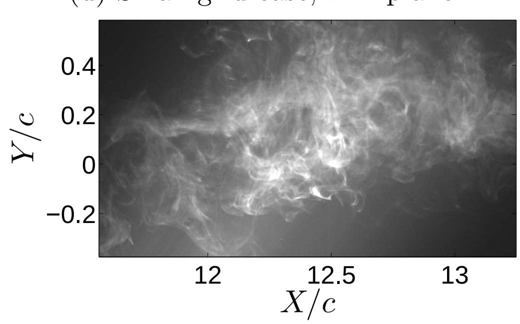

(f) Large-grid case; XY plane.

Figure 4.13: Images of fluorescent dye in the XY and XZ plane near $X/c = 12.8$.

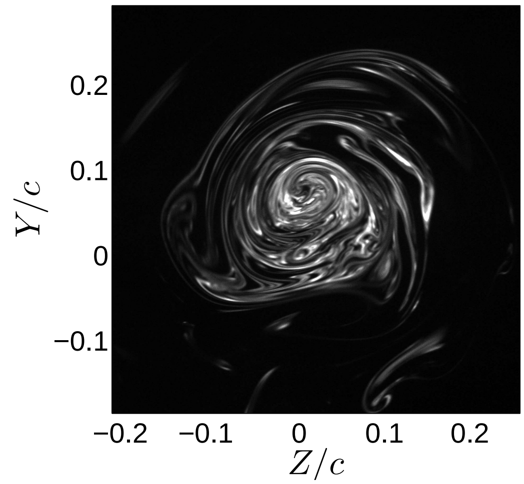

(a) No-grid case; YZ plane.

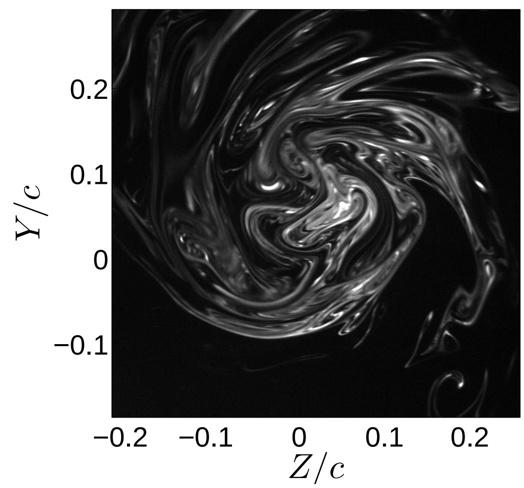

(b) Small-grid case; YZ plane.

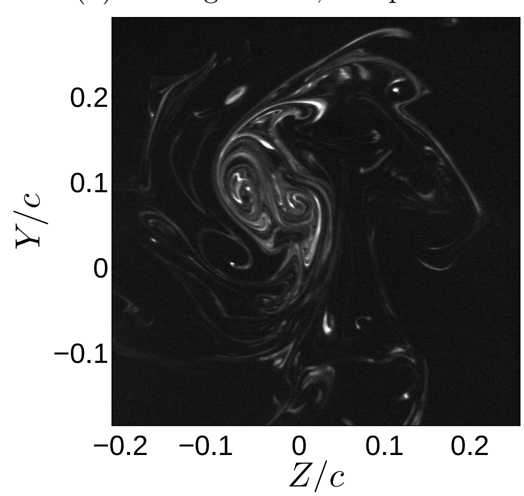

(c) Large-grid case; YZ plane.

Figure 4.14: Images of fluorescent dye in the YZ plane at $X/c = 9.7$.

Chapter 5

Analysis and discussion of the results

This chapter presents the analysis of both SPIV measurements and LIF images. SPIV measurements were used to quantify the wandering of the vortex axis and to investigate radial profiles of azimuthal and axial velocity. The evaluation of various vortex axis finding techniques for planar velocity data constitutes a significant portion of this chapter. Analysis of LIF images in the YZ plane served as an alternative method for measuring vortex axis wandering characteristics; this approach could potentially resolve the movement of the vortex axis with a higher temporal resolution than that of the PIV method. LIF images in the XY and XZ planes were used to visualize the instantaneous vortex axis in three dimensions. These images were also used as a third means by which to investigate the vortex axis wandering as well as to identify the angles of incidence of the vortex axis to the YZ plane Θ.

5.1 Waveform shape and inclination of the vortex axis

5.1.1 Vortex axis identification in XY and XZ plane dye images

The motivating hypothesis for recording images of fluorescent dye in the XY and XZ planes was that these images could identify the spanwise Y_{ax} and transverse Z_{ax} coordinates of the vortex axis at specific streamwise locations. Initially, an attempt was made to identify the axis location by measuring the location of the centre of mass of the vortex in the Y and Z directions using pixel intensity as the mass parameter at each streamwise location. This approach was unsuccessful because the dye was not distributed consistently about the vortex axis in different streamwise measurement planes. Additionally, because the laser light source was positioned below the vortex, the dye at the bottom of the vortex was illuminated more brightly than the dye at the top of the vortex. These problems made this automated method too inaccurate

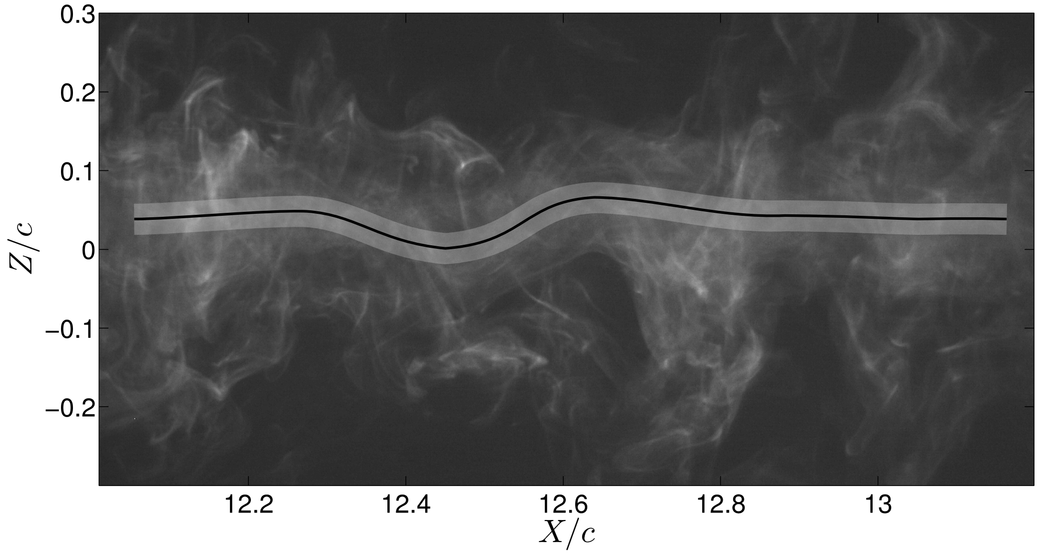

Figure 5.1: Sample of vortex axis identification in an LIF image in the XZ plane; black line marks the vortex axis, surrounding highlighted region marks uncertainty bounds in vortex axis location.

to yield useful results. Instead, a manual approach was used as it was recognized that visual inspection of the images permitted one to distinguish dye in the core of the vortex from dye present in peripheral structures. The vortex axis was assumed to be located at the centre of the vortex core as there was no reason to suspect any significant non-axisymmetry of the core. The uncertainty in identifying the vortex axis by this method was estimated to be $0.03c$ (see Figure 5.1). This technique was successful for all images except those taken near $X/c = 12.8$ in the large-grid case. In the latter images the vortex axis was not distinct enough to be confidently identified by this technique so results from these images are not included in subsequent analyses.

5.1.2 Reconstruction of vortex axis

The 200 images captured in both XY and XZ planes near $X/c = 6.6$ and 12.8 for each turbulence condition were de-warped and scaled to real world dimensions using a calibration plate with known dimensions using the manufacturer's software (FlowMaster software, LaVision Inc.). After the images had been corrected, the vortex axis was traced by hand in each frame excluding regions near the edges of the frame where lighting was insufficient for core identification. This resulted in a

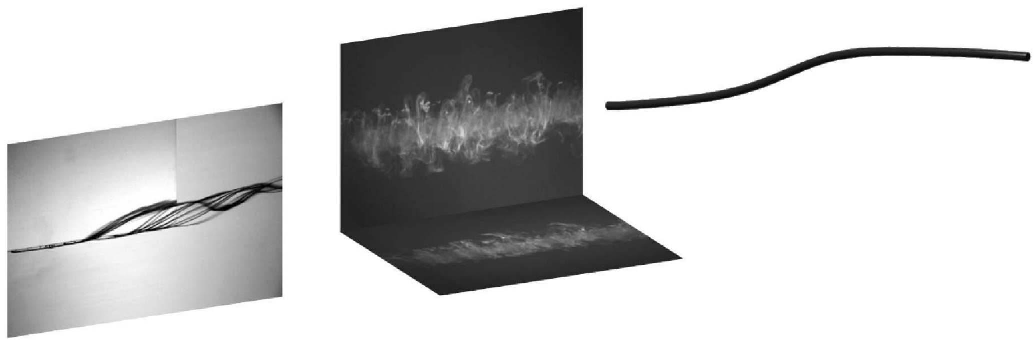

Figure 5.2: Outline of the XY and XZ plane LIF measurement and analysis process.

series of (X,Y) or (X,Z) coordinates for each frame, covering approximately $0.75c$ in the streamwise direction. Using MATLAB, 9^{th} order polynomials were fitted to each series of coordinates in each image to represent Y_{ax} and Z_{ax} as functions of X, namely as

$$p_1 = \sum_{n=0}^{9} a_n X^n \tag{5.1}$$

and

$$p_2 = \sum_{n=0}^{9} b_n X^n, \tag{5.2}$$

where a_n and b_n are fitted coefficients.

Because the XY and XZ images were taken simultaneously and the streamwise location X was recorded in the frames, the coordinates of the vortex axis could be determined at any streamwise location in the data frame by evaluating p_1 and p_2 at that location. The vortex axis was reconstructed in three dimensions by evaluating p_1 and p_2 over the streamwise extent of the frame. An example is shown in Figure 5.2.

5.1.3 Waveform of the wandering vortex axis

This section is concerned with the waveform shape of the vortex axis, whether it resembles a regular shape, and the degree by which it is affected by freestream turbulence. These issues are of interest in light of the assertion of Bailey et al. (2011) that there may be a regular helical component of vortex wandering, which is unaffected by freestream turbulence. It was observed that instantaneous vortex axis reconstructions produced waveforms which were nearly planar, and lay on planes that included the streamwise axis and varied in orientation from one frame to the next. In this plane, the vortex axis often had a quasi-sinusoidal shape with a wavelength λ. The reconstructed vortex axis was inspected from different points of view until the plane on which the waveform pattern appeared to be most prominent, if such existed, was found and then λ was estimated from that view. The streamwise extent of the dye images over which the axis was reconstructed was $0.75c$; this length limited the maximum discernible λ. In addition, it was not always possible to discriminate between small-scale perturbations of the vortex axis, which may be presumed to be caused by freestream turbulent eddies, and large-scale distortions, which may be attributed to wandering motions. In view of these limitations, as well as the considerable uncertainty of this method of identifying the vortex axis, the measurements of λ that are presented here should be taken as cursory estimates.

As mentioned previously, the reconstructed vortex axis shapes were inspected from different points of view and, for frames in which the visible length of the axis appeared to show at least one-quarter wave, the number of visible wavelengths was recorded to the nearest quarter wave. Instances with one-quarter, one-half, three-quarter, one, and one-and-a-quarter waves were encountered, as shown in representative examples in Figures 5.3 and 5.4; it is noted, however, that in many frames it was not possible to detect the presence of such waves.

The result of this rough wavelength estimation procedure was that all identifiable undulations of the vortex axis were deemed to have one among the following five wavelengths: $3c$, $1.5c$, c, $0.75c$, and $0.5c$. Table 5.1 lists the percentage of vortex axis reconstructions in which the observed wavelength was assigned each of these five values, along with the average wavelength $\overline{\lambda}/c$ for the three freestream turbulence conditions. In all cases, irrespectively of turbulence conditions and distance downstream of the wing, the average detected wavelength was slightly lower than c and comparable to the length of the images that were considered. Although it is theoretically possible that a consideration of longer images would have resulted in a longer average wavelength, the statistical distribution of the present results does not support

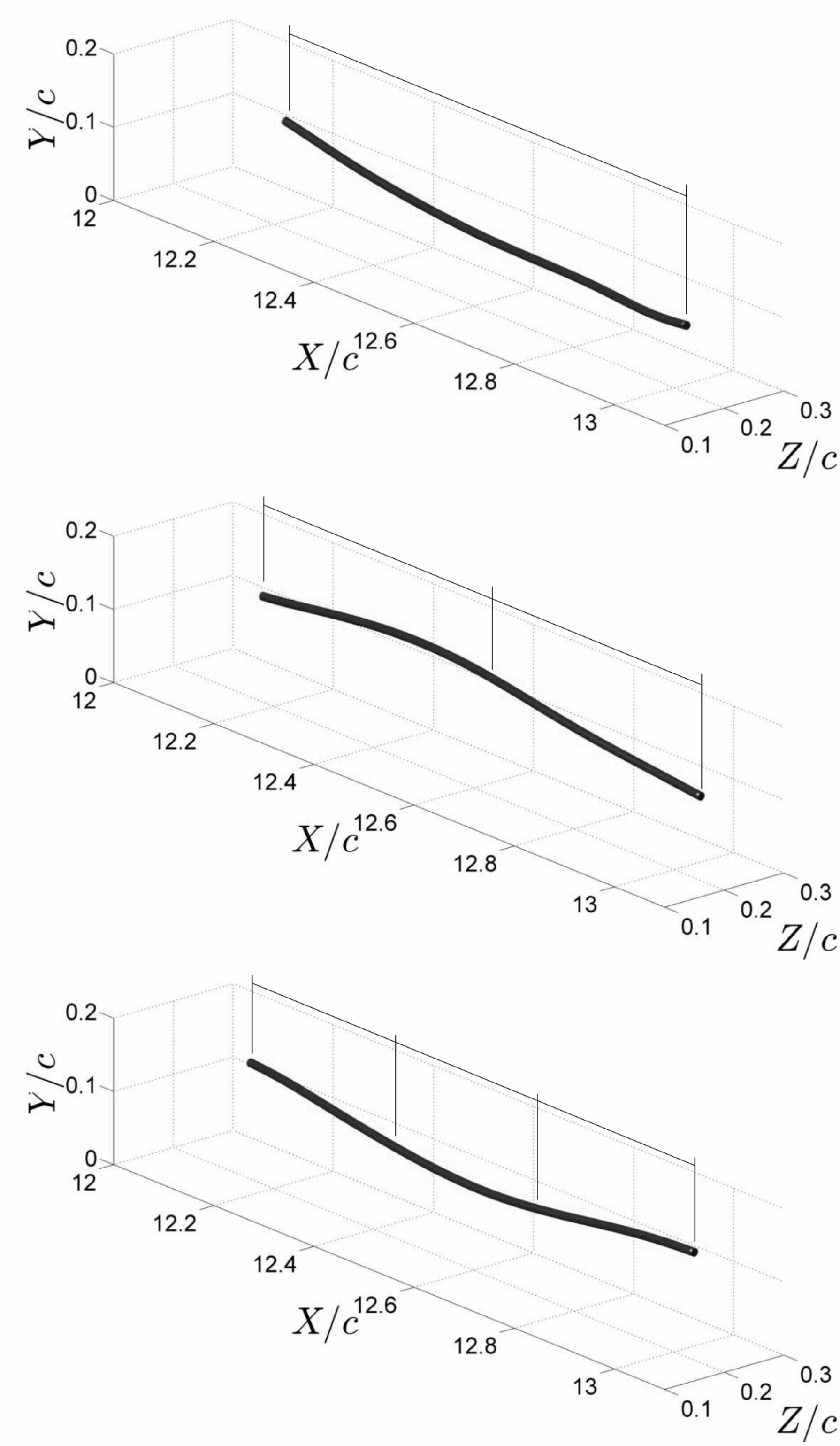

Figure 5.3: Examples of reconstructed vortex axes, in which the visible length appears to be a quarter of a wavelength (top), half a wavelength (middle), or three quarters of a wavelength (bottom).

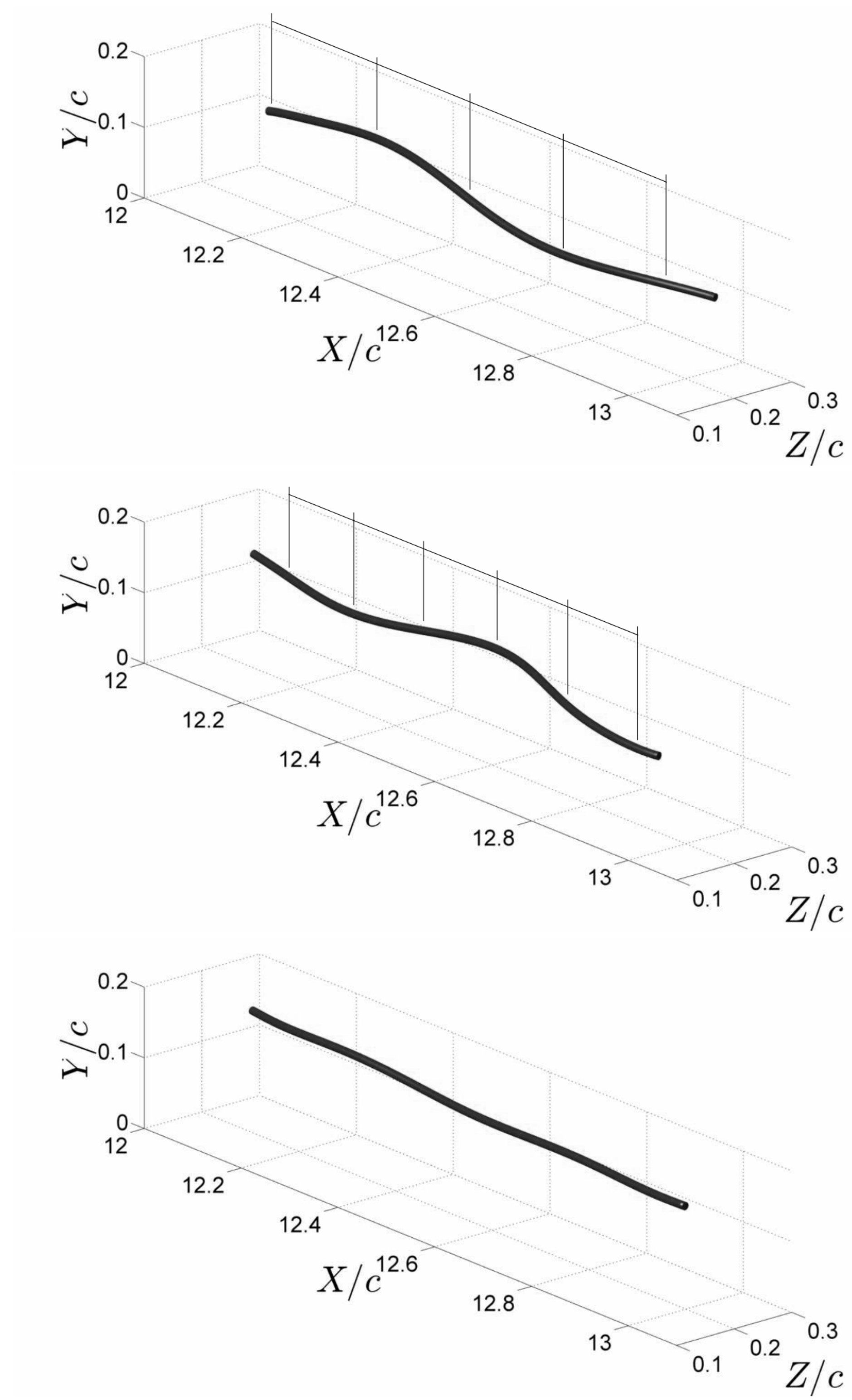

Figure 5.4: Examples of reconstructed vortex axes, in which the visible length appears to be a full wavelength (top), one and a quarter wavelength (middle), or not distinguishable as part of a wave (bottom).

Table 5.1: Wavelengths of vortex motion from XY and XZ dye images.

	X/c	Percent of images with specified wavelength						$\overline{\lambda}/c$
		3c	1.5c	c	0.75c	0.5c	Indiscernible	
No-grid	6.6	2	9	17	11	3	59	0.8
	12.8	0	16	27	27	1	29	0.8
Small-grid	6.6	4	12	35	7	0	42	0.7
	12.8	0	14	23	19	7	37	0.9
Large-grid	6.6	0	32	38	17	0	13	0.7

this conjecture.

At some instances, the vortex axis was observed to have a roughly helical shape over the length of the frame, however, these instances were sporadic. Moreover, the direction of rotation of the helices varied so their presence was taken to be incidental and not indicative of a consistent helical pattern in the vortex axis at a pitch discernible from these measurements.

5.1.4 Vortex axis inclination

The polynomials p_1 and p_2 that describe the vortex axis in the XY and XZ planes, respectively, were used to estimate the instantaneous local inclination angle Θ between the vortex axis and the streamwise axis. In this study, Θ was of particular interest because values of U_θ and U_x obtained from SPIV data assumed that the vortex axis was perpendicular to the measurement plane, namely parallel to the streamwise direction. Due to wandering, however, the vortex axis would generally be inclined with respect to the streamwise direction, which would introduce an error in the measurements of U_θ and U_x. The local axis inclination angle could be obtained from p_1 and p_2 as

$$\Theta = tan^{-1}\sqrt{\left(\frac{dp_1}{dX}\right)^2 + \left(\frac{dp_2}{dX}\right)^2}. \tag{5.3}$$

The ensemble averaged vortex axis coordinates Y_{ax} and Z_{ax} over the observed streamwise distance were found to vary roughly linearly with respect to the streamwise distance X from the wing. In all cases, the inclination of the mean vortex axis with

Table 5.2: Mean Θ values from XY and XZ dye images and the corresponding uncertainties $\delta U_{\theta,x}$ in SPIV measurements of U_θ and U_x.

	No-grid		Small-grid		Large-grid	
X/c	Θ [°]	$\delta U_{\theta,x}$ [%]	Θ [°]	$\delta U_{\theta,x}$ [%]	Θ [°]	$\delta U_{\theta,x}$ [%]
6.6	6	0.5	7	0.7	14	3.0
12.8	7	0.7	10	1.5		

respect to the streamwise axis was lower than 1.5°. The uncertainty in the orientation of the cameras constituted a potential misalignment bias in the measured X axis direction of roughly 2° from the true streamwise axis direction. This misalignment error could not be separated from the true inclination of the mean vortex axis coordinates with respect to the streamwise direction in these measurements. The mean location of the vortex axis was investigated more rigorously using SPIV data (see Section 5.2.4).

The uncertainty in the alignment of the vortex axis and the streamwise axis was taken into account in the estimation of the uncertainty $\delta U_{\theta,x}$ of the SPIV measurements of U_θ and U_x. The possible misalignment bias of 2° was added to the measured mean values of Θ to ensure that the uncertainty estimates of $\delta U_{\theta,x}$ were conservative. The precision uncertainty in the measured angle of inclination of the vortex axis with respect to X in each image was 5°, and the corresponding value for an average from 200 image pairs was 0.4°. Mean Θ and $\delta U_{\theta,x}$ values are given in Table 5.2.

5.2 Wandering of the vortex axis

For each freestream condition, the amplitude of vortex axis wandering was quantified by calculating the standard deviation of the vortex axis coordinates in the YZ plane from the time series of vortex axis locations. Independent measurements of Y_{ax} and Z_{ax} were obtained using three different measurement techniques: LIF images in the XY and XZ planes, LIF images in the YZ plane, and SPIV measurements in the YZ plane. The mean location of the vortex axis was estimated from the SPIV measurements.

5.2.1 Vortex wandering in the XY and XZ planes from dye images

Dye images in the XY and XZ planes were analyzed as outlined in Section 5.1. Time series of vortex axis locations were obtained by evaluating p_1 and p_2 from each frame at a specified streamwise location. The streamwise locations were chosen as the centres of the two measurement frames ($X/c = 6.6$ and 12.8), because the illumination of the dye was highest at these locations allowing the vortex core to be identified with the highest confidence. These locations also correspond to SPIV measurement planes so a direct comparison of wandering statistics was possible there. The standard deviations of the resulting series of vortex axis coordinates σ_Y and σ_Z for each set of images were calculated and are presented in Section 5.2.4.

5.2.2 Vortex wandering in the YZ plane from dye images

For each freestream condition, 1000 images of fluorescing dye in and around the vortex core were recorded at $X/c = 9.7$ in the YZ plane. Large-scale flow patterns are clearly shown by the dye patterns in these images (see Figure 4.14). In the no-grid case, the images are dominated by a single spiral pattern which appears to emanate from the vortex core (*e.g.*, Figure 5.5). In the small-grid case, some images show a spiral pattern similar to that seen in the no-grid case near the vortex core, however, more secondary spirals and dye 'arms' are visible around the vortex core indicating the presence of strong secondary structures (*e.g.*, Figure 5.6 a). Some images from the small-grid cases do not have a distinct spiral showing the location of the vortex core (*e.g.*, Figure 5.6 b). In the large-grid case the dye patterns are dominated by secondary structures and it is rarely possible to, even approximately, identify the location of the vortex core based on the dye patterns in the image. When images from the no- and small-grid cases are viewed sequentially, an obvious centre of rotation of the dye patterns emerges in nearly all cases. Whereas spiral patterns in individual dye images are indicative of the paths of dyed fluid injected at the wing-tip in and near the vortex core as it was convected downstream, the centre of rotation represents the location of the rotational axis of the vortex in the sequence of images being examined. The centre of rotation was, therefore, a more accurate representation of the location of the vortex axis than the location about which the dye appeared to be spiralling

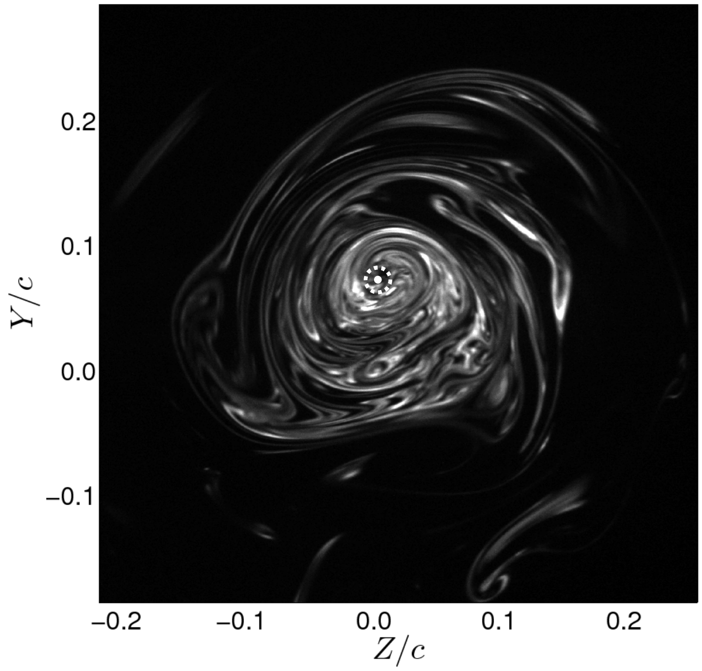

Figure 5.5: Sample of vortex axis identification in an LIF image in the YZ plane for the no-grid case; white dot marks the vortex axis, dotted line marks the uncertainty bounds.

out from. The location of the centre of rotation was identified visually for each image (see Figure 5.5). Three sequential images were inspected in rapid succession and the location of the apparent centre of rotation was recorded in the final frame. This method was used for images from the no- and small-grid cases, however, as it was rarely possible to identify a centre about which the dye patterns were rotating in the dye images from the large-grid cases, vortex axis locations were not obtained from those images. Estimates of σ_Y and σ_Z based on these measurements of the vortex axis location in the no- and small-grid cases will be presented in Section 5.2.4.

5.2.3 Vortex wandering examined with the use of SPIV measurements

Estimates of the vortex axis location based on analysis of planar velocity field measurements using different techniques were compared in order to ascertain the consistency of the corresponding estimates of Y_{ax} and Z_{ax} as well as their applicability of these techniques to the current experiments. Each approach was tested on a set of 100 SPIV velocity maps for all three freestream turbulence conditions at $X/c = 6.6$. A

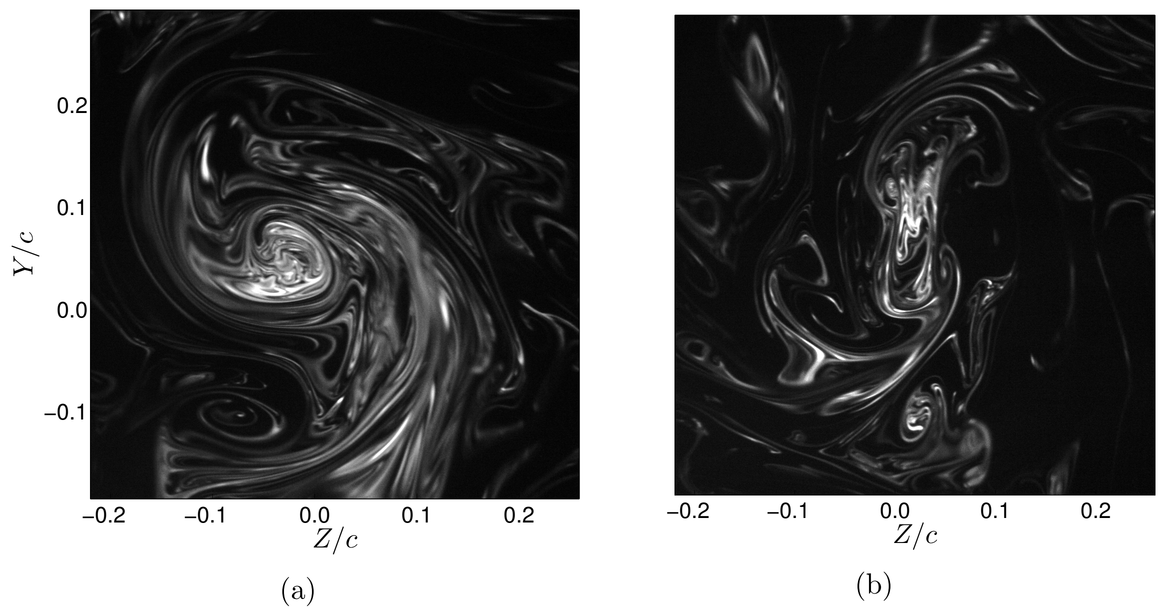

Figure 5.6: Sample LIF images in the YZ plane for the small-grid case: (a) an image in which a single distinct dye spiral is visible and (b) an image in which no distinct spiral is visible.

full explanation of each method follows. A comparison of the results of these methods is presented at the end of this section.

Scalar extrema

Several popular methods for determining vortex axis location rely on examining the variation of a scalar parameter that is expected to achieve an extreme value on the axis of a vortex, at least under idealized conditions. Two such scalars are the swirling strength

$$SS = max\left[0, -\left(\frac{\partial U_y}{\partial Z}\frac{\partial U_z}{\partial Y} - \frac{1}{2}\left(\frac{\partial U_y}{\partial Y}\frac{\partial U_z}{\partial Z}\right) + \frac{1}{4}\left(\frac{\partial U_y}{\partial Y}^2 + \frac{\partial U_z}{\partial Z}^2\right)\right)\right] \tag{3.9}$$

and the axial velocity deficit

$$\Delta U_x = U_\infty - U_x. \tag{5.4}$$

Both SS and ΔU_x were examined in this study. Peak values of these parameters were used to estimate the vortex axis location.

Smoothing

Non-uniformities in the flow and spurious velocities in the measured SPIV velocity fields can lead to erroneous extreme values in parameters that depend on the flow velocity vectors or their derivatives. To reduce the effect of these vectors, a smoothing filter was applied to the parameter fields being used to estimate the vortex axis location. The smoothing was accomplished in MATLAB by computing the 2D correlation of the scalar fields with a matrix of size $n \times n$ whose elements were equal and summed to unity. Samples of the effect of the smoothing on SS for correlation matrix sizes of $n = 2$ to 6 are shown in Figure 5.7. The size of the correlation matrix was selected based on the results of the smoothing of the SS field. A filter using a 4×4 matrix was chosen because at this size multiple local maxima of similar magnitude are no longer visible near the vortex axis and the peaks in swirling strength outside of the primary vortex have been reduced to the extent that they are significantly smaller than the peak in the vortex core.

Swirling Strength

The swirling strength is defined as the magnitude of the imaginary part of the eigenvalues of the velocity gradient tensor. Because SS depends only on velocity derivatives, it is not affected by the movement of the vortex as a whole (*i.e.*, it is Galilean invariant). The location with the highest swirling strength SS_{max} can, in some cases, produce useful estimates of the vortex axis location (van der Wall & Richard, 2006).

Axial velocity deficit

Another approach to vortex axis detection is to use the surplus or deficit of axial velocity in the vortex core as an indicator of the vortex axis position. SPIV velocity maps at all measurement planes in this study indicate that the vortex core is of the wake-like type, that is, it displays a consistent axial velocity deficit with respect to the freestream velocity. As with the swirling strength, a 4×4 smoothing filter was applied to the data before estimating the axis location. The location of the largest axial velocity deficit $\Delta U_{x,max}$ was used as an estimate of the vortex axis position.

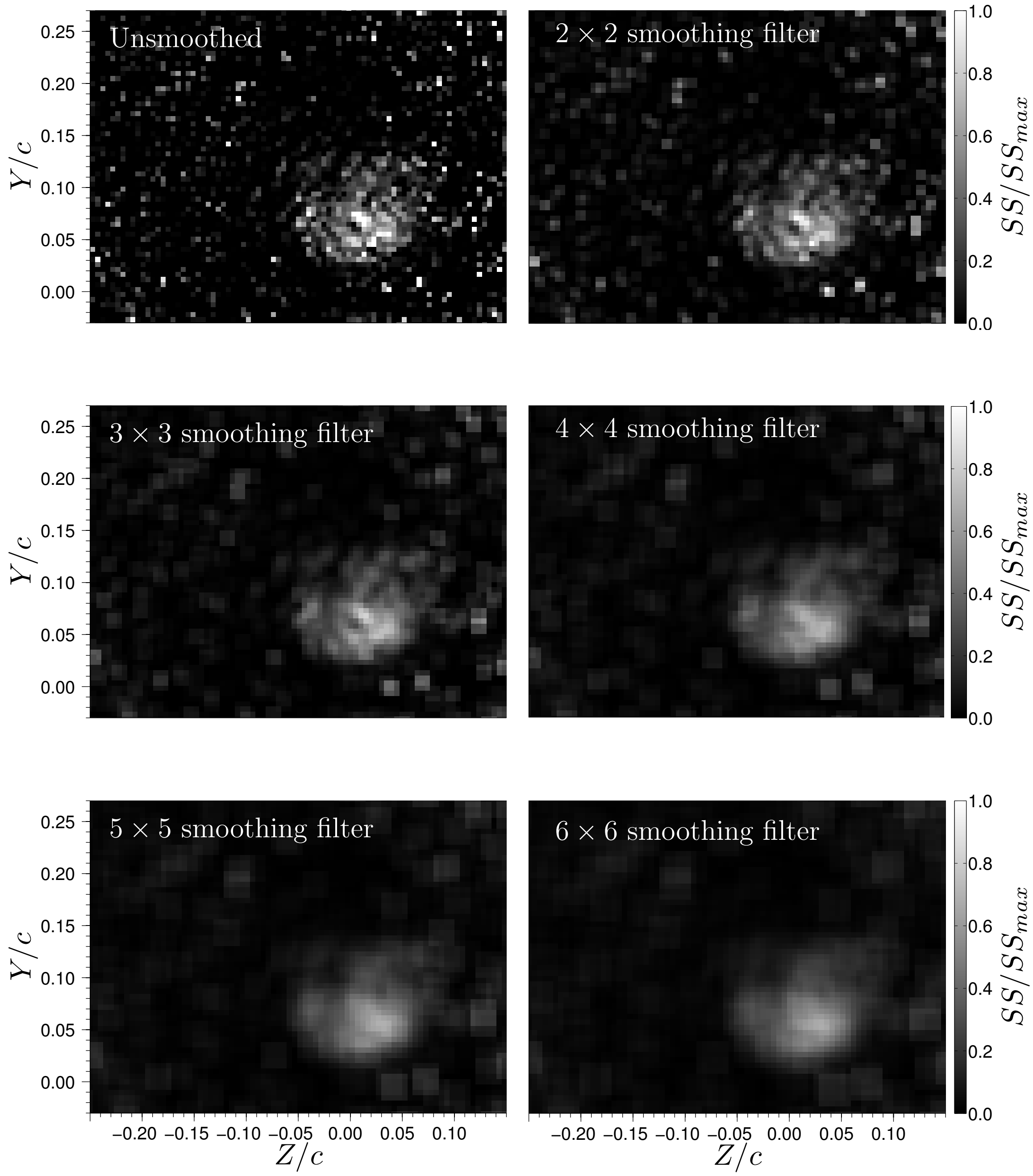

Figure 5.7: Smoothing filters of various sizes applied to the SS field from a single vector map.

Centre of mass of a scalar

Because of the presence of strong turbulence structures and the potential for spurious velocity vectors to have significant impacts on the location of the maximum value of these parameters, the centres of mass of SS and ΔU_x (using the SS and ΔU_x themselves as the mass parameters) were determined as additional indicators of the vortex axis location. These centre of mass based estimates are denoted $\Delta U_{x,COM}$ and SS_{COM}, respectively. Calculation of $\Delta U_{x,COM}$ and SS_{COM} was done in a limited area around the vortex axis so that the centres of mass were not significantly influenced by freestream structures. An additional concern in the selection of an appropriate area of consideration for the centre of mass calculations was that if, for example, SS_{COM} was determined using a calculation area centred on the location of SS_{max} and SS_{max} were significantly offset from the true location of the vortex axis, SS_{COM} may be biased towards the side of the vortex that SS_{max} was on. The same would be true for values of $\Delta U_{x,COM}$ determined based on a calculation area centred on $\Delta U_{x,max}$. This would result in discrepancies between SS_{COM} and $\Delta U_{x,COM}$ due to the differences between $\Delta U_{x,max}$ and SS_{max} and not solely due to differences in the overall distribution of values of SS and ΔU_x near the vortex axis. In order to ensure that SS_{COM} and $\Delta U_{x,COM}$ were not affected by this bias, the areas used in the centre of mass calculations were not centred on the locations of SS_{max} and $\Delta U_{x,max}$ but based on an independent estimate of the vortex axis location.

Q parameter

Hunt et al. (1988) suggested the Q-criterion as a means to define the spatial extent of a vortex. Q is defined in terms of the rate of strain tensor S and the rate of rotation tensor Ω as

$$Q = \frac{1}{2}\left(\|\Omega\|^2 - \|S\|^2\right). \tag{3.10}$$

The Q-criterion specifies that a vortex exists where there is a connected region in which Q is positive.

In this study, the Q parameter was used to generate an estimate of the vortex axis location that was independent of SS and ΔU_x. First, the location of the maximum

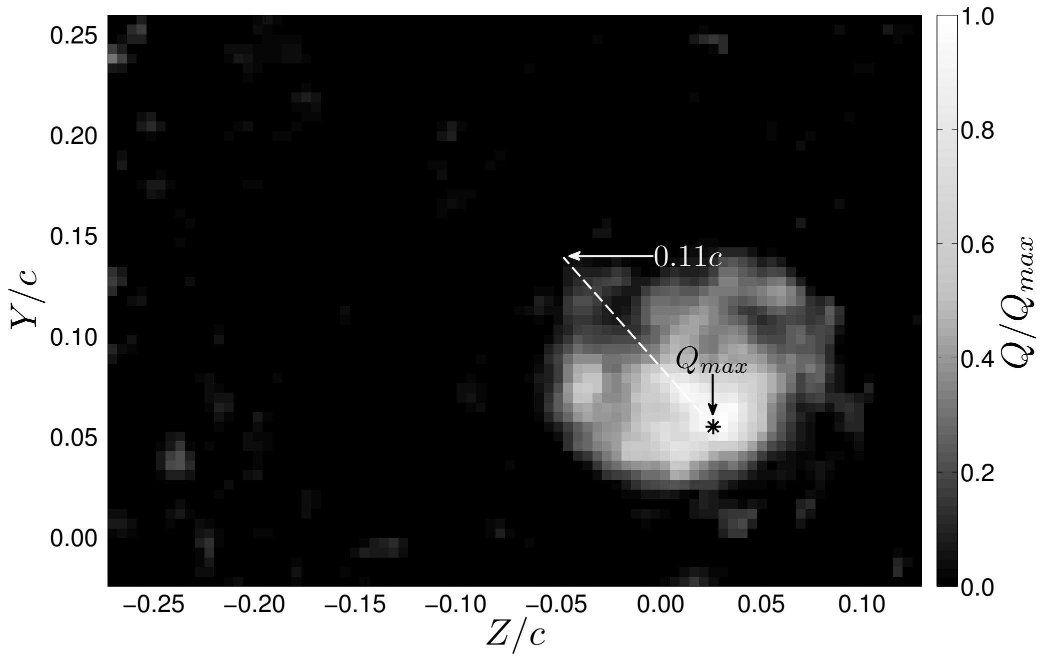

Figure 5.8: Q from a single vector map for the no-grid case at $X/c = 6.6$.

value of the Q parameter Q_{max} was found. Then the location of the centre of mass of the Q parameter Q_{COM} was determined based on a calculation area centred on the location of Q_{max}. It is noted that this method is subject to the same biases as the methods based on calculating the centre of mass of SS or ΔU_x in a calculation area centred on the location of their maximum values. Even so, the resulting estimate of Q_{COM} is expected to be a sufficiently accurate estimate of the vortex axis location for the purposes of centring the other centre of mass calculations. The values of Q_{COM} were, therefore, used as independent estimates of the location of the vortex axis on which to centre the areas of calculation for both SS_{COM} and $\Delta U_{x,COM}$.

Figure 5.8 shows the value of Q across the measurement frame from one vector field along with the location of Q_{max}. Ideally, the radius of the circular area used to compute the Q_{COM} would include the entire region where Q is positive due to the wing-tip vortex but not regions outside of the wing-tip vortex where Q is positive due to other vortical structures. In order to identify a suitable radius for the circular area over which Q_{COM} was to be calculated, the magnitude of the change in the location of the Q_{COM}, denoted $|\Delta YZ_Q|$, as the radius of consideration r_Q increased was examined for a sample of 100 vector maps at $X/c = 6.6$ for all freestream conditions. The ensemble averages of $|\Delta YZ_Q|$ normalized by the change in radius of consideration Δr_Q over which $|\Delta YZ_Q|$ occurs are plotted in Figure 5.9 ($\Delta r_Q = 0.01c$ for all cases). The radius of consideration corresponding to an area just encompassing the vortex core region was identified as the location where $|\Delta YZ_Q|$ began to settle towards a low value.

Examining the sample plot of Q in Figure 5.8 taken from the no-grid case, it can be seen that, very close to the location of Q_{max}, the value of Q remained very high in all directions. Moving away from the location of Q_{max} there is a marked increase in asymmetry in the values of Q. This asymmetry would cause the location of Q_{COM} to shift toward the side of the vortex containing higher values of Q as r_Q was increased and the area of consideration included the asymmetric region. A corresponding increase in $^{|\Delta YZ_Q|}/_{\Delta r_Q}$ as r_Q increases from zero can be seen in Figure 5.9. At a distance of $0.11c$ from the location of Q_{max} in Figure 5.8, the edge of the connected area of positive values of Q has been reached in all directions. In Figure 5.9a, we see that this corresponds to the location where $^{|\Delta YZ_Q|}/_{\Delta r_Q}$ begins to settle at a low value. This can be explained by the fact that, when the edge of the connected area of positive values of Q is reached on all sides (*i.e.*, the edge of the vortex core has been reached in all directions), additional changes in the vortex axis position estimate provided by Q_{COM} are due to freestream structures that are smaller and weaker than the primary vortex and cause only small changes in the location of Q_{COM}. For both the no- and small-grid cases $^{|\Delta YZ_Q|}/_{\Delta r_Q}$ begins to settle at approximately $r_Q/c = 0.11$ (see 5.9 a and b). For the large-grid case, the expected trend was not observed. It is likely that the difference in behaviour was primarily due to large powerful turbulent structures near the core, which began to affect Q_{COM} as soon as the edge of the vortex was reached in any direction. In the large-grid case at roughly $r_Q/c = 0.06$, $^{|\Delta YZ_Q|}/_{\Delta r_Q}$ begins increasing significantly (see Figure 5.9 c). It was assumed that this corresponded to the location at which the area of consideration for Q_{COM} began to encompass some strong secondary structures in the periphery of the vortex. In order to keep the estimate of Q_{COM} unbiased by these structures, the area of consideration for Q_{COM} was limited to $r_Q/c = 0.06$. If the size of the vortex core were roughly the

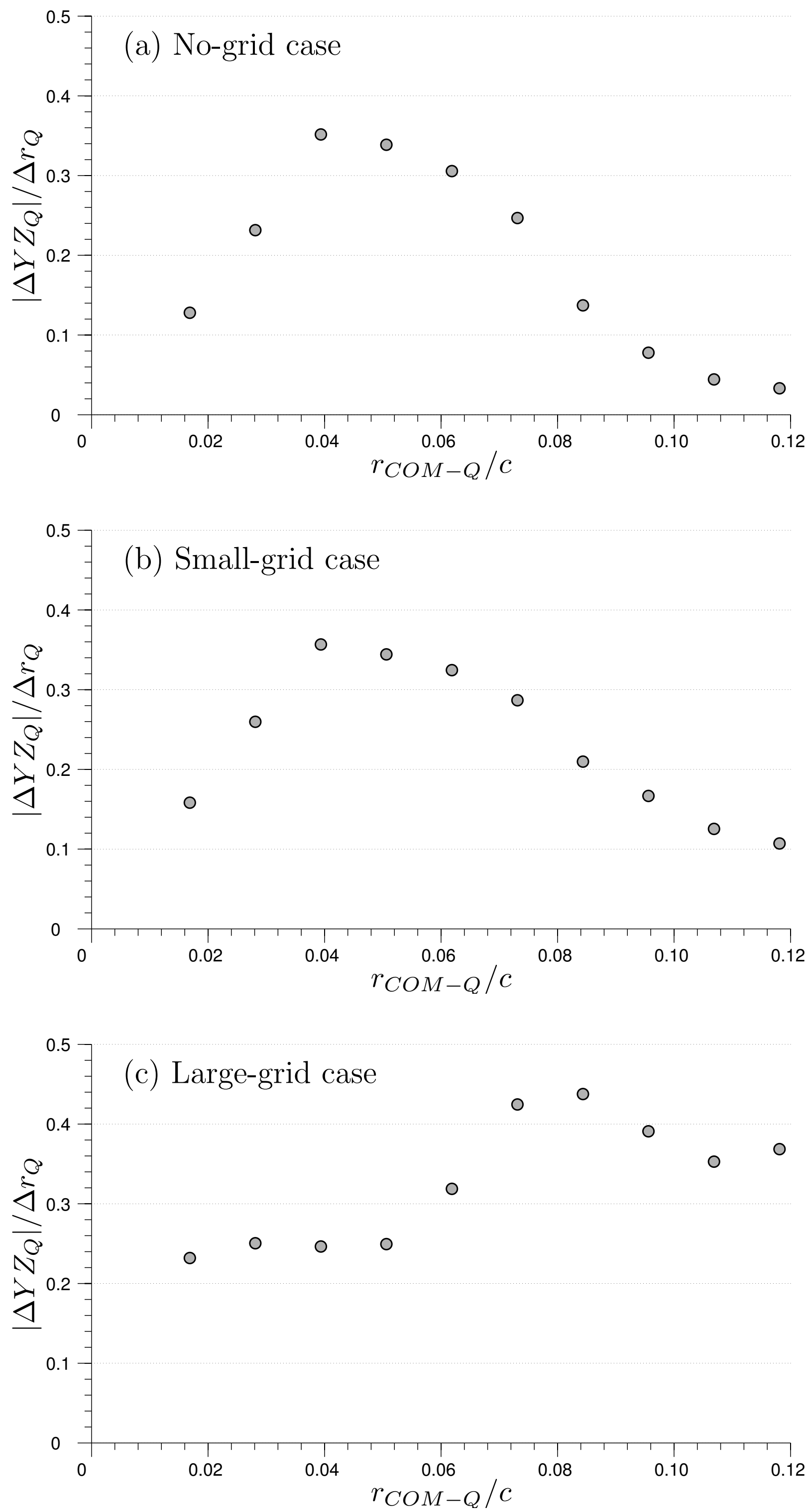

Figure 5.9: Magnitude of the change in the location of Q_{COM} versus the radius of consideration.

same in the large-grid case as in the no- and small-grid cases, limiting r_Q/c to 0.06 would result in measurements of Q_{COM} which would be based on areas of calculation that would be smaller than the vortex core. Calculating Q_{COM} over an area smaller than the true vortex core size would decrease the precision of the estimate of the vortex axis location provided by Q_{COM}, however, this was considered preferable to increasing the calculation area, which would introduce large errors due to the strong contribution of peripheral turbulent structures to ${}^{|\Delta YZ_Q|}/_{\Delta r_Q}$. It is also possible that the unexpected trends in $|\Delta YZ_Q|$ indicate that there are instances in which the vortex has broken down by the time it reaches the streamwise location of the measurement frame due to the turbulence generated by the large-grid.

The locations Q_{max} and Q_{COM} themselves were considered as alternative estimates of the vortex axis location.

Swirling Strength

The centre of mass of the swirling strength calculated over a circular area surrounding the vortex axis is an estimate of the vortex axis location that is based on the value of SS within the entire vortex core rather on a single peak in SS. The area of consideration used to calculate SS_{COM} was centred on the independent estimate of the vortex axis location provided by Q_{COM}.

As with Q_{COM}, the accurate calculation of SS_{COM} must be based on an area of consideration encompassing the entire area near the vortex axis where SS is significantly affected by the primary vortex. The optimal radius of the area considered for the calculation of SS_{COM} may be different from the one used for Q_{COM}. Additionally, the location of Q_{COM} may be slightly offset from the centre of region where the values of SS are significantly affected by the primary vortex. As previously described, the location of SS_{max} may also be slightly offset from the centre of region where the values of SS are significantly affected by the primary vortex. The location of SS_{COM} was based on a calculation area centred on Q_{COM}, because this is an independent estimate of the vortex axis location, however, the location of SS_{max} was used to aid in determining the radius for the area of consideration for SS_{COM} as is subsequently described. The locations of Q_{COM} and of SS_{max} were found to be relatively close to each other. This was evidenced by the fact that the average distance between Q_{COM} and SS_{max} for the first 100 frames for the no-grid case at $X/c = 6.6$ was $0.02c$, while the core radius of the vortex was estimated to be roughly $0.11c$ (*e.g.*, Figure 5.8). For small values of r_{SS}, estimates of SS_{COM} based on areas of consideration centred on SS_{max} and Q_{COM} may be separated by a distance similar to the distance separating SS_{max} and Q_{COM} themselves. As r_{SS} increases and becomes large enough for the entire vortex core to be included in the area of consideration for the calculations of SS_{COM} regardless of whether the area is centred on the location of SS_{max} or on Q_{COM}, the difference between the two estimates should be significantly reduced (see Figure 5.10). The difference between the values of SS_{COM} based on calculation areas centred on SS_{max} or Q_{COM} was quantified by calculating the correlation coefficient between them for different values of r_{SS}. Correlation coefficients were calculated for six values of r_{SS} between 0.02 and $0.17c$ for 100 frames at $X/c = 6.6$ for the three freestream conditions (Figure 5.11). The value of r_{SS} at which the correlation coefficient settled to a nearly constant value was used as the radius of consideration for the determination of SS_{COM}. For the no-grid case, the correlation coefficient value settled at $r_{SS} \approx 0.08c$, for the small-grid case at $0.06c$, and for the large-grid case at $0.11c$. It is important to note that for the no-grid and small-grid cases the asymptotic value of the correlation coefficient was not significantly lower than 1, whereas for the large-grid case it was roughly 0.6. This is consistent with the previous observations that the vortex axis can be located with fair accuracy in the no-grid and small-grid cases, but not in the large-grid case.

Axial velocity deficit

The centre of mass of ΔU_x calculated over a circular area surrounding the vortex axis was also used as an estimate of the vortex axis location. The area used in the centre of mass calculations was a circular region centred on Q_{COM}. In the same manner as for SS_{COM}, the radius of the area of consideration for Q_{COM} was determined by examining the correlation between $\Delta U_{x,COM}$ of an area centred on Q_{COM} and one centred on $\Delta U_{x,COM}$ for various radii of consideration r_{AD}. From Figure 5.12 it can be seen that the correlation settled at approximately $0.08c$ for the no- and small-grid

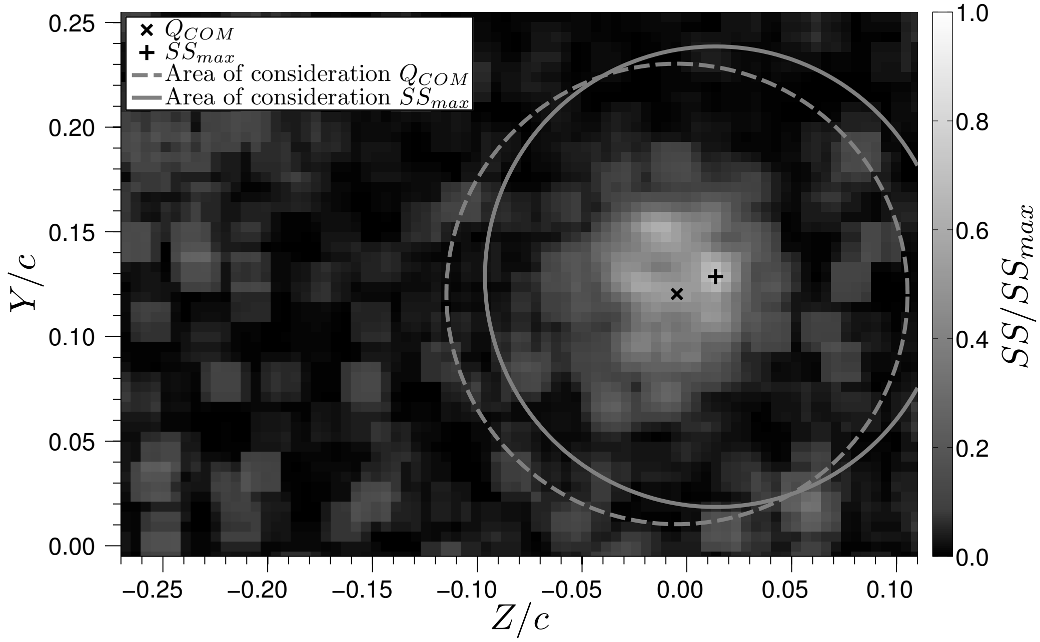

Figure 5.10: Areas of consideration centred on Q_{COM} and SS_{max} (radius of $0.11c$ in both cases).

cases and at approximately $0.14c$ for the large-grid case. These values were used to define the radius of consideration in the determination of estimates of the vortex axis location based on $\Delta U_{x,COM}$. As for the swirling strength, the correlation coefficients for the no- and small-grid cases were much closer to 1 than the one for the large-grid case.

Streamline identification

The location of the vortex axis was also estimated using the "streamlines" of secondary flows on cross-planes, based on the SPIV vector fields. The velocity vector map was overlain with streamlines of the secondary flows and the location of the vortex axis was identified visually as the location on which these streamlines seemed to be centred (see Figure 5.13). In the case of a stationary vortex, this method is expected to yield accurate results. However, this method is not Galilean invariant (*i.e.*, it would not produce the same results on a stationary vortex as on a translating vortex). If the vortex were not stationary, the location where the streamlines of the secondary flows spiral outwards from would not coincide with the true vortex

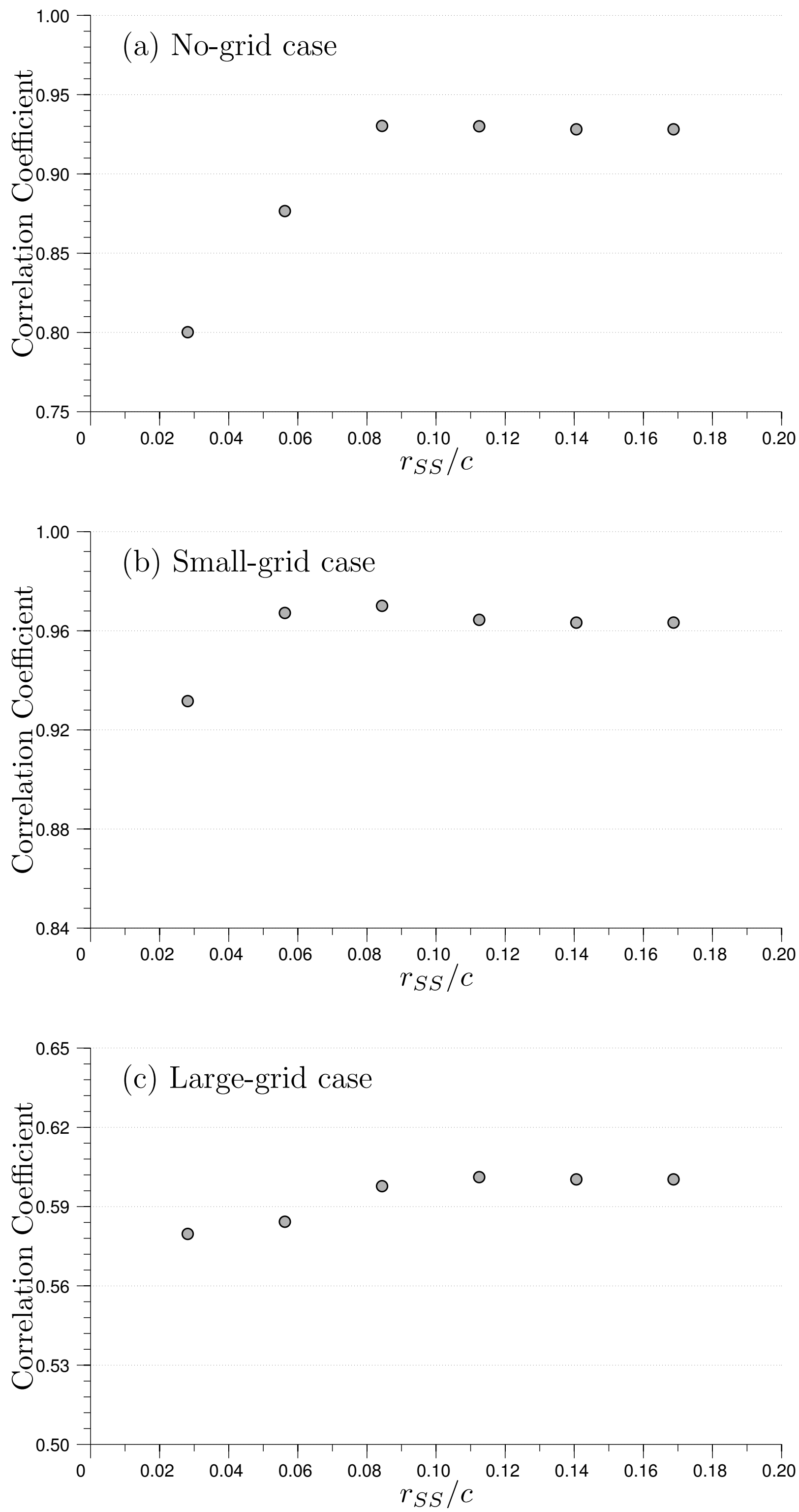

Figure 5.11: Correlation coefficient between the locations of the SS_{COM} determined using an area of consideration centred on Q_{COM} and SS_{max}.

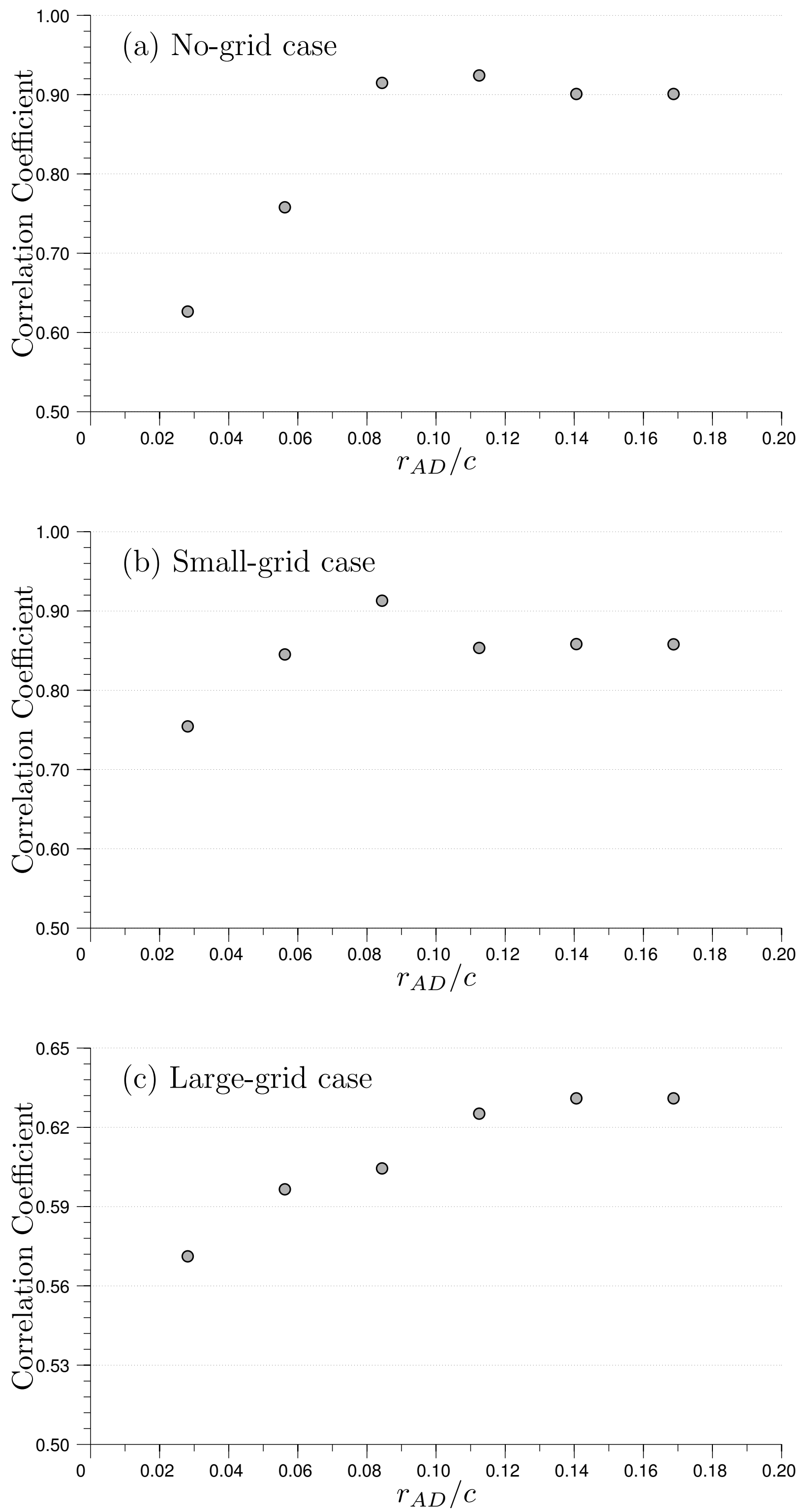

Figure 5.12: Correlation coefficient between the locations of the $\Delta U_{x,COM}$ determined using an area of consideration centred on Q_{COM} and $\Delta U_{x,max}$.

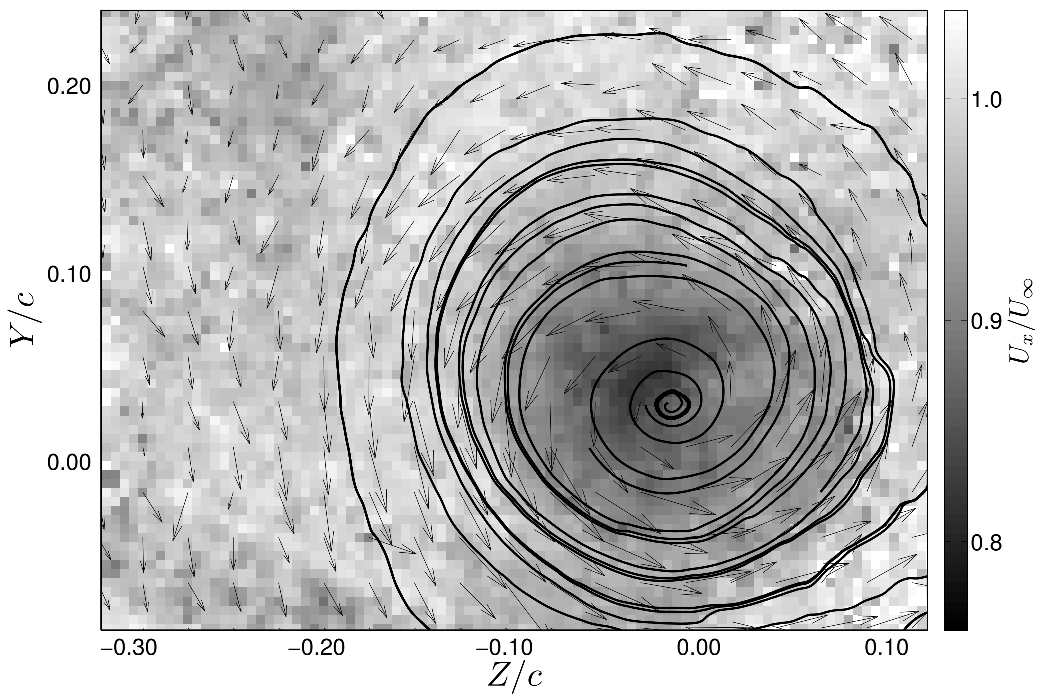

Figure 5.13: Sample velocity vector map overlain with streamlines of the secondary flows.

axis. The faster the vortex is translating, the less accurate this method would be. Additionally, some data frames, especially in the large-grid case, contained strong freestream structures, which deformed the streamlines of the secondary flows around the vortex axis making the estimation of the true vortex axis location by this method less precise.

Planar least-squares fit

Following an approach similar to the one used by Bhagwat and Ramasamy (2012), a planar least-squares fit (PLSF) was performed to estimate the vortex axis location. The least-squares error to be minimized in this technique is the discrepancy between the radial profile of azimuthal velocities U_θ across the vortex in the measured data and a radial profile of U_θ from a reference profile. The parameters being adjusted between iterations to minimize the least-squares error are the coordinates of the vortex axis Y_{ax} and Z_{ax}. The initial values of Y_{ax} and Z_{ax} were the estimates generated by the streamline technique. The reference profile of U_θ was determined by performing a

10^{th} order polynomial fit to measured data where the vortex axis has been aligned in each data frame using vortex axis coordinates which were identified by the streamline technique in each frame. The PLSF method is not Galilean invariant as it depends on velocity vectors and not their derivatives.

Comparison of vortex axis locations identified by different methods

Table 5.3 gives a summary of the results of each of the methods of vortex axis identification from the SPIV vector fields in terms of the standard deviation of the vortex axis coordinates (σ_z and σ_y) for all freestream conditions. Tables 5.4, 5.5, and 5.6 show the correlation coefficients between the vortex axis locations calculated using the different methods of identification in the no-grid, small-grid, and large-grid cases, respectively.

As discussed previously, a vortex has been identified in the present work as a circular or spiral flow pattern. This approach would be appropriate for a stationary vortex (Robinson, 1990), and so the streamline identification technique is expected to locate the vortex axis fairly accurately in the no-grid case, in which vortex wandering was relatively weak. Table 5.4, which lists the correlation coefficients between the locations identified by different methods for the no-grid case, shows that the SS_{COM}, Q_{COM}, and PLSF techniques identify vortex axis locations which are fairly close to those identified by the streamline method. Moreover, high correlation could be seen between the vortex axis locations identified as SS_{COM} and Q_{COM} as well as between the locations identified as SS_{max} and Q_{max}. There was, however, a significant difference between the locations identified by SS_{COM} and SS_{max}, as well as between the locations identified by Q_{COM} and Q_{max}. The discrepancy between SS_{COM} and SS_{max} is shown in Figure 5.10, where SS_{max} is not in the centre of the area containing high values of SS as indicated by SS_{COM}. Non-uniformities in the core velocity field may cause multiple local maxima of the SS in the vortex core or a single local maximum, which is offset from the true vortex axis location. As it is based on the overall trend of SS in the vortex core, SS_{COM} provides a more reliable estimate of the vortex axis location. This discrepancy is of particular importance as it illustrates the inadequacy of using SS_{max} as an indicator of the vortex axis location in strongly

Table 5.3: Standard deviation of vortex axis locations from SPIV data calculated using different techniques.

		SS_{max}	SS_{COM}	$\Delta U_{x,max}$	$\Delta U_{x,COM}$	Q_{max}	Q_{COM}	Streamline	PLSF
No-grid	σ_z/c	0.021	0.012	0.017	0.012	0.021	0.012	0.009	0.010
	σ_y/c	0.019	0.009	0.015	0.010	0.019	0.010	0.010	0.009
Small-grid	σ_z/c	0.034	0.031	0.027	0.027	0.034	0.031	0.026	0.025
	σ_y/c	0.032	0.028	0.031	0.025	0.032	0.028	0.025	0.025
Large-grid	σ_z/c	0.055	0.067	0.060	0.063	0.081	0.067	0.057	0.056
	σ_y/c	0.052	0.070	0.065	0.067	0.084	0.070	0.062	0.064

Table 5.4: Correlation coefficients between vortex axis locations identified using different techniques for the no-grid case.

	SS_{max}	SS_{COM}	$\Delta U_{x,max}$	$\Delta U_{x,COM}$	Q_{max}	Q_{COM}	Streamline	PLSF
SS_{max}	1							
SS_{COM}	0.68	1						
$\Delta U_{x,max}$	0.28	0.58	1					
$\Delta U_{x,COM}$	0.46	0.84	0.63	1				
Q_{max}	0.94	0.69	0.29	0.47	1			
Q_{COM}	0.71	0.98	0.57	0.84	0.73	1		
Streamline	0.65	0.85	0.51	0.74	0.65	0.84	1	
PLSF	0.51	0.82	0.55	0.81	0.52	0.82	0.91	1

Table 5.5: Correlation coefficients between vortex axis locations identified using different techniques for the small-grid case.

	SS_{max}	SS_{COM}	$\Delta U_{x,max}$	$\Delta U_{x,COM}$	Q_{max}	Q_{COM}	Streamline	PLSF
SS_{max}	1							
SS_{COM}	0.91	1						
$\Delta U_{x,max}$	0.61	0.71	1					
$\Delta U_{x,COM}$	0.69	0.79	0.78	1				
Q_{max}	0.99	0.91	0.61	0.69	1			
Q_{COM}	0.90	0.99	0.72	0.82	0.89	1		
Streamline	0.78	0.90	0.74	0.82	0.77	0.89	1	
PLSF	0.75	0.88	0.76	0.82	0.74	0.89	0.97	1

Table 5.6: Correlation coefficients between vortex axis locations identified using different techniques for the large-grid case.

	SS_{max}	SS_{COM}	$\Delta U_{x,max}$	$\Delta U_{x,COM}$	Q_{max}	Q_{COM}	Streamline	PLSF
SS_{max}	1							
SS_{COM}	0.58	1						
$\Delta U_{x,max}$	0.34	0.56	1					
$\Delta U_{x,COM}$	0.55	0.97	0.62	1				
Q_{max}	0.54	0.67	0.44	0.67	1			
Q_{COM}	0.58	1.00	0.55	0.97	0.66	1		
Streamline	0.43	0.59	0.62	0.63	0.52	0.58	1	
PLSF	0.47	0.61	0.62	0.63	0.57	0.60	0.92	1

turbulent flows.

The correlation coefficients for the cases of small- and large-grid turbulence show a good correspondence of the results of SS_{COM}, Q_{COM}, PLSF, and the streamline method (see Tables 5.5 and 5.6). The PLSF and the streamline method, however, are less reliable than SS_{COM}, Q_{COM} for the small- and large-grid cases, because the former are not Galilean invariant and the movement of the vortex core is expected to be significant in these cases. Additionally, the size and strength of turbulent structures in these cases often distort the streamlines of the secondary flows in and around the vortex core making the streamline identification technique more difficult to implement.

Based on these results, both Q_{COM} and SS_{COM} are likely to produce acceptable estimates for vortex axis location in an approximately two dimensional flow field. In a perfectly two-dimensional flow, the two parameters would theoretically produce the same results (Carmer et al., 2008). Even in the presently studied cases, which are not perfectly two-dimensional, there was a high correlation between Q_{COM} and SS_{COM}. In addition to three-dimensionality effects, discrepancies between the vortex axis locations based on these two parameters could be due to differences in the areas considered in the centre of mass calculations for Q and SS. In subsequent sections, we will consider SS_{COM} to be the best estimate of the location of the vortex axis.

5.2.4 Results of vortex axis wandering analysis

The mean location of the vortex axis was examined based on the axis locations from SPIV data, as the bias limit of the axis location from the LIF data was too high for any statistically significant information to be extracted from them. Figure 5.14 shows the mean vortex axis location along the flow. The precision uncertainty in individual measurements of the location of the vortex axis was estimated as the mean difference between the axis locations determined by the streamline method and those determined by SS_{COM}, which was $0.006c$, $0.012c$, and $0.053c$ for the no-grid, small-grid, and large-grid cases, respectively; for the mean vortex axis location, these values were reduced by a factor of roughly 45, which is equal to the square root of the number of vector maps used to generate the mean axis locations (2000). The bias limit of

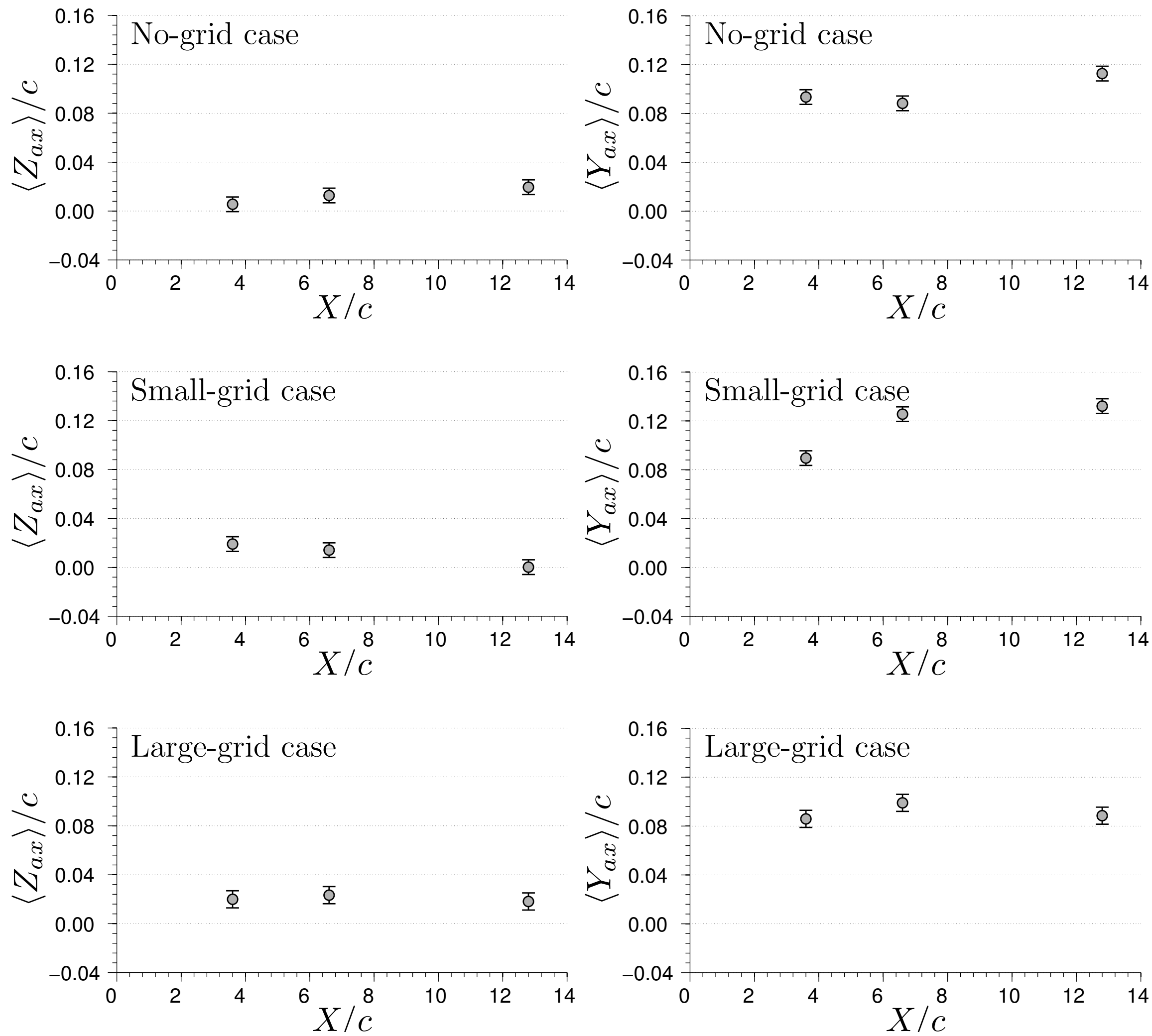

Figure 5.14: Mean vortex axis locations.

these values was taken to be $0.006c$, namely equal to the uncertainty in the positioning of the reference point on the calibration plate (Section 3.7.1).

The vortex is consistently located on the suction side of the wing (*i.e.*, $\langle Z_{ax} \rangle > 0$). No statistically significant change in the mean vortex location in the transverse direction Z occured under any freestream conditions. In the spanwise direction Y, the vortex was consistently inboard of the wing-tip (*i.e.*, $\langle Y_{ax} \rangle > 0$) showing a slight shift further inboard over the length of the test section for the no- and small-grid cases.

As a means to quantify the amplitude of vortex wandering, Table 5.7 summarizes the standard deviation of the vortex axis location in the Y and Z directions based on axis locations determined from the LIF images in the XY and XZ planes, the LIF images in the YZ plane, and the SPIV vector maps. The standard deviation of the vortex axis location derived from the SPIV data is shown in Figure 5.15 as the average of σ_Y and σ_Z (denoted σ_{ax}) for the all freestream turbulence cases and at all streamwise measurement planes. Uncertainty bars in this figure include both the uncertainty of the axis location in a given measurement and the uncertainty in the mean axis location. As expected, the vortex wandering amplitude increased strongly with increasing freestream turbulence intensity and length scale; it is noted, however, that the effect of the turbulence intensity cannot be separated from that of the turbulence length scale in the present experiments because they were increased simultaneously.

There is also a trend towards increasing vortex wandering amplitude with increasing distance downstream of the wing. The compounding of perturbations of the vortex by freestream structures moving downstream of the wing is expected to be a major factor in this increase in mean wandering amplitude. Additionally, a positive feedback mechanism is present in the vortices which could amplify upstream perturbations in the path of the vortex, as suggested by Rokhsaz et al. (2000). Segments of the vortex that are displaced from a straight line would induce a motion on each other through Biot-Savart induction (Hama, 1962). This induced velocity on the vortex core can cause some of its segments to wander further away from the mean axis location.

5.3 Velocity of the vortex core

5.3.1 Vortex velocity fields in different frames of reference

The velocity field of the vortex on a cross-plane (*i.e.*, a plane that is perpendicular to the streamwise axis X) depends on the frame of reference in which it is considered. Three frames of reference are relevant to this problem: a) the laboratory frame, b) a frame convected downstream with the freestream velocity, and c) a frame attached to the vortex axis. The objective in this study is to determine the induced velocity field of the vortex in a frame of reference attached to the vortex axis. To do so, we need

Table 5.7: Standard deviation of axial location.

Standard deviation of Z and Y axial locations									
		X/c							
		3.6		6.6		9.7		12.8	
		σ_Z/c	σ_Y/c	σ_Z/c	σ_Y/c	σ_Z/c	σ_Y/c	σ_Z/c	σ_Y/c
No-grid	SPIV	0.008	0.008	0.011	0.010			0.016	0.015
	XY/XZ LIF			0.015	0.016			0.016	0.024
	YZ LIF					0.012	0.012		
Small-grid	SPIV	0.023	0.023	0.028	0.028			0.028	0.028
	XY/XZ LIF			0.021	0.025			0.023	0.033
	YZ LIF					0.023	0.028		
Large-grid	SPIV	0.044	0.047	0.064	0.063			0.074	0.072
	XY/XZ LIF			0.044	0.053				
	YZ LIF								

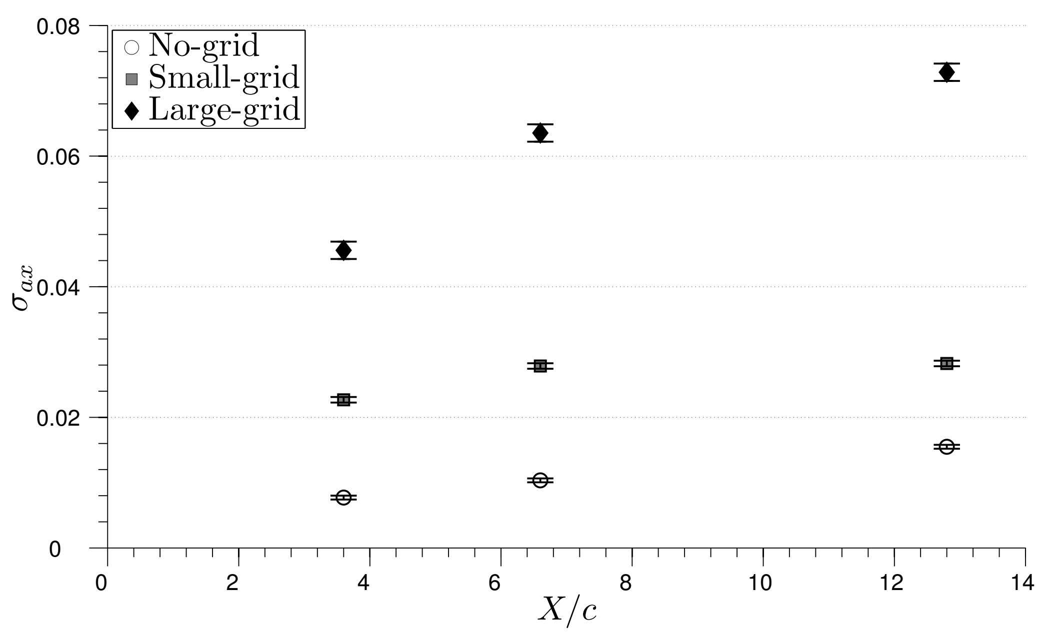

Figure 5.15: Standard deviation of axis location.

to know the instantaneous position of the vortex axis on each plane of measurement and the instantaneous velocity of the vortex axis.

The vortex axis position on a fixed cross-plane changes from one instant to another as a result of two distinct motions.

i. The vortex as a whole is convected downstream by the main stream and so, unless the vortex axis were a straight line parallel to the freestream direction (which is not true in any of the present cases), its intersection with the measurement cross-plane shifts on this plane in time (see Figure 5.16 a). This change in position on the measurement cross-plane in time would appear to represent transverse motion of the vortex axis even if the axis waveform were frozen. The apparent motion of the vortex axis in the case of a vortex with a frozen axis waveform, however, does not correspond to a transverse velocity of the fluid on the vortex axis and would not influence SPIV vector maps. For this reason, the induced velocity field of the vortex is not affected by convection.

ii. The axis waveform generally deforms in time (see Figure 5.16 b). Like the convection of a frozen axis waveform, deformation of the waveform causes the location of the intersection of the vortex axis with the measurement cross-plane to shift in time. This deformation also introduces a non-zero cross-plane velocity of the fluid on the vortex axis, which will be referred to as the axis deformation velocity vector $\mathbf{U_{def}}$. This velocity would be present in the SPIV measurements of the vortex velocity field and needs to be subtracted from these measurements before the vortex-induced velocity field can be estimated.

It is noted that, unlike SPIV measurements, LIF images in the cross plane are subjected to vortex axis motion that is due to the effects of both convection and deformation. The apparent velocity due to this movement will be referred to as the vortex planar movement velocity vector $\mathbf{U_{VPM}}$.

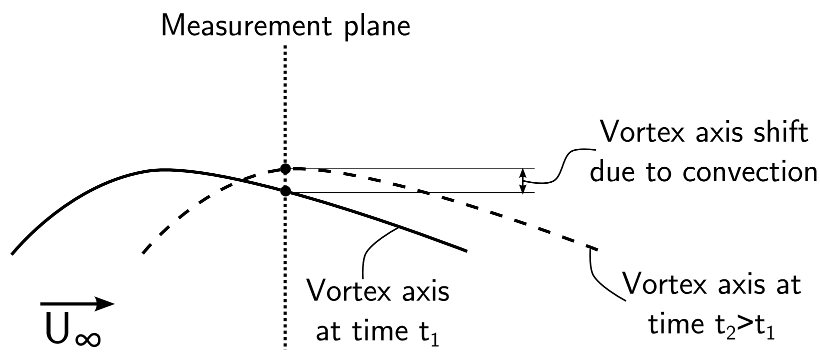

(a)

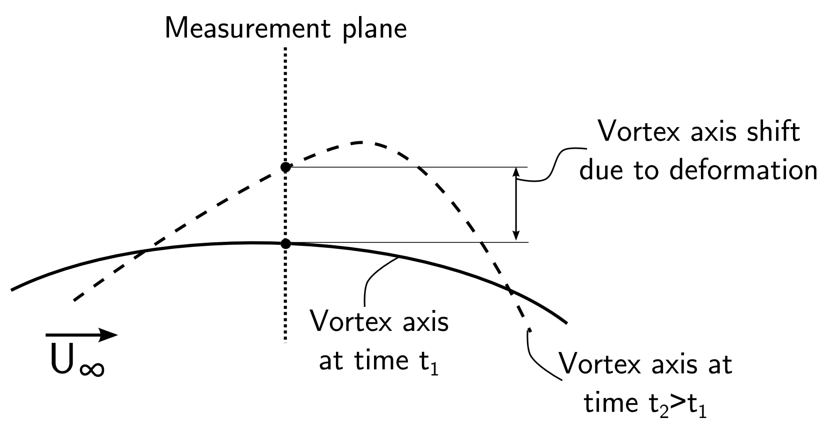

(b)

Figure 5.16: Illustration of convection of the vortex axis waveform (a) and of deformation of the vortex axis waveform (b).

5.3.2 Axis deformation velocity

In order to determine the velocity field induced by the wandering vortex in a frame of reference that is attached to the vortex axis, the instantaneous $\mathbf{U_{def}}$ must be subtracted from the measured velocity vectors across the vortex in each frame. For the purposes of this study, the vortex is assumed to move as a rigid body, which is to say, $\mathbf{U_{def}}$ is assumed to be constant across the vortex. For a non-wandering axisymmetric vortex, the spatially averaged cross-plane Cartesian velocity components U_y and U_z across the vortex would both be zero. For a wandering axisymmetric vortex, the average cross-plane Cartesian components would be non-zero and their vector sum would be equal to $\mathbf{U_{def}}$. Under the assumption of approximate axisymmetry of the vortex, the instantaneous $\mathbf{U_{def}}$ was estimated as the vector sum of the average Cartesian velocity components $U_{y,def}$ and $U_{z,def}$ over a circular area with a radius r_{def} and centred on the vortex axis. In order to determine an appropriate radius for the area of calculation, $U_{y,def}$ and $U_{z,def}$ were plotted versus the radius over which they were calculated. Near the vortex axis there was some variation of $U_{y,def}$ and $U_{z,def}$, however, examination of radial profiles from instantaneous vector maps demontrated that there were fairly consistent radii for each freestream condition at which the values of $U_{y,def}$ and $U_{z,def}$ reached plateaus. These radii, which were $0.055c$, $0.045c$, and $0.035c$ for the no-grid, small-grid, and large-grid cases, respectively, were used to define the areas over which the deformation velocity of the vortex axis were calculated.

For the purposes of this study, the vortex was assumed to translate in the cross-plane as a rigid body. However, the estimated value of $\mathbf{U_{def}}$ showed some weak dependence on the radius of the area over which it was calculated. This may be attributed to non-axisymmetry of the vortex in individual vector maps and turbulence in the vortex core.

The means and standard deviations of the magnitude $\mathbf{U_{def}}$ of the deformation velocity for all freestream flow conditions at X/c = 3.6, 6.6, and 12.8 are shown in Figure 5.17. As expected, both properties increase with increasing freestream turbulence. Another observation that can be made is that both properties decrease with increasing distance downstream of the wing; this can be possibly attributed to the corresponding streamwise decrease of turbulence intensity.

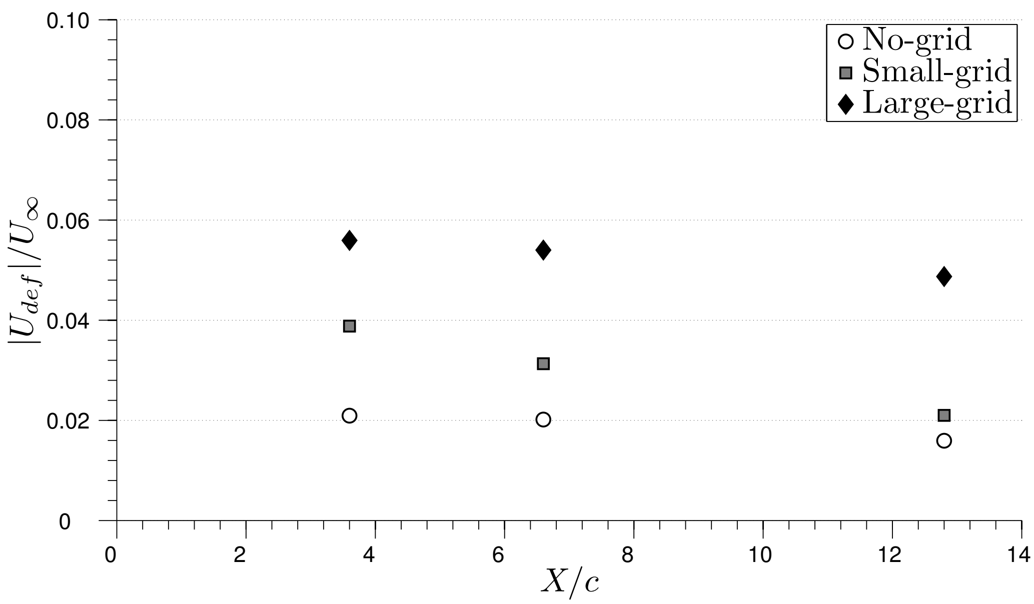

(a)

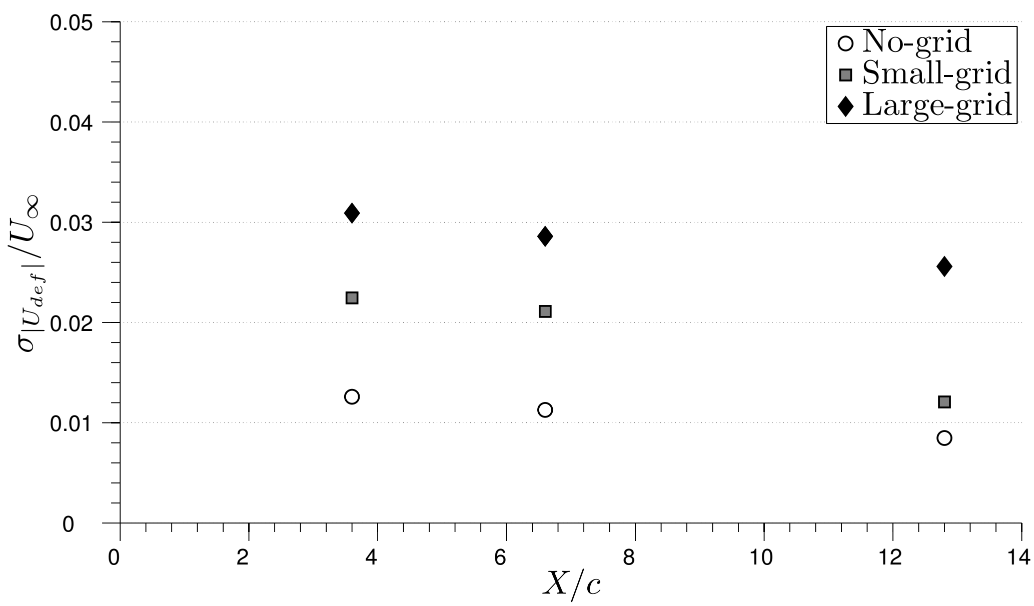

(b)

Figure 5.17: Average vortex axis deformation velocities (a) and standard deviation of vortex axis deformation velocities (b).

Table 5.8: Mean and standard deviation of the vortex planar movement velocity magnitude at $X/c = 9.7$.

	No-grid	Small-grid
$\lvert\mathbf{U_{VPM}}\rvert/U_\infty$	0.25	0.40
$\sigma_{\lvert\mathbf{U_{VPM}}\rvert}/U_\infty$	0.15	0.27

5.3.3 Vortex planar movement velocity

The vortex planar movement velocity $\mathbf{U_{VPM}}$ was calculated from LIF images in the YZ plane using the vortex axis locations which were identified as described in Section 5.2.2. It represents a combination of the effects of the convection of the vortex axis waveform and the deformation of the vortex axis waveform. The magnitude of $\mathbf{U_{VPM}}$ at a time t_i was calculated using a central difference scheme as

$$|\mathbf{U_{VPM}}(t_i)| = \frac{\sqrt{\left(Z_{ax}(t_{i+1}) - Z_{ax}(t_{i-1})\right)^2 + \left(Y_{ax}(t_{i+1}) - Y_{ax}(t_{i-1})\right)^2}}{(t_{i+1} - t_{i-1})}, \tag{5.5}$$

where t_i is the time at which a frame i was recorded and $Y_{ax}(t_i)$ and $Z_{ax}(t_i)$ are the Y and Z coordinates of the vortex axis location at time t_i, respectively. The mean and standard deviation of $|\mathbf{U_{VPM}}|$ are shown in Table 5.8. The uncertainty in the identification of each vortex axis location ($\pm$ 0.01c for the no-grid case and $\pm$ 0.02c for the small-grid case) is very high relative to the magnitude of the movement of the vortex axis between frames (the average vortex axis displacement between frames was 0.003c for the no-grid case and 0.004c for the small-grid case). As a result, the uncertainty in the mean $|\mathbf{U_{VPM}}|$ is also high at 50 % and 60 % for the no- and small grid cases, respectively. Even so, it can be seen that $\mathbf{U_{VPM}}$ is approximately one order of magnitude larger than $\mathbf{U_{def}}$. It can be concluded, therefore, that the observed movement of the vortex axis location in the YZ plane is primarily due to convection of the vortex axis in the streamwise direction and not to deformation of the vortex axis waveform.

5.4 Reconstruction of the velocity field of the vortex

After determining the coordinates of the vortex axis and $\mathbf{U_{def}}$ in each vector map, the coordinate system was translated to a new coordinate system whose origin coincided with the position of the identified vortex axis on that plane. Then, the Cartesian components $U_{y,def}$ and $U_{z,def}$ were subtracted from the corresponding measured velocity components to reconstruct approximately the velocity field that was induced by the vortex in a frame of reference moving with the vortex axis. The resulting velocities on the cross-plane were then expressed in polar coordinates to yield the azimuthal U_θ and radial U_r velocity components. Ensemble averaged values of U_r were between -0.5×10^{-4} and 1.5×10^{-4} m/s for all cases; such values were lower in magnitude than the measurement uncertainty, which was equal to 6.0×10^{-4} m/s, and will therefore be considered as negligible and will not be discussed further. It is also noted that the angle of incidence of the vortex axis to the plane of measurement was sufficiently small (see Table 5.2) and the cross-plane wandering velocity of the vortex was much smaller than the axial velocity U_x for U_x to require no correction for vortex wandering effects.

Radial profiles of the adjusted azimuthal and axial velocity components in the vortex were determined as circumferential averages around the vortex axis. First, the total area of each velocity map on a cross plane was divided into annular bins with increments in radius equal to $0.001c$. Then, all values of the adjusted velocities U_θ and U_x within each annular bin from all instantaneous velocity maps for a given case were averaged to produce bin averages. Finally, a 10^{th} order polynomial, in terms of the radial coordinate, was fitted to the bin averages for each set of measurements to produce the radial profile of the corresponding velocity component. It is noted that this approach resulted in polynomials that were not biased towards large radii, which would have been the case if these polynomials were fitted to un-binned data in view of the fact that the number of measurements at a given radius from the vortex axis was proportional to the square of the radial distance from the vortex axis.

Figure 5.18 shows representative cases of radial profiles of the azimuthal and axial velocities with the corresponding instantaneous bin averages also shown. The scatter in instantaneous data points was lowest for the no-grid case and highest for the large-grid case. The scatter also increased with increasing streamwise distance from the wing. The fits of the polynomials to the binned data were very good in all cases, with the standard deviation of the bin averages from the polynomial not exceeding $0.8 \times 10^{-3} U_\infty$. As an example of the significance of the correction for vortex wandering on the calculation of radial profiles, Figure 5.19 shows a radial profile of $\langle U_\theta \rangle$ for the small-grid case at $X/c = 6.6$ in the laboratory frame of reference, together with a profile of the same property in the frame of reference that was attached to the vortex axis (wandering frame of reference). Significant differences may be observed between the two profiles, especially within the vortex core. The effect of changing the frame of reference from the laboratory frame to the wandering frame was more significant for cases in which the amplitude of vortex wandering and the speed with which the vortex axis moved were greater, *i.e.*, cases further downstream of the wing and cases with stronger turbulence in the freestream.

5.5 Axial velocity variation

The streamwise evolution of the radial profiles of the normalized axial velocity in the vortex for the no-grid, small-grid, and large-grid cases are shown in Figure 5.20. In all cases considered, the axial velocity was lower than the freestream velocity. The velocity deficits decreased monotonically with radial distance and showed trends towards asymptotes far from the axis. Within the core region, the velocity deficit also decreased monotonically and significantly with distance from the wing (see Figure 5.21). Outside the core the streamwise rate of change of the velocity deficit was very low and could be positive zero or negative, depending on freestream conditions and location. The radius of this core region was roughly $0.07c$ for the no-grid case and increased to approximately $0.085c$ for the two grid cases.

The radial profiles of U_x/U_∞ for the three freestream turbulence conditions have been plotted together at $X/c = 3.3$, 6.6, and 12.8 in Figure 5.22 to illustrate the effect of freestream turbulence conditions on the velocity deficit. At all streamwise locations, the velocity deficit within a core region near the vortex axis was lower in the small-grid case than in the no-grid case and diminished further in the large-grid

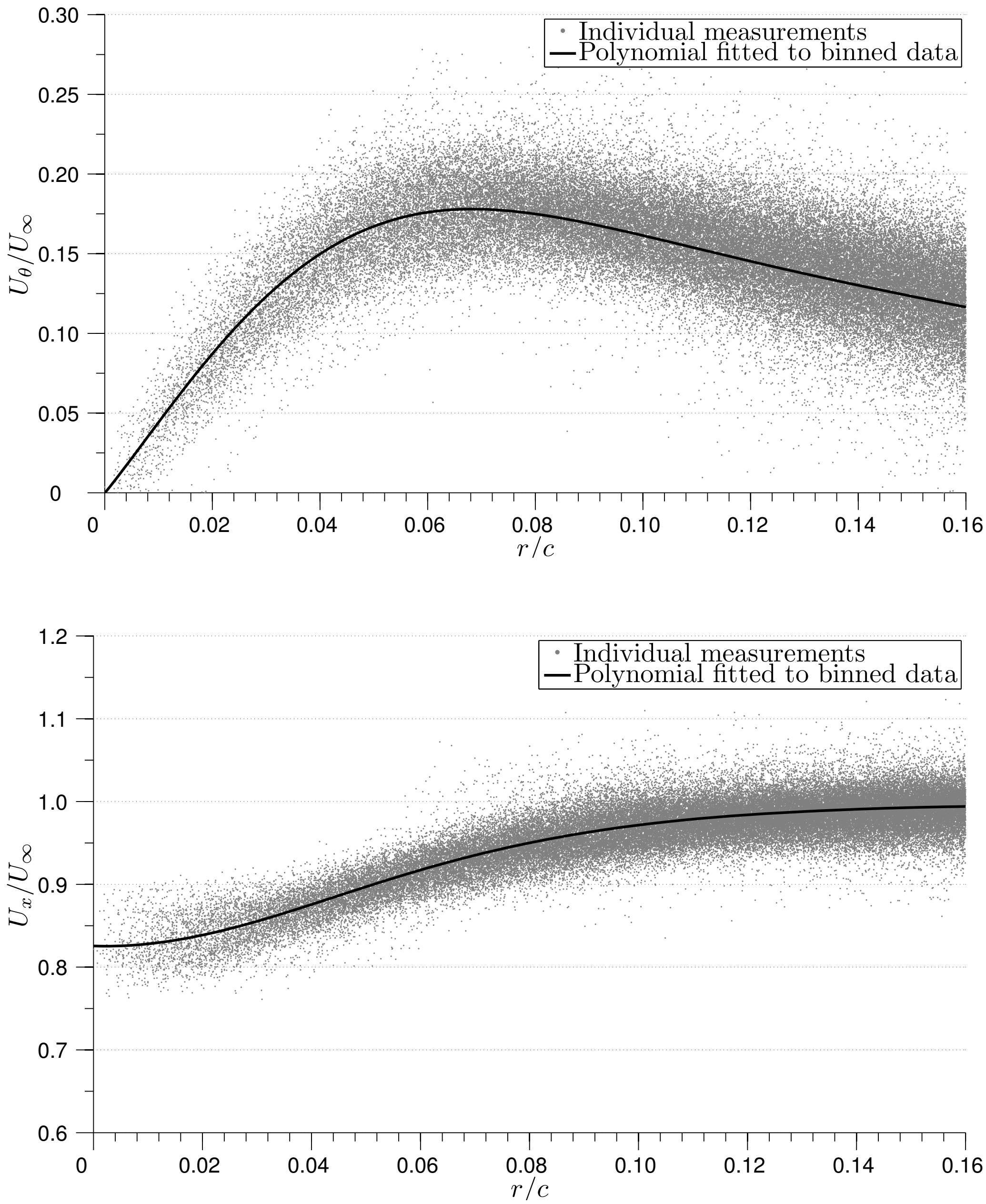

Figure 5.18: Examples of measured values of U_θ and U_x along with polynomials fitted to averages of these values within annular bins with radial increments equal to $0.001c$ ($X/c = 6.6$, no-grid case).

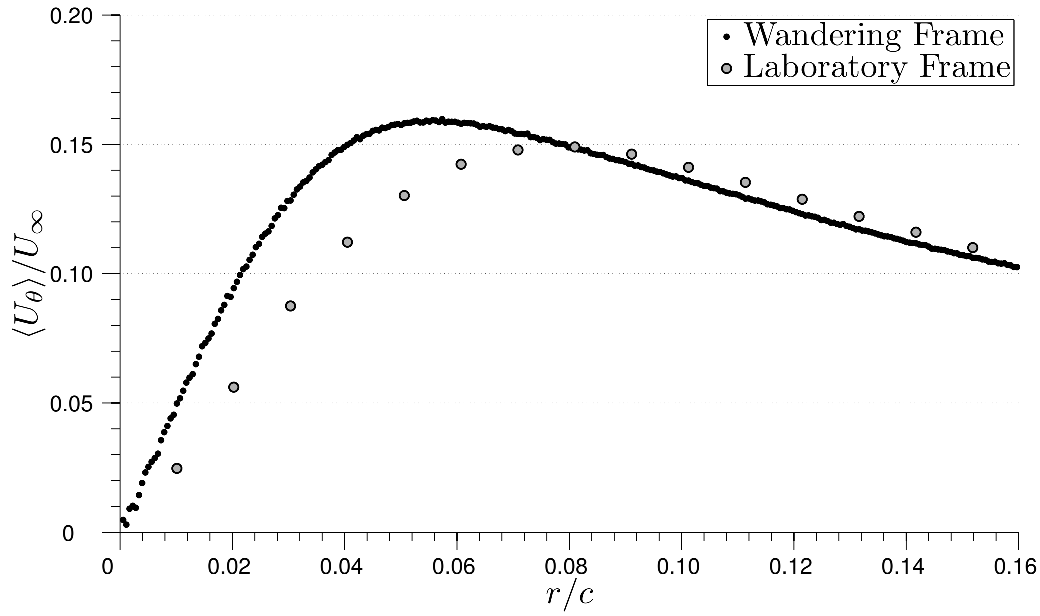

Figure 5.19: Radial profiles of U_θ in the laboratory and wandering frames of reference ($X/c = 3.6$, small-grid case).

case. Outside the core, the ordering was reversed, although differences among the three cases were relatively small.

5.6 Azimuthal velocity variation

Figure 5.23 a, b, and c show the evolution of the characteristic radial profiles of U_θ/U_∞ downstream of the wing for the no-grid, small-grid, and large-grid cases, respectively.

Figure 5.23 shows that, in both the no- and small-grid cases, the peak U_θ/U_∞ decreased in magnitude and its location moved to larger radii as the distance downstream of the wing was increased. This trend is shown more clearly in Figures 5.24 and 5.25, which show the radial position of the peak azimuthal velocity and the value of the peak azimuthal velocity, respectively for the three freestream conditions at all measurement planes. For the large-grid case, a peak in the U_θ/U_∞ profile was only discernible within the measurement area for the measurement plane at $X/c = 3.6$. At $X/c = 6.6$ and 12.8, the U_θ/U_∞ profiles in the large-grid case did not achieve distinct peaks within the measured radial extent. Instead, these profiles rose and

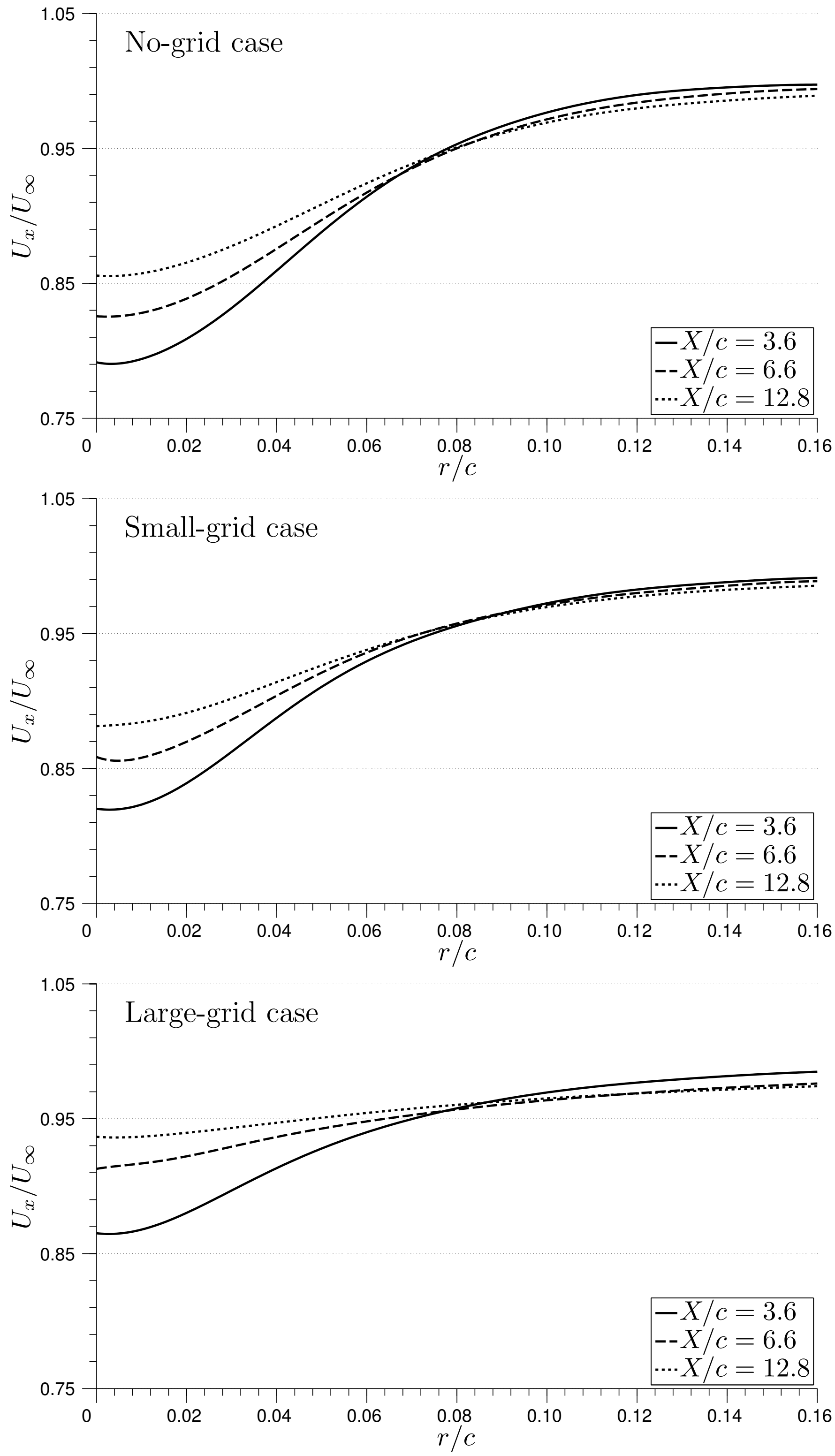

Figure 5.20: Radial profiles of axial for the no-grid, small-grid, and large-grid cases.

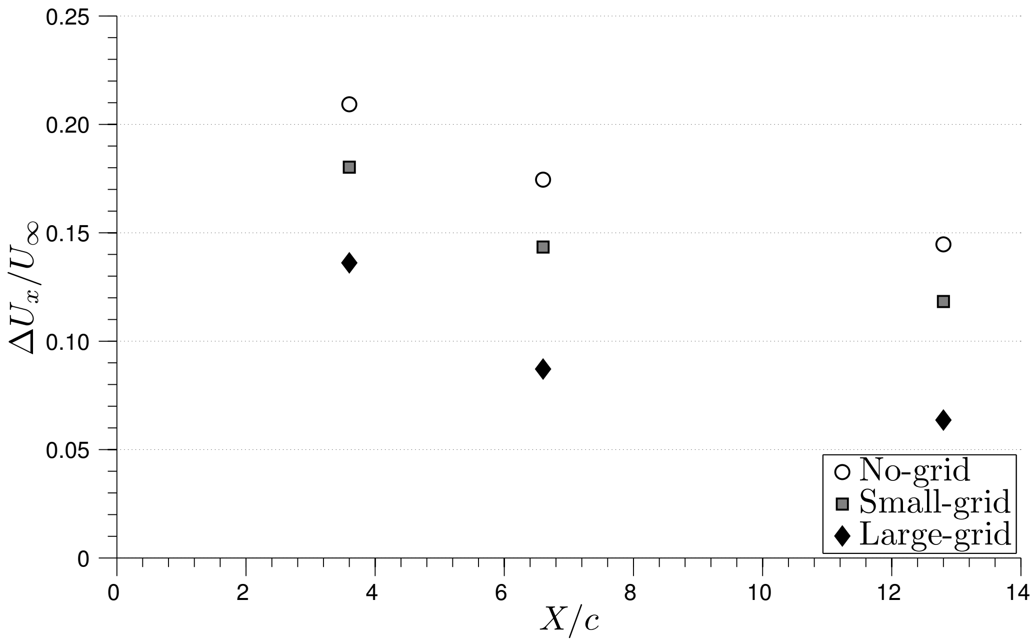

Figure 5.21: Axial velocity deficits ΔU_x.

became nearly flat beyond $r/c = 0.08$. The lack of apparent peaks in azimuthal velocity observed in the large-grid cases is inconsistent with conventional vortex velocity profiles. It may be attributed, at least in part, to stripping of core angular momentum by strong freestream turbulent eddies. For all freestream conditions, the values of U_θ/U_∞ at all radial locations decreased with increasing distance from the wing. It is interesting to note that the decrease in U_θ/U_∞ in the large-grid case between $X/c = 3.6$ and 6.6 was much greater than in either of the other freestream turbulence cases.

The slope of the U_θ/U_∞ profiles in the vortex core decreased with increasing distance downstream of the wing in all cases. At the vortex axis U_θ is zero for an ideal vortex. In the no- and small-grid cases, deviations at the vortex axis from $U_\theta/U_\infty = 0$ were minimal. In the large-grid case, U_θ at the vortex axis was between 1 and 2.5 % of U_∞. This may indicate that the vortex axis was not identified as precisely in these cases as in the no- and small-grid cases and also that the vortex translation velocity was not calculated as accurately as well as being variable across the vortex.

Figure 5.26 shows the characteristic radial profiles of U_θ/U_∞ for the three freestream

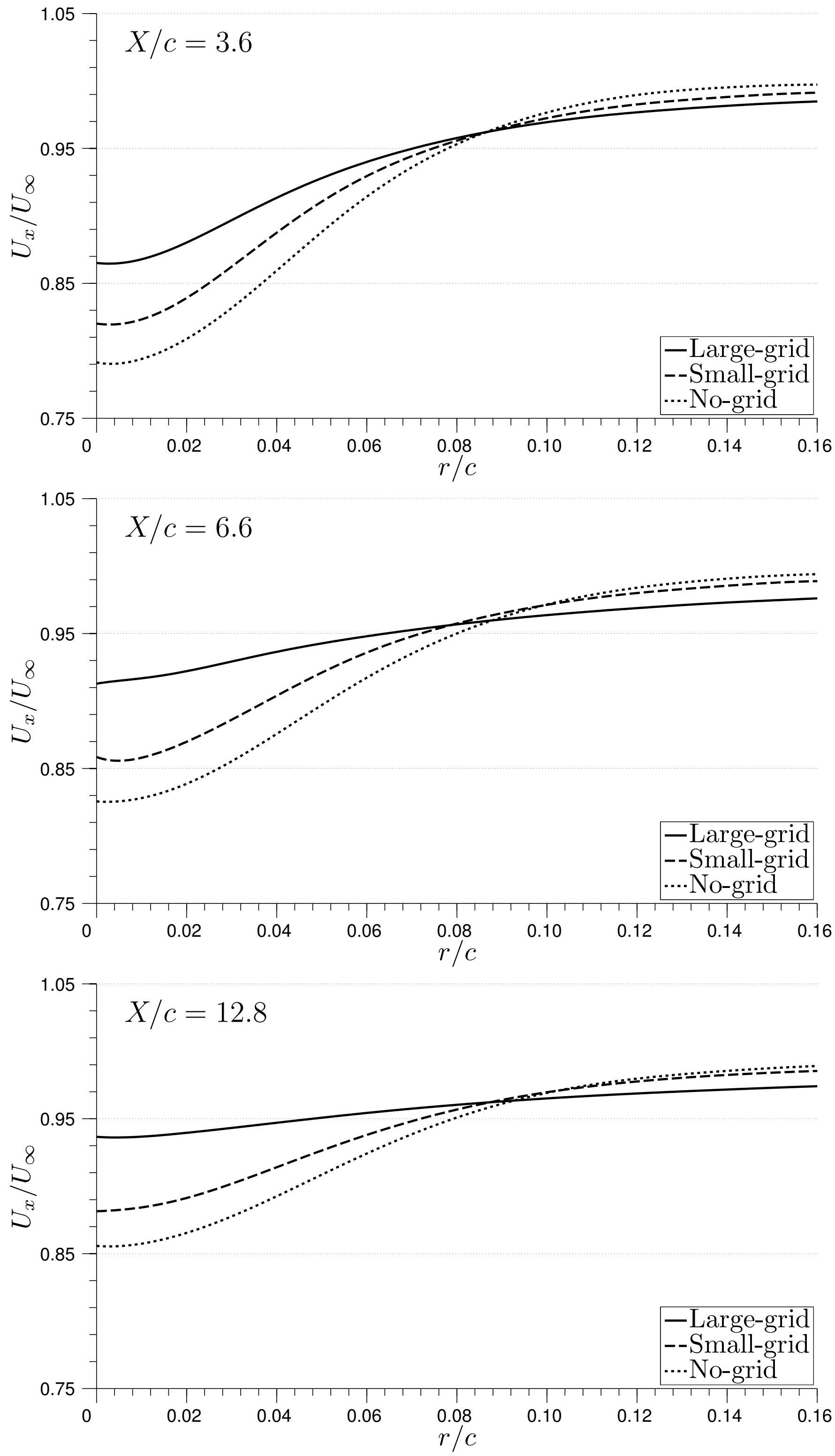

Figure 5.22: Radial profiles of axial velocity at $X/c = 3.6$, 6.6, and 12.8.

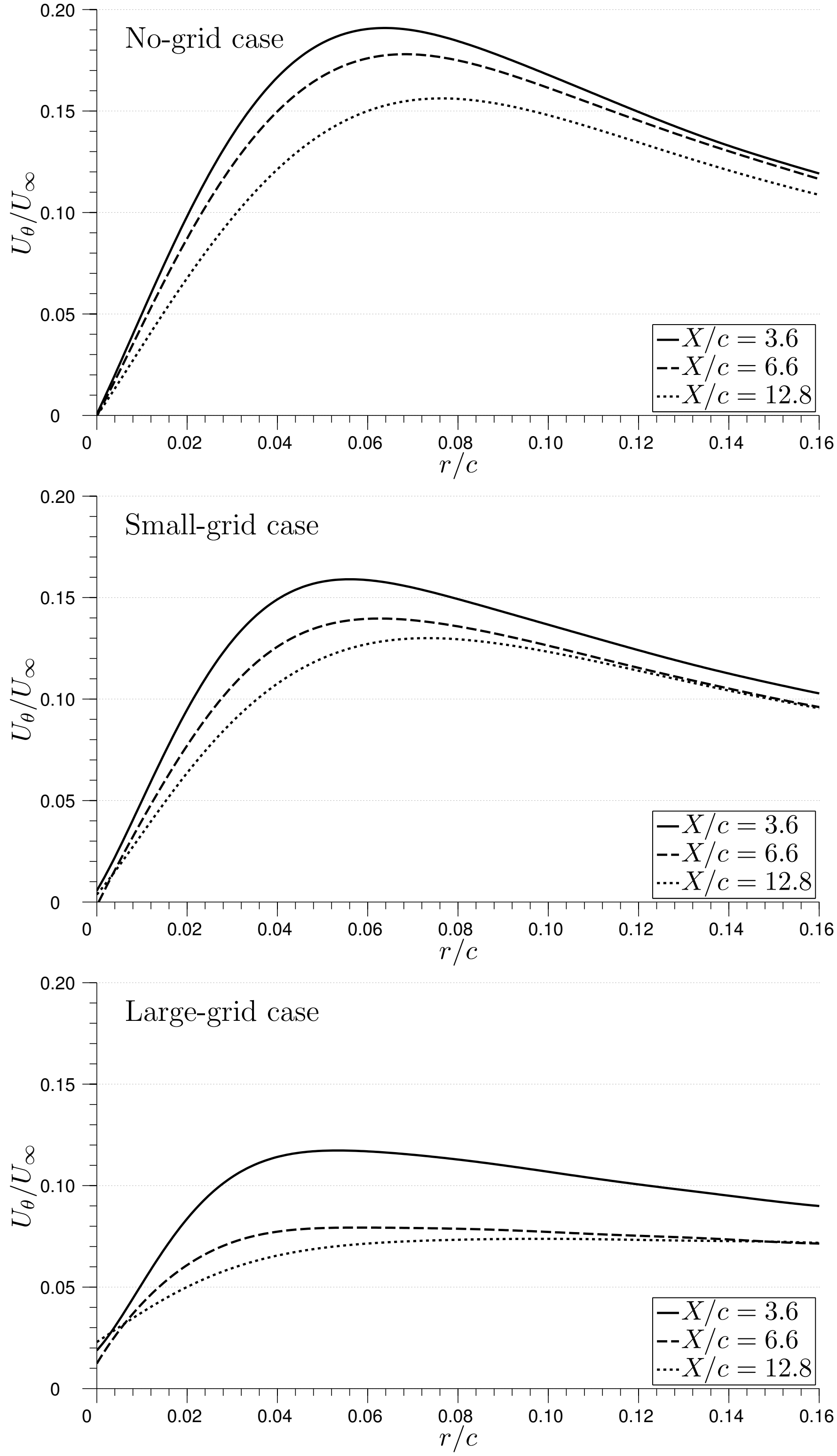

Figure 5.23: Radial profiles of azimuthal velocity for the no-grid, small-grid, and large-grid cases.

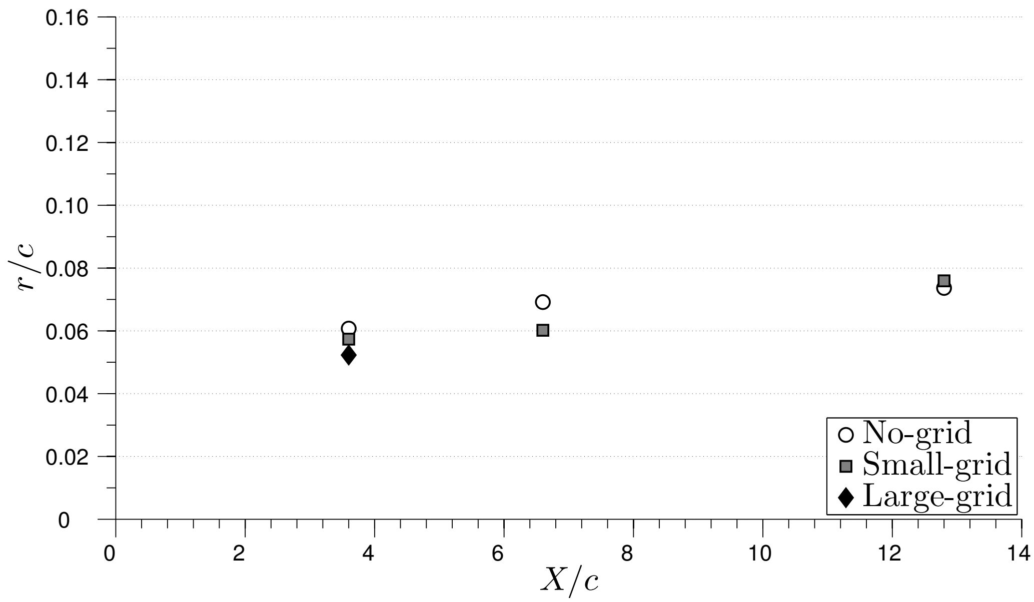

Figure 5.24: Radial locations of the peak values of U_θ.

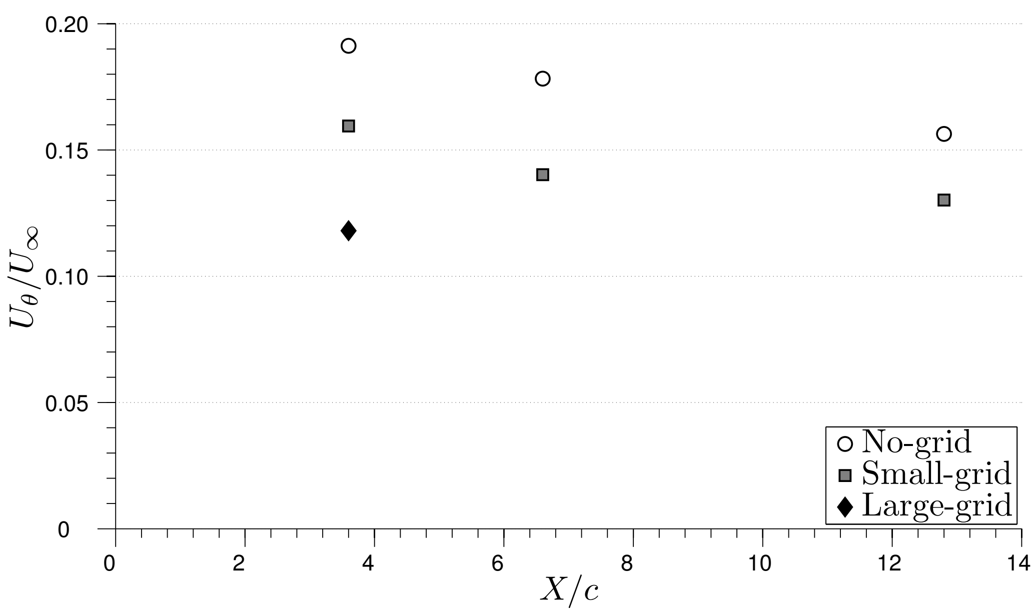

Figure 5.25: Peak values of U_θ.

turbulence conditions together at $X/c = 3.3$, 6.6, and 12.8, respectively. At all measurement planes, the peak U_θ/U_∞ was higher in the small-grid case than in the no-grid case (see also Figure 5.25). The location of the peak U_θ/U_∞ was further from the vortex axis in the no-grid case than the small-grid case at $X/c = 3.6$ and 6.6 but became slightly closer to the vortex axis than in the small-grid case at $X/c = 12.8$ (see also Figure 5.24). At $X/c = 3.6$, where distinct peaks in U_θ/U_∞ were discernible in all cases, the peak was lower and closer to the vortex axis in the large-grid case than in either the no- or small-grid cases. Near the vortex axis, the slopes of the U_θ/U_∞ profiles were very similar in the no- and small-grid cases. At $X/c = 3.6$ the azimuthal velocity profile from the small-grid case began to significantly diverge from the profile from the no-grid case at approximately $r/c = 0.02$, whereas at $X/c = 6.6$ and 12.8 the azimuthal velocity profiles began to diverge closer to the vortex axis, at approximately $r/c = 0.01$. The slope of the U_θ/U_∞ profile beyond the peak radius was consistently much higher in magnitude for the no- and small-grid cases than in the large-grid case.

5.7 Circulation variation

The circulation over a circular path centred on the vortex axis and with a radius r was calculated as

$$\Gamma(r) = U_\theta(r) 2\pi r. \tag{5.6}$$

Figure 5.27 shows the circulation at the radius of the peak in the U_θ profile for cases for which a distinct peak existed. The average circulation $\Gamma^* \approx 1.8 \times 10^{-3}$ m^2/s at the location of the peak value of U_θ for the no-grid case at the three measurement planes was used as a scale to normalize measurements of circulation in subsequent figures.

Comparisons of the radial variations of circulation under the different freestream turbulence conditions are shown in Figure 5.28. Γ increased monotonically with increasing radius for all freestream turbulence conditions and at all measurement planes. The radial extent of the measurements from the vortex axis was not sufficient to assess whether the vortex velocity field reached an irrotational state, in which case it would have been possible to estimate the total circulation Γ_o of the vortex. Moreover,

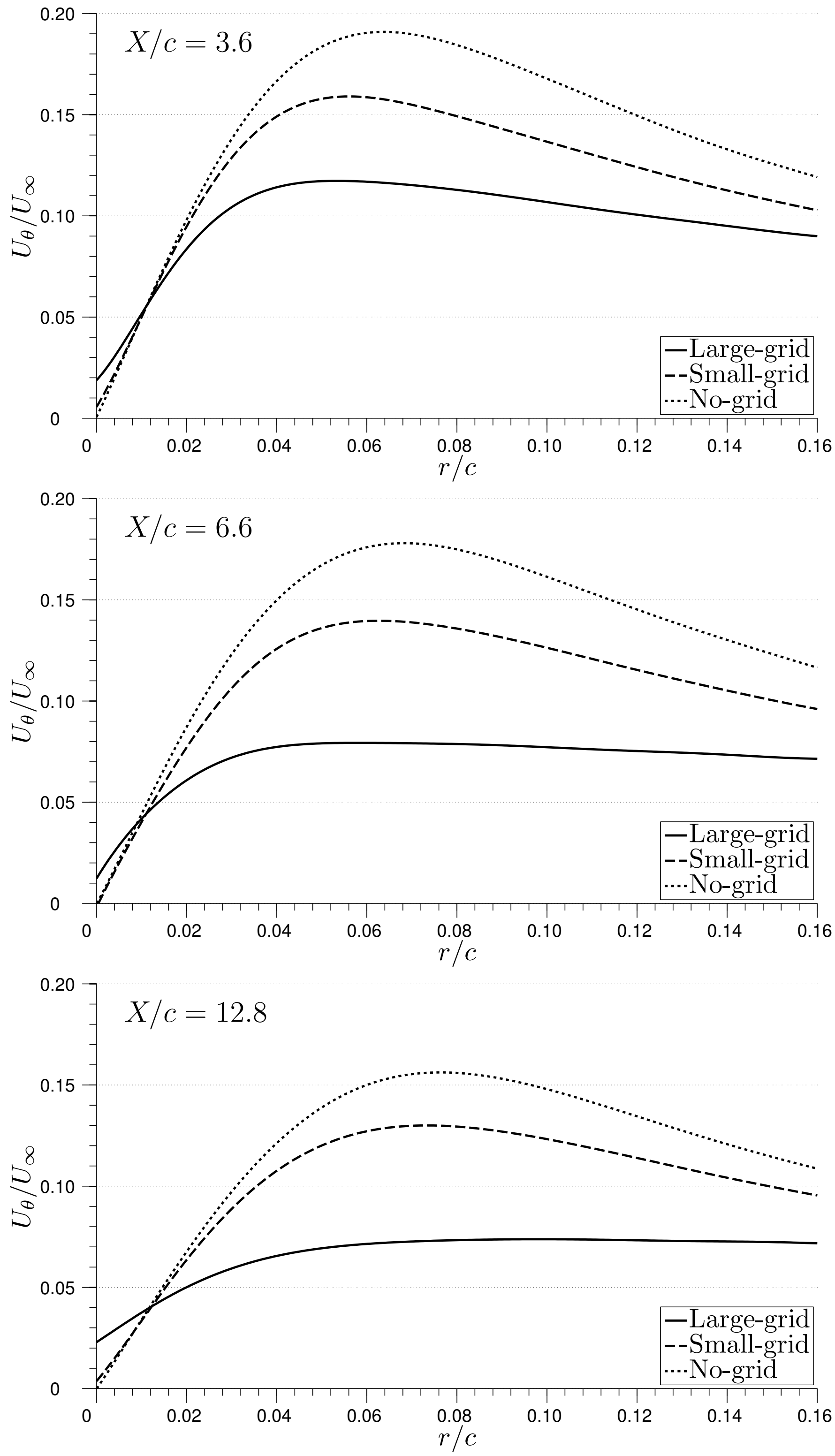

Figure 5.26: Radial profiles of azimuthal velocity at $X/c = 3.6$, 6.6, and 12.8.

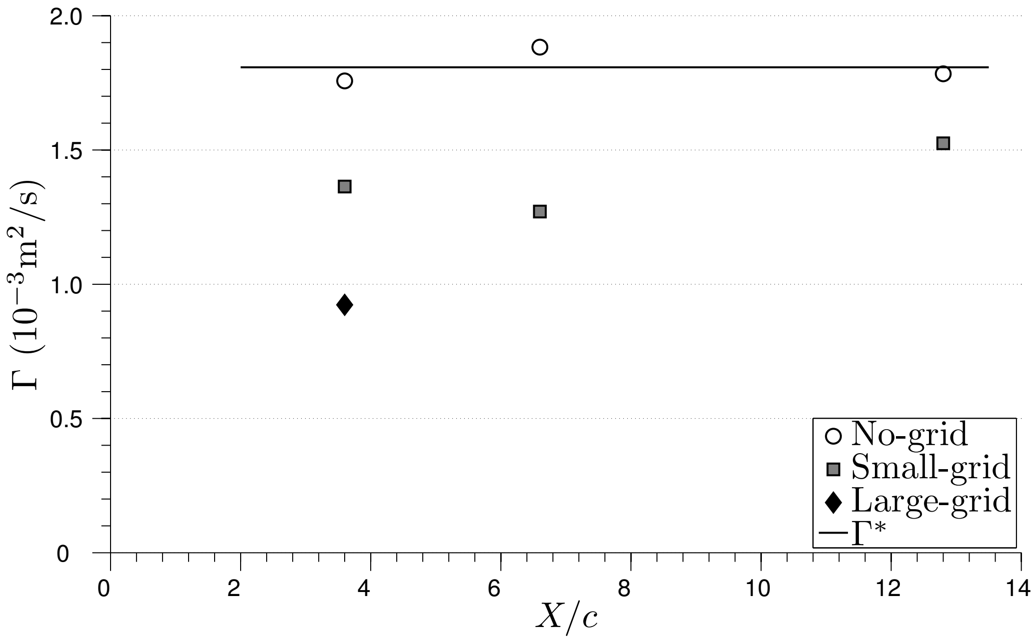

Figure 5.27: Circulation at location of the peak value of U_θ.

the available results show no evidence that the circulation overshoots Γ_o, as reported in some numerical studies (*e.g.*, Pantano & Jacquin, 2001; Pradeep & Hussain, 2010), although this possibility cannot be excluded. The circulation at each radial position for the no-grid case was significantly higher than that for the small-grid case, which in turn was significantly higher than that for the large-grid case. This shows clearly that core vorticity was diffused effectively by freestream turbulence. At very small radii ($r \leq 0.01c$), the circulations for all freestream conditions and downstream distances nearly collapsed onto a roughly parabolic function of the radius. This indicates that in all cases the vortex had an inner core that was in approximately rigid body rotation. Beyond the inner core, for the no-grid and small-grid cases at all measurement planes and for the large-grid case only close to the wing ($X/c = 3.6$), the circulation rates of growth kept increasing with radius, until reaching inflection points at the radii of the peak azimuthal velocity, beyond which the rates of growth decreased. This trend is compatible with the tendency towards irrotationality away from the vortex axis. In contrast, the shape of the Γ profiles for the large-grid cases at $X/c = 6.6$ and 12.8 were nearly linear even at the largest radii measured as a result of the nearly flat azimuthal velocity profiles (see Figure 5.23 c). In these cases, the possibility that the vortex would reach an irrotational state appears to be remote.

Figure 5.29 shows comparatively the radial variations of circulation on the three streamwise measurement planes for each of the three freestream conditions. For the no-grid case, the circulation within the measurement area decreased slowly downstream of the wing for all radial locations. This may be the result of diffusion of vorticity towards larger distances from the axis as well as of viscous decay of the vortex. Recalling that the total circulation within the vortex core, corresponding to the value of Γ at the radius of the peak azimuthal velocity, did not show significant variation at different streamwise locations (see Figure 5.27), one may conclude that viscous decay did not affect significantly the vortex core. For both cases with grids, the circulation at a fixed radius dropped measurably from $X/c = 3.6$ to $X/c = 6.6$, but did not change by any significant amount further downstream. In view of this complexity and also considering that the circulation profiles were qualitatively dissimilar for these two cases, it is difficult to make a general statement concerning the downstream evolution of the circulation of a vortex in grid turbulence.

5.8 On the vortex non-axisymmetry

Contour plots of the ensemble averaged local axial velocities $\langle U_x \rangle$ from the adjusted vector maps are shown in Figures 5.30, 5.31, and 5.32. At $X/c = 3.6$, a significant non-axisymmetry about the vortex axis is observed in $\langle U_x \rangle$, which is attributed to the wake of the wing that creates a velocity deficit on one side of the vortex only (Figure 5.30 a, c, and e). This deficit region is likely due to a velocity deficit in the wake of the wing which had not yet been completely dissipated at this distance from the wing and is still affecting the vortex. $\langle U_x \rangle$ are shown to be roughly axisymmetric in all other cases

The axisymmetry of the ensemble averaged local velocities $\langle U_\theta \rangle$ from the adjusted vector maps is examined in the contour plots shown Figures 5.30, 5.31, and 5.32. A slight non-axisymmetry about the vortex axis is observed in $\langle U_\theta \rangle$ at $X/c = 3.6$ with higher velocities coming in the top left and bottom right of the vortex in Figure 5.30 b, d, and f. $\langle U_\theta \rangle$ is shown to be roughly axisymmetric in all other cases excepting in the large-grid cases for the measurement planes at $X/c = 6.6$ and 12.8 (Figures 5.31

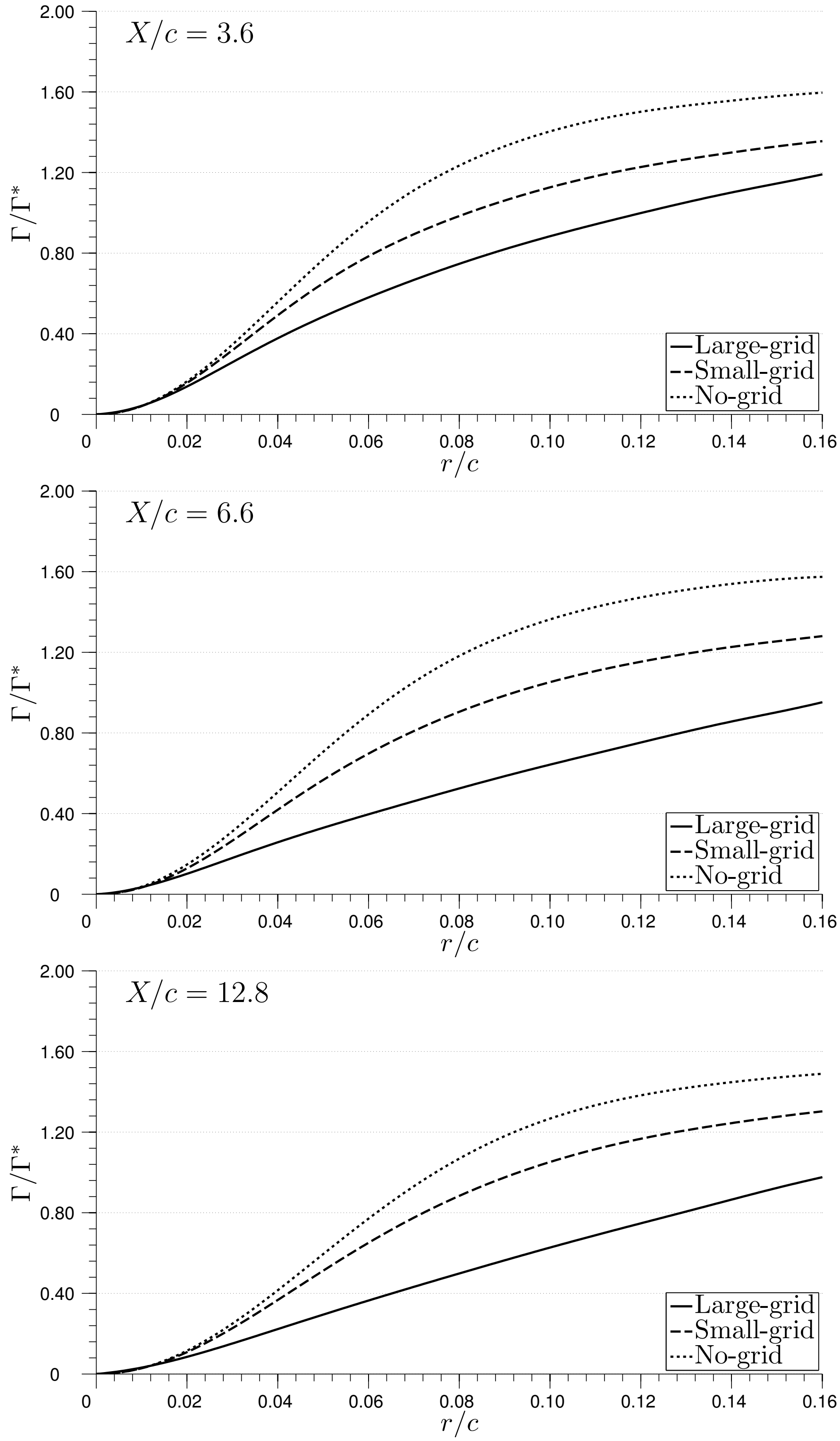

Figure 5.28: Radial variation of circulation at $X/c = 3.6$, 6.6, and 12.8.

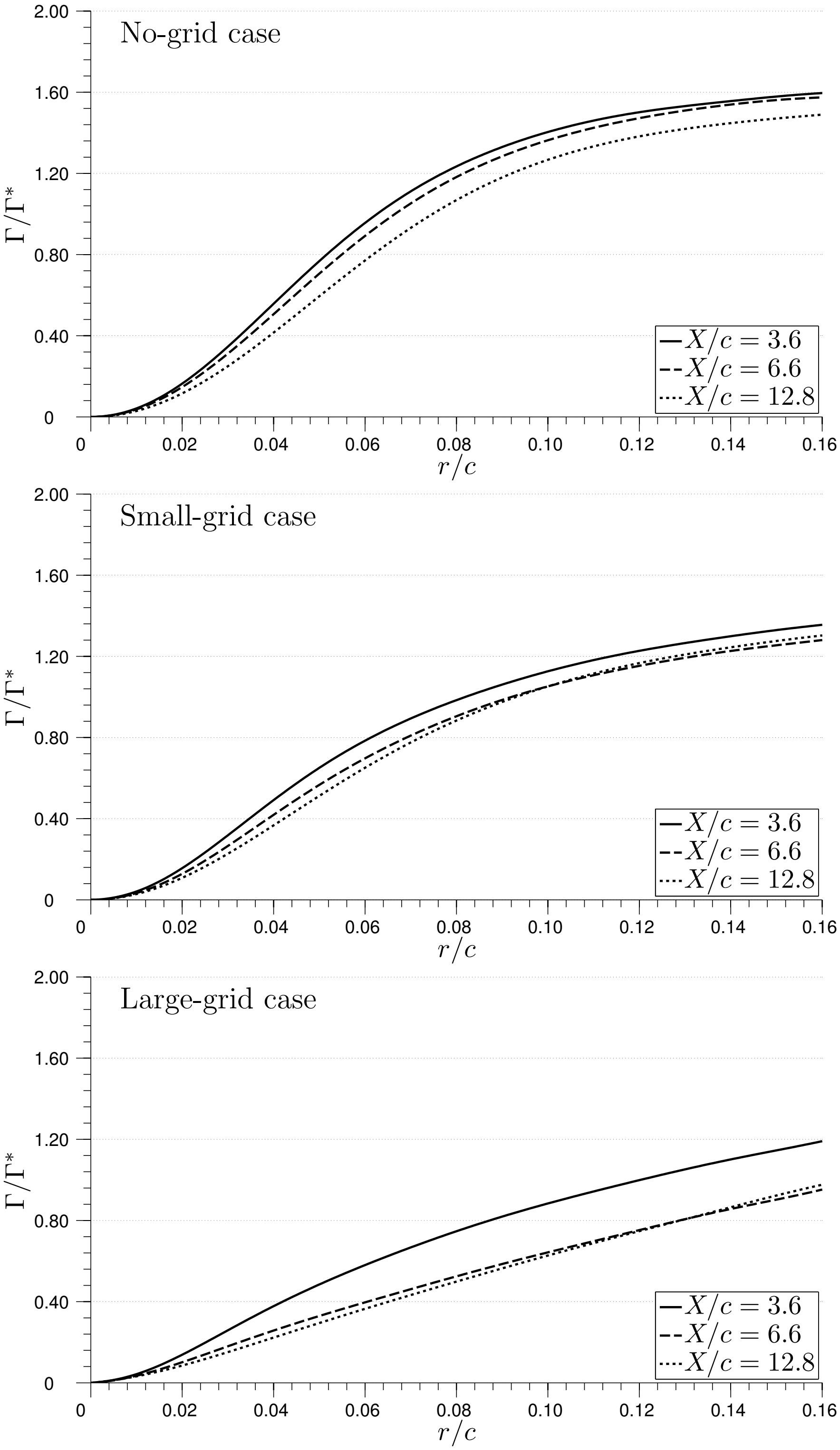

Figure 5.29: Radial variation of circulation for the no-grid, small-grid, and large-grid cases.

f and 5.32 f). In these cases, an intrusion of relatively low $\langle U_\theta \rangle$ values into the right side of the vortex is observed. The cause of this asymmetry is not definitively known. The large standard deviation of the vortex axis location in the large-grid cases (see Figure 5.7) meant that in some vector maps, the vortex axis was near the right side of the measurement window ($Z/c = 0.15$). Consequently, no velocity vectors were obtained at large radii on right side vortex in those cases. The average velocity vectors on the right side of the vortex at large radii were, therefore, based on fewer velocity measurements than those in the rest of the average field and, therefore, there was less confidence in the average vectors near $Z/c = 0.15$.

5.9 Comparisons with results from the literature

The present observation that the wandering amplitude of the vortex axis increased with streamwise distance from the wing (Figure 5.15) is in agreement with available literature (Devenport et al., 1996). Wandering amplitude in the current study was also shown to increase with increasing turbulence intensity, as observed by Bailey and Tavoularis (2008).

The vortex core was found to be wake-like in all cases examined. The maximum axial velocity deficit at the vortex axis was between 21 % and 6 % of the freestream velocity, depending on downstream distance and freestream conditions. The present no-grid results can be compared to those by Lee and Pereira (2010) in a low turbulence wind tunnel at $Re_c = 3 \times 10^5$, which is merely 25 % higher than the present one. Both studies examined the vortex generated by a square tipped NACA 0012 wing at $\alpha = 5°$. Lee and Pereira (2010) found that, after exhibiting a weak jet-like character near the trailing edge of the wing-tip, their vortex became wake-like with a core velocity deficit that increased with distance downstream of the wing to the end of their measurement range at $X/c = 5.0$. At $X/c = 5.0$ the axial velocity deficit was roughly 12 %, which is lower in magnitude but qualitatively compatible with the interpolated deficit of roughly 20 % for the no-grid case in the current study. In Figure 5.20, it can be seen that the magnitude of the core velocity deficit decreased with distance downstream of the wing in the measurement planes used in the current study. This appears to be in contrast with the trend observed by Lee and Pereira (2010), however, one should

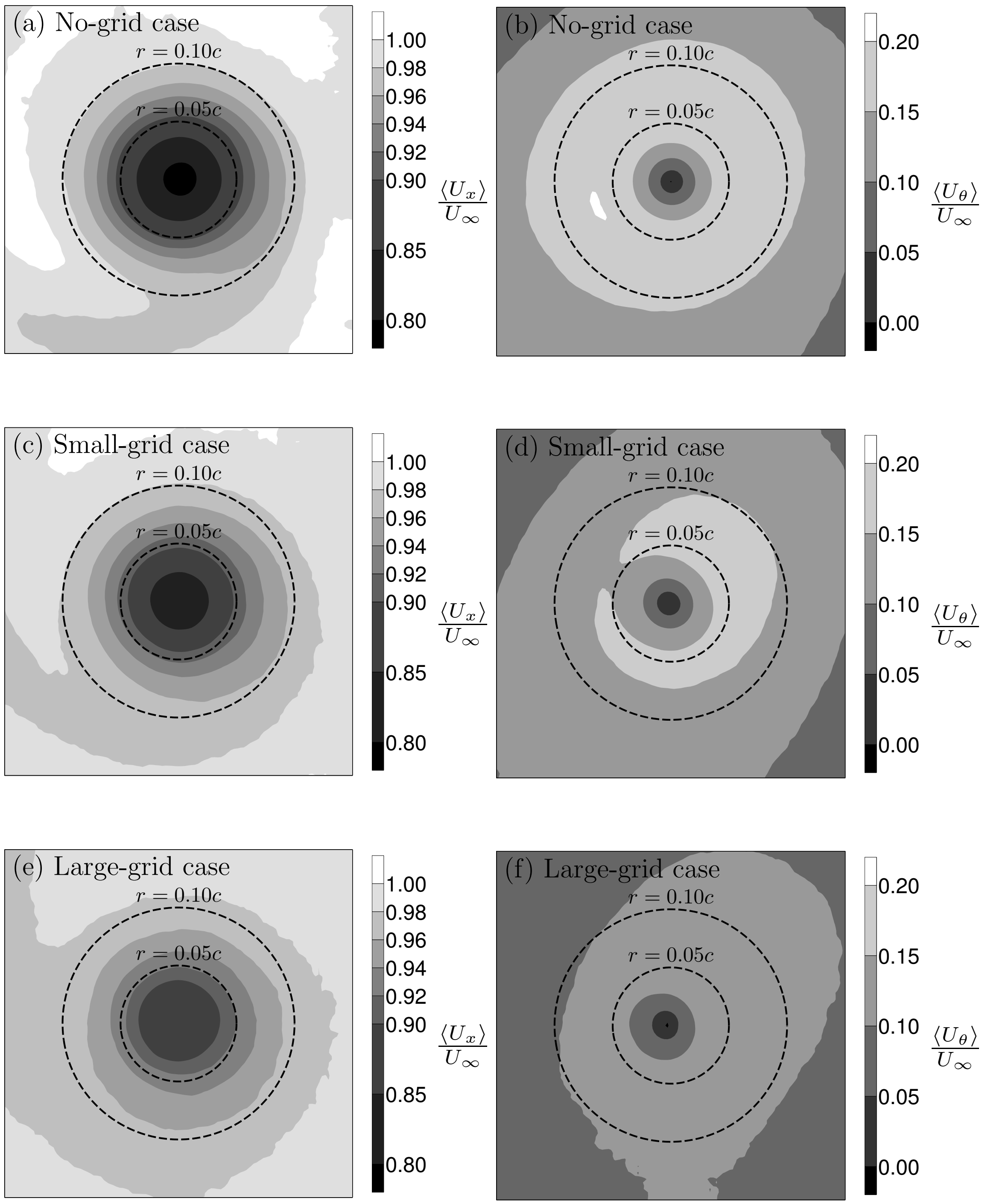

Figure 5.30: Ensemble averages of U_x and U_θ at $X/c = 3.6$.

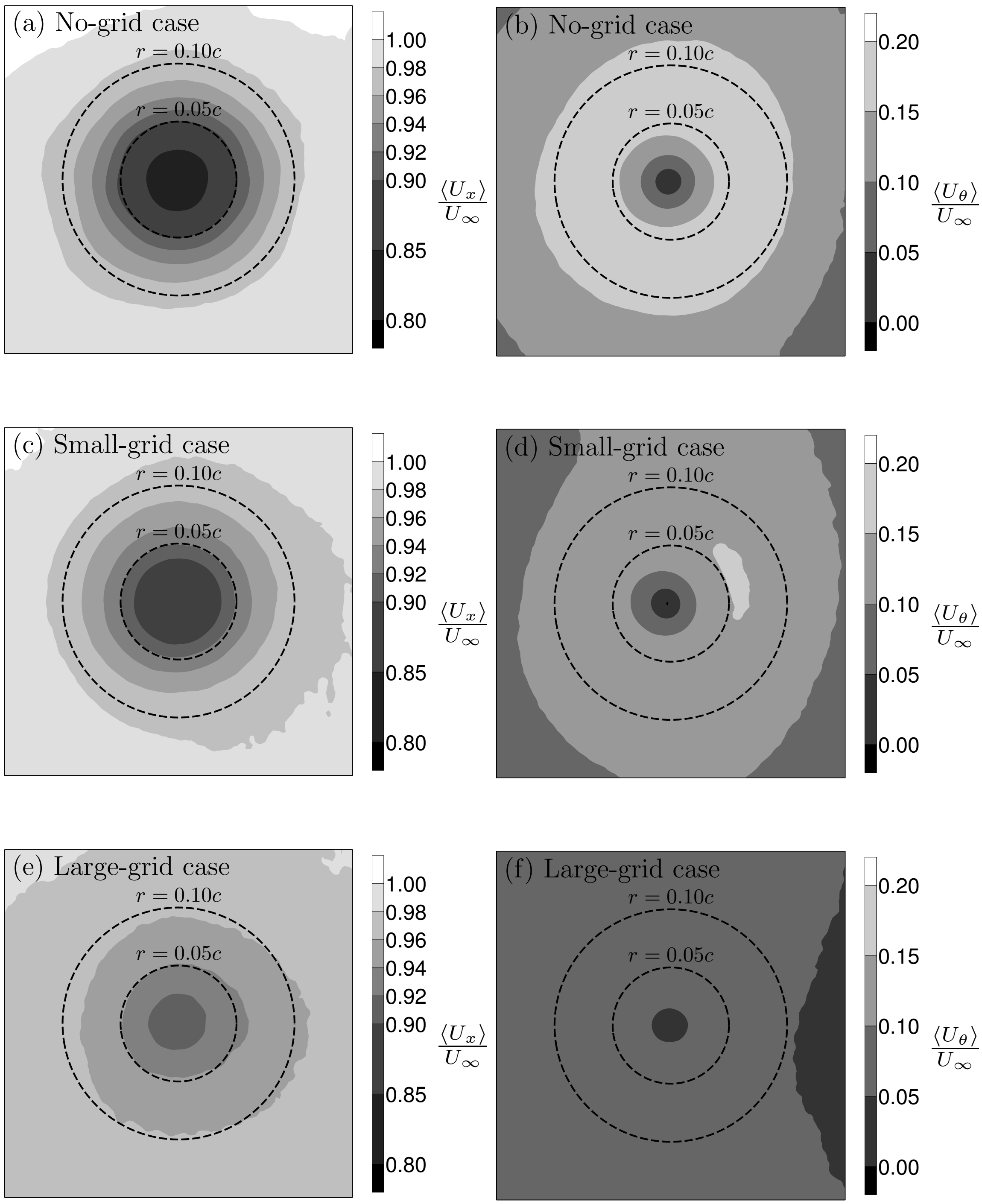

Figure 5.31: Ensemble averages of U_x and U_θ at $X/c = 6.6$.

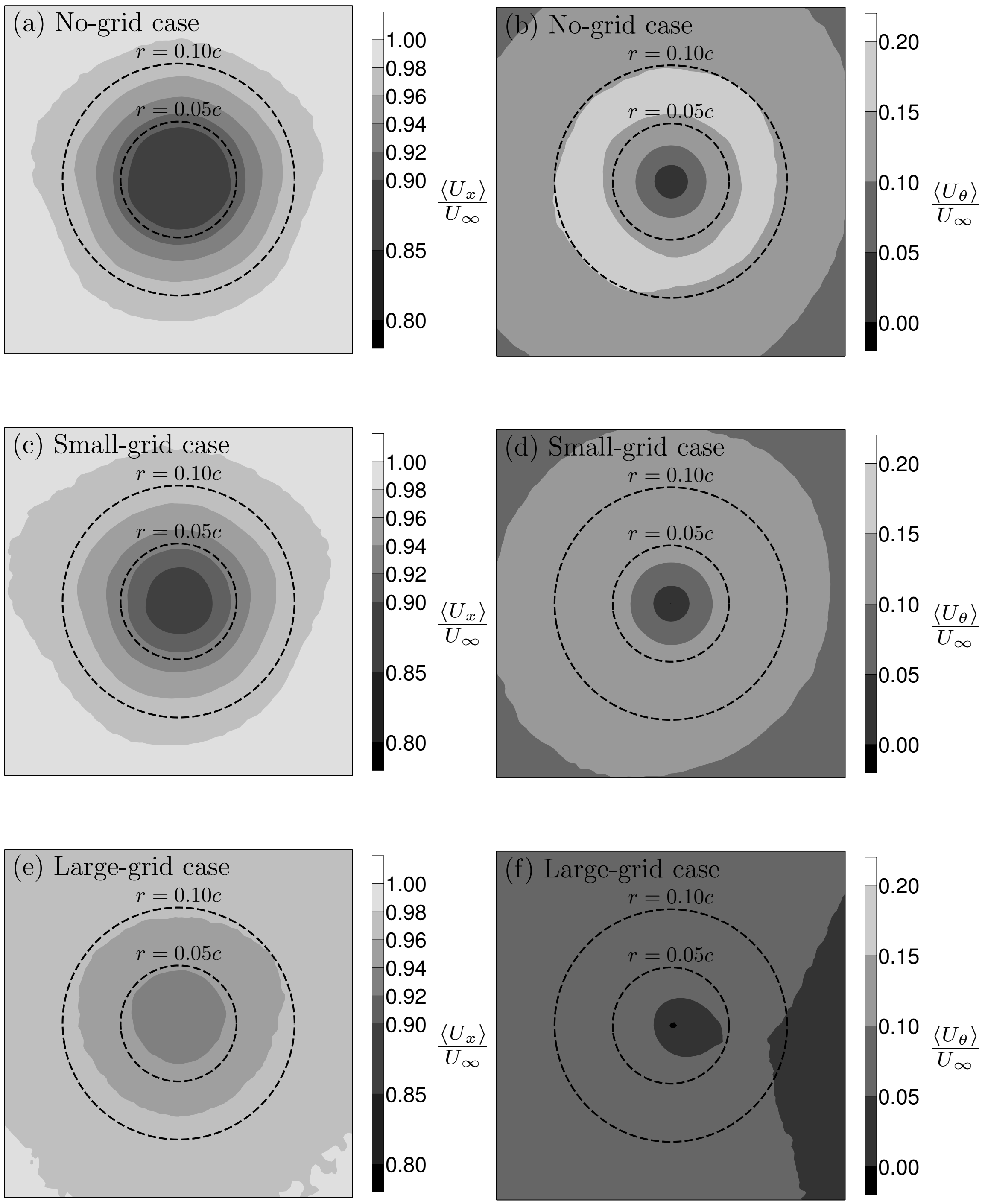

Figure 5.32: Ensemble averages of U_x and U_θ at $X/c = 12.8$.

note that in their study the growth of the core velocity deficit was essentially arrested at $X/c = 5.0$, which is upstream of all but one of the measurement planes in the current study. It is plausible that changes in the trends of the core velocity deficit may occur at different downstream locations in the two studies or that these trends may be sensitive to experimental conditions affecting the vortex formation process, such as the wing aspect ratio, the Reynolds number, and the wing surface roughness.

The shapes of the radial profiles of azimuthal velocity conformed to conventional vortex profiles in both the no- and small-grid cases: each profile had an approximately linear section near the vortex axis and reached a peak beyond which the azimuthal velocity decreased in a manner which was compatible with a trend towards irrotationality. In the large-grid case, the profile shape beyond the radius of the peak azimuthal velocity was atypical, as its decrease appeared to be roughly linear and at a small rate, especially at $X/c = 6.6$ and 12.8. It is interesting to note that this large-grid profile shape was similar to radial profiles of azimuthal velocity reported by Bailey and Tavoularis (2008) for a case with high freestream turbulence intensity before it was corrected for the wandering of the vortex axis. This would suggest that the identification of the vortex axis in the large-grid case was possibly not precise enough for one to determine an accurate velocity profile in the frame of reference attached to the vortex axis (see Section 5.6).

In agreement with the results of Bailey and Tavoularis (2008), the magnitude of the peak azimuthal velocity was found to decrease with increasing turbulence intensity and with increasing distance downstream of the wing (Figure 5.25). However, the radial location of this peak azimuthal velocity was found to increase consistently with distance downstream of the wing, which contradicts the conclusion of Bailey and Tavoularis (2008) that this radius does not depend on streamwise position (Figure 5.24).

Chapter 6

Conclusions and recommendations for future work

6.1 Conclusions

In this study, the effects of freestream turbulence on the wandering motion and the velocity field of an isolated wing-tip vortex were investigated using several experimental techniques and vortex identification methods.

Data were collected in a water tunnel facility under three different freestream conditions, including unobstructed flow and two cases with grid-generated turbulence. Velocity measurements were collected on three cross-planes downstream of the wing.

The location of the vortex axis in planar velocity maps was identified using the swirling strength, the Q parameter, the axial velocity deficit, a planar least squares fit technique based on the azimuthal velocity profile, and the centre of streamlines. The results of the different approaches were compared and the centre of mass of the swirling strength found to be most suitable for the conditions of this study.

The amplitude of vortex wandering was found to increase as the turbulence intensity and length scales were increased. The amplitude of vortex wandering also increased with increasing distance downstream of the wing under all freestream conditions, in agreement with past literature.

In all cases examined, the wing-tip vortex core was wake-like, exhibiting an axial velocity deficit with respect to the freestream. The magnitude of the velocity deficit decreased as the intensity and length scales of the freestream turbulence increased. The magnitude of the velocity deficit also decreased as the distance of the measurement plane downstream of the wing was increased.

The maximum azimuthal velocity generally decreased and its location moved further from the vortex axis as the intensity and length scales of freestream turbulence increased. As the distance of the measurement plane from the wing was increased, however, the maximum azimuthal velocity decreased and its location moved closer to the vortex axis. Circulation about the vortex at the radial location of the peak azimuthal velocity decreased with increasing turbulence intensity.

The waveform shape of the vortex axis was reconstructed from two LIF images recorded simultaneously on two axial planes that were perpendicular to each other and was subsequently analysed to provide the angle of inclination of the vortex axis and its wandering motion.

The potential of using high speed LIF images taken in the plane perpendicular to the streamwise axis to identify the vortex axis location with high frequency resolution was evaluated. This technique showed promise for the cases with low freestream turbulence intensity but became unusable for higher freestream turbulence intensities as the dye patterns were too distorted for the location of the vortex axis to be discerned from them.

6.2 Recommendations for future work

The accurate identification of the vortex axis location is of fundamental importance in analysing the velocity fields of wandering vortices. More study of the reliability of parameters used to locate the vortex axis is needed, especially for turbulent flows. The use of tomographic PIV data would be beneficial both in allowing the calculation of vortex axis indicator parameters in their three dimensional forms as well as in reducing the uncertainty introduced by the inclination of the vortex axis with respect to the streamwise direction.

Wing-tip vortex wandering remains poorly understood. To improve our understanding of this problem, additional high quality measurements acquired under a wide range of experimental conditions are needed, including additional measurements of wing-tip vortices in turbulent freestreams at higher Reynolds numbers than that of the present tests. The use of time-resolved PIV systems would be very beneficial, as this method would provide a more accurate description of vortex wandering motion, allowing one to identify any organized patterns of motion, if such exist.

References

Anderson, E. A., & Lawton, T. A. (2003). Correlation between vortex strength and axial velocity in a trailing vortex. *Journal of Aircraft*, *40*(4), 699–704.

Arcoumanis, C., McGuirk, J. J., & Palma, J. M. L. M. (1990). On the use of fluorescent dyes for concentration measurements in water flows. *Experiments in Fluids*, *10*(2-3), 177–180.

Bailey, S. (2006). *The interaction of a wing-tip vortex and free-stream turbulence.* PhD Dissertation, University of Ottawa, Ottawa, Canada.

Bailey, S., Estejab, B., Robert, M., & Tavoularis, S. (2011). Long-wavelength vortex motion induced by free-stream turbulence. In *Seventh International Symposium on Turbulence and Shear Flow Phenomena, Ottawa, Canada.*

Bailey, S., & Tavoularis, S. (2008). Measurements of the velocity field of a wing-tip vortex, wandering in grid turbulence. *Journal of Fluid Mechanics*, *601*, 281–315.

Bailey, S., Tavoularis, S., & Lee, B. H. (2006). Effects of free-stream turbulence on wing-tip vortex formation and near field. *Journal of Aircraft*, *43*(5), 1282–1291.

Baker, G. R., Barker, S. J., Bofah, K. K., & Saffman, P. G. (1974). Laser anemometer measurements of trailing vortices in water. *Journal of Fluid Mechanics*, *65*, 325–336.

Bandyopadhyay, P. R., Ash, R. L., & Stead, D. J. (1991). Organized nature of a turbulent trailing vortex. *AIAA Journal*, *29*(10), 1627–1633.

Batchelor, G. K. (1964). Axial flow in trailing line vortices. *Journal of Fluid Mechanics*, *20*, 645–658.

Batchelor, G. K., & Townsend, A. A. (1948). Decay of isotropic turbulence in the initial period. *Proceedings of the Royal Society of London. Series A, Mathematical and Physical Sciences*, *193*(1035), 539-558.

Beninati, M. L., & Marshall, J. S. (2005). An experimental study of the effect of free-stream turbulence on a trailing vortex. *Experiments in Fluids*, *38*(2), 244-257.

Bhagwat, M. J., & Ramasamy, M. (2012). Effect of tip vortex aperiodicity on measurement uncertainty. *Experiments in Fluids*, *53*(5), 1191–1202.

Birch, D., Lee, T., Mokhtarian, F., & Kafyeke, F. (2003). Rollup and near-field behavior of a tip vortex. *Journal of Aircraft*, *40*(3), 603–607.

Breitsamter, C. (2011). Wake vortex characteristics of transport aircraft. *Progress in Aerospace Sciences*, *47*(2), 89 - 134.

Carmer, C., Konrath, R., Schröder, A., & Monnier, J.-C. (2008). Identification of vortex pairs in aircraft wakes from sectional velocity data. *Experiments in Fluids*, *44*(3), 367-380.

Comte-Bellot, G., & Corrsin, S. (1966). The use of a contraction to improve the isotropy of grid-generated turbulence. *Journal of Fluid Mechanics*, *25*(4), 657–682.

Crow, S. C. (1970). Stability theory for a pair of trailing vortices. *AIAA Journal*, *8*, 2172-2179.

del Pino, C., Parras, L., Felli, M., & Fernandez-Feria, R. (2011). Structure of trailing vortices: Comparison between particle image velocimetry measurements and theoretical models. *Physics of Fluids*, *23*(1).

Devenport, W. J., Rife, M. C., Liapis, S. I., & Follin, G. J. (1996). The structure and development of a wing-tip vortex. *Journal of Fluid Mechanics*, *312*, 67–106.

Devenport, W. J., Vogel, C. M., & Zsoldox, J. S. (1999). Flow structure produced by the interaction and merger of a pair of co-rotating wing-tip vortices. *Journal of Fluid Mechanics*, *394*, 357–377.

Dunn, W. (2004). *Vortex shedding from cylinders with step-changes in diameter in uniform and shear flows.* PhD Dissertation, University of Ottawa, Ottawa, Canada.

Green, S. I. (1995). Wing tip vortices. In S. I. Green (Ed.), *Fluid Vortices* (Vol. 30, p. 427-469). Springer Netherlands.

Green, S. I., & Acosta, A. J. (1991). Unsteady flow in trailing vortices. *Journal of Fluid Mechanics*, *227*, 107–134.

Gursul, I., & Xie, W. (2000). Origin of vortex wandering over delta wings. *Journal of Aircraft*, *37*(2), 348–350.

Hama, F. R. (1962). Progressive deformation of a curved vortex filament by its own induction. *Physics of Fluids*, *5*(10), 1156-1162.

Helmholtz, H. (1867). On integrals of the hydrodynamical equations, which express vortex-motion (P. Tait, Trans.). *Philosophical Magazine Series 4*, *33*(226), 485–512. (Original work published 1858)

Heyes, A., Jones, R., & Smith, D. (2004). Wandering of wing-tip vortices. In *12th International Symposium on Application of Laser Techniques to Fluid Mechanics, Lisbon, Portugal.*

Holzäpfel, F., Hofbauer, T., Darracq, D., Moet, H., Garnier, F., & Gago, C. F. (2003). Analysis of wake vortex decay mechanisms in the atmosphere. *Aerospace Science and Technology*, *7*(4), 263 - 275.

Hunt, J. C., Wray, A., & Moin, P. (1988). Eddies, streams, and convergence zones in turbulent flows. In *Studying Turbulence Using Numerical Simulation Databases, 2* (Vol. 1, pp. 193–208).

Hussain, A. K. M. F., & Hayakawa, M. (1987). Eduction of large-scale organized structures in a turbulent plane wake. *Journal of Fluid Mechanics*, *180*, 193–229.

International Air Transport Association. (2013). *Fact sheet: Fuel.* Retrieved 2013-12-04, from `http://www.iata.org/pressroom/facts_figures/fact_sheets/Documents/fuel-fact-sheet.pdf`

Iungo, G. V., Skinner, P., & Buresti, G. (2009). Correction of wandering smoothing effects on static measurements of a wing-tip vortex. *Experiments in Fluids*, *46*(3), 435-452.

Jacquin, L. (2005). On trailing vortices: A short review. *International Journal of Heat and Fluid Flow*, *26*(6), 843 - 854.

Jacquin, L., Fabre, D., Geffroy, P., & Coustols, E. (2001). The properties of a transport aircraft wake in the extended near field - an experimental study. In *39th Aerospace Sciences Meeting and Exhibit.* American Institute of Aeronautics and Astronautics.

Jacquin, L., & Pantano, C. (2002). On the persistence of trailing vortices. *Journal of Fluid Mechanics*, *471*, 159–168.

Jeong, J., & Hussain, F. (1995). On the identification of a vortex. *Journal of Fluid Mechanics*, *285*, 69–94.

Jiang, M., Machiraju, R., & Thompson, D. (2005). 14 - detection and visualization of vortices. In C. D. Hansen & C. R. Johnson (Eds.), *Visualization Handbook* (p. 295 - 309). Burlington: Butterworth-Heinemann.

Kroo, I. (2001). Drag due to lift: Concepts for prediction and reduction. *Annual Review of Fluid Mechanics*, *33*(1), 587-617.

LaVision Inc. (2012). *FlowMaster* [Product Manual].

Lee, T., & Pereira, J. (2010). Nature of wakelike and jetlike axial tip vortex flows. *Journal of Aircraft*, *47*(6), 1946–1954.

Marshall, J. S. (1997). The flow induced by periodic vortex rings wrapped around a columnar vortex core. *Journal of Fluid Mechanics*, *345*, 1–30.

Marshall, J. S., & Beninati, M. L. (2005). External turbulence interaction with a columnar vortex. *Journal of Fluid Mechanics*, *540*, 221–245.

Melander, M. V., & Hussain, F. (1993). Coupling between a coherent structure and fine-scale turbulence. *Physical Review E*, *48*, 2669–2689.

Moore, D. W., & Saffman, P. G. (1973). Axial flow in laminar trailing vortices. *Proceedings of the Royal Society of London. A. Mathematical and Physical Sciences*, *333*(1595), 491-508.

O'Neill, P., Nicolaides, D., Honnery, D., & Soria, J. (2004). Autocorrelation functions and the determination of integral length with reference to experimental and numerical data. In *Proceedings of the Fifteenth Australasian Fluid Mechanics Conference. University of Sydney.*

Pantano, C., & Jacquin, L. (2001). Differential rotation effects within a turbulent batchelor vortex. In B. J. Geurts, R. Friedrich, & O. Mtais (Eds.), *Direct and large-eddy simulation iv* (Vol. 8, p. 321-328). Springer Netherlands.

Pope, S. (2000). *Turbulent flows.* Cambridge University Press.

Pradeep, D., & Hussain, F. (2010). Vortex dynamics of turbulencecoherent structure interaction. *Theoretical and Computational Fluid Dynamics*, *24*(1-4), 265-282.

Raffel, M. (2007). *Particle image velocimetry a practical guide.* Berlin: Heidelberg.

Ragab, S., & Sreedhar, M. (1995). Numerical simulation of vortices with axial velocity deficits. *Physics of Fluids (1994-present)*, *7*(3), 549-558.

Rayleigh, L. (1917). On the dynamics of revolving fluids. *Proceedings of the Royal Society of London. Series A, Containing Papers of a Mathematical and Physical*

Character, *93*(648), 148-154.

Robinson, S. K. (1990). A review of vortex structures and associated coherent motions in turbulent boundary layers. In A. Gyr (Ed.), *Structure of Turbulence and Drag Reduction* (p. 23-50). Springer Berlin Heidelberg.

Rokhsaz, K., Foster, S. R., & Miller, L. S. (2000). Exploratory study of aircraft wake vortex filaments in a water tunnel. *Journal of Aircraft*, *37*(6), 1022–1027.

Sarpkaya, T., & Daly, J. J. (1987). Effect of ambient turbulence on trailing vortices. *Journal of Aircraft*, *24*(6), 399–404.

Schram, C., Rambaud, P., & Riethmuller, M. (2004). Wavelet based eddy structure eduction from a backward facing step flow investigated using particle image velocimetry. *Experiments in Fluids*, *36*(2), 233-245.

Spalart, P. R. (1998). Airplane trailing vortices. *Annual Review of Fluid Mechanics*, *30*(1), 107-138.

Specialist Committee on Uncertainty Analysis of 25th ITTC. (2008). *Recommended Procedures and Guidelines: Uncertainty Analysis - Particle Image Velocimetry.* International Towing Tank Conference.

Stephan, A., Holzäpfel, F., & Misaka, T. (2013). Aircraft wake-vortex decay in ground proximity - physical mechanisms and artificial enhancement. *Journal of Aircraft*, *50*(4), 1250–1260.

Sun, M., & Marshall, J. S. (2000). A flow visualization study of vortex interaction with the wake of a sphere. *Journal of Fluids Engineering*, *122*(3), 560–568.

Takahashi, N., Ishii, H., & Miyazaki, T. (2005). The influence of turbulence on a columnar vortex. *Physics of Fluids*, *17*(3).

Tavoularis, S. (2005). *Measurement in fluid mechanics.* Cambridge; New York: Cambridge University Press.

van der Wall, B. G., & Richard, H. (2006). Analysis methodology for 3C-PIV data of rotary wing vortices. *Experiments in Fluids*, *40*(5), 798-812.

Vanderwel, C. (2011). *Measurements of passive scalar dispersion from a continuous point source in uniformly sheared turbulence* [PhD Proposal]. University of Ottawa.

van Jaarsveld, J. P. J., Holten, A. P. C., Elsenaar, A., Trieling, R. R., & van Heijst, G. J. F. (2011). An experimental study of the effect of external turbulence on the decay of a single vortex and a vortex pair. *Journal of Fluid Mechanics*, *670*, 214–239.

Widnall, S. E. (1975). The structure and dynamics of vortex filaments. *Annual Review of Fluid Mechanics*, *7*(1), 141-165.

Zhou, J., Adrian, R. J., Balachandar, S., & Kendall, T. M. (1999). Mechanisms for generating coherent packets of hairpin vortices in channel flow. *Journal of Fluid Mechanics*, *387*, 353–396.